# Generalized relativistic mean-field model with non-linear derivative nucleon-meson couplings for nuclear matter and finite nuclei

**Verallgemeinertes relativistisches Mittelfeldmodell mit nichtlinearen Nukleon-Meson Ableitungskopplungen für Kernmaterie und endliche Kerne**

Zur Erlangung des Grades eines Doktors der Naturwissenschaften (Dr. rer. nat.)
genehmigte Dissertation von M.sc. Sofija Antić aus Pula (Kroatien)
Tag der Einreichung: 13.06.2017, Tag der Prüfung: 12.07.2017

Darmstadt 2018 — D 17

1. Gutachten: Prof. Dr. Karlheinz Langanke
2. Gutachten: Prof. Dr. Gabriel Martinez-Pinedo

TECHNISCHE UNIVERSITÄT DARMSTADT

GSI Helmholtzzentrum für Schwerionenforschung, Theorie

Institut für Kernphysik

Faschbereich Physik

Generalized relativistic mean-field model with non-linear derivative nucleon-meson couplings for nuclear matter and finite nuclei
Verallgemeinertes relativistisches Mittelfeldmodell mit nichtlinearen Nukleon-Meson Ableitungskopplungen für Kernmaterie und endliche Kerne

Genehmigte Dissertation von M.sc. Sofija Antić aus Pula (Kroatien)

1. Gutachten: Prof. Dr. Karlheinz Langanke
2. Gutachten: Prof. Dr. Gabriel Martinez-Pinedo

Tag der Einreichung: 13.06.2017
Tag der Prüfung: 12.07.2017

Darmstadt 2018 — D 17



# Erklärung zur Dissertation

Hiermit versichere ich, die vorliegende Dissertation ohne Hilfe Dritter nur mit den angegebenen Quellen und Hilfsmitteln angefertigt zu haben. Alle Stellen, die aus Quellen entnommen wurden, sind als solche kenntlich gemacht. Diese Arbeit hat in gleicher oder ähnlicher Form noch keiner Prüfungsbehörde vorgelegen.

Darmstadt, den Juni 13, 2017

(Sofija Antić)

# Abstract

The equation of state (EOS) for highly compressed dense matter is one of the main concerns of nuclear astrophysics in recent years. It is essential for modeling compact astrophysical objects like neutron stars (NS), their mergers and core-collapse supernovae (CCSN). It also sets the conditions for the creation of chemical elements in the universe, in particular for the r-process whose astrophysical site is still under debate. Therefore, it is an active theoretical and experimental research topic.

At present, a realistic and quantitative description of dense matter is not available from first principles using the basic theory of quantum chromodynamics (QCD). Hence, a large variety of phenomenological models has been developed for describing nuclear systems. These models depend on a number of adjustable parameters that have to be determined by data. It is essential for the further development of the field to determine the most realistic parameter sets and to use them consistently. New and more precise constraints on EOS parameters are becoming available with the advancement of technology and novel astrophysical observations and laboratory experiments conducted. As a consequence we are able to provide models that can be further used in many studies, both for nuclear structure and astrophysical applications.

In this work an extended relativistic mean-field (RMF) model, the density-dependent (DD) non-linear derivative (NLD), or in short DD-NLD model, is developed. The novelty is combining density-dependent nucleon-meson couplings with the energy dependence introduced in the nucleon self-energies in order to reproduce the experimental behavior of the optical potential. The model is applied to the description of infinite nuclear matter, focusing on the high density region above nuclear saturation, and used to obtain the NS EOS at zero temperature. In order to determine the model parameters they are fitted to nuclear matter properties at saturation density as well as to selected properties of several finite nuclei among which are binding energies, charge and diffraction radii, surface thicknesses, etc. The obtained set of parameters is used in the calculation of the NS mass-radius relation by solving the Tolman-Oppenheimer-Volkoff equations. This was considered only for nuclear systems at vanishing temperature. For general astrophysical applications however, e.g. in order to provide EOS tables for simulations of CCSN, it is necessary to extend the theoretical description to finite temperatures. Since the developed DD-NLD model has a very general form, it can in principle be extended to temperature dependent cases. For the purpose of this work, the extended temperature dependent model for nuclear matter is developed, but in the limit of low temperatures, up to about 20 MeV. This allows to study the liquid-gas phase transition for nuclear matter expected at sub-saturation densities, covering the full range of isospin asymmetries. A study of the spinodal and binodal regions of instability and phase coexistence is performed. We discuss the influence of the energy-dependent self-energies in the EOS model with increasing temperature and the effects it has on the liquid-gas phase transition.

# Abstrakt

Die Zustandsgleichung für hochkomprimierte dichte Materie ist eines der Hauptanliegen der nuklearen Astrophysik in den letzten Jahren. Sie ist wesentlich für die Modellierung kompakter astrophysikalischer Objekte wie Kernkollaps-Supernovae, Neutronensternen und ihre Verschmelzung. Sie bestimmt ebenfalls die Bedingungen für die Enstehung der Elemente im Universum, insbesondere für den r-Prozess, dessen astrophysikalischer Ort noch debattiert wird. Daher ist die Zustandsgleichung ein aktives Thema der theoretischen und experimentellen Forschung.

Gegenwärtig ist eine realistische und quantitative Beschreibung dichter Materie von ersten Prinzipien unter Verwendung der grundlegenden Theorie der Quantenchromodynamik nicht verfügbar. Daher wurden eine große Vielfalt phänomenologischer Modelle zur Beschreibung nuklearer Systeme entwickelt. Diese Modelle hängen von einer Anzahl von anzupassender Parameter ab, die durch Daten bestimmt werden müssen. Für die weitere Entwicklung des Feldes ist es entscheidend, die realistischsten Parametersätze zu bestimmen und sie konsistent zu verwenden. Neue Einschränkungen kommen von astrophysikalischen Beobachtungen und Laborexperimenten, die uns ermöglichen, bessere modelle bereitzustellen, die in vielen Studien, sowohl für Kernstruktur- und astrophysikalischen Anwendungen, verwendet werden können.

In dieser Arbeit wird ein erweitertes relativistische Mittelfeldmodell, das dichteabhängige nichtlineare Ableitungsmodell oder kurz DD-NLD Modell, entwickelt. Bei den nuklearen Selbstenergien wird eine Energieabhängigkeit eingeführt, um das experimentelle Verhalten des optischen Potentials zu reproduzieren. Das Modell wird auf die Beschreibung von unendlicher Kernmaterie, mit Schwerpunkt auf die Hochdichteregion oberhalb der Sättigungsdichte, angewendet sowie für die Neutronstern-Zustandsgleichung bei verschwindender Temperatur. Um die Modellparameter zu bestimmen, werden Kernmaterieparameter bei Sättigungsdichte sowie Eigenschaften mehrerer Atomkerne, darunter Bindungsenergien, Ladungs- und Diffraktionsradien, Oberflächendicken, etc., angepasst. Die erhaltenen Parametersätze werden verwendet, um die Masse-Radius-Beziehung von Neutronensternen durch Lösen der Tolman-Oppenheimer-Volkoff-Gleichungen zu bestimmen. In diesen Untersuchungen wird das DD-NLD-Modell nur für nukleare Systeme bei verschwindender Temperatur betrachtet. Für allgemeine astrophysikalische Anwendungen jedoch, z.B. für die Bereitstellung von Zustandsgleichungstabellen für Simulationen von Kernkollaps-Supernovae, ist es notwendig, die theoretische Beschreibung auf endlichen Temperaturen zu erweitern. Zu diesem Zweck wird das temperatur-erweiterte Modell entwickelt. Dieses ermöglicht, die Eigenschaften homogener Kernmaterie bei kleinen Temperaturen bis zu 15 MeV zu studieren und dabei den vollen Bereich der Isospinasymmetrie von Neutronenmaterie über symmetrische Materie bis zu Protonenmaterie abzudecken. Der Flüssig-Gas Phasenübergang und die spinodalen und binodalen Gebiete der Instabilität bzw. Koexistenz von Phasen werden untersucht. Wir diskutieren den Einfluss der energieabhängigen Selbstenergien im Zustandsgleichungsmodell mit steigender Temperatur und deren Effekte auf den Flüssig-Gas Phasenübergang.

# Acknowledgments

Here I want to thank all the people that helped me during my Ph.D. studies, either by directly contributing to this work or by supporting my research and studies in any way.

First of all, I warmly thank my mentor, Dr. Stefan Typel, for the opportunity I was given to work on one of the exciting topics of today's nuclear physics. I am grateful for all the support and encouragement I received during the period of my Ph.D., and I appreciate the time and effort invested in helping me through these years. It was a pleasure to work with such a person and I have learned more than I could have hoped for.

Further, I want to thank my supervisor, Prof. Dr. Karlheinz Langanke, for all the support and time provided despite an already busy schedule. Thank you for the advice and suggestions and for being a person to whom I could rely on. Many thanks to Prof. Dr. Gabriel Martinez-Pinedo for taking over a role as a member of my Ph.D. committee, for funding my research through the Nuclear Astrophysics Virtual Institute (NAVI) project and overall for maintaining a good connection between the GSI Theory group and the Nuclear astrophysics group of TU Darmstadt by including me in their activities. I also want to thank Prof. Dr. Tetyana Galatyuk and to Prof. Dr. Michael Vogel for taking part in my Ph.D. defense as the members of the examination committee.

Thanks to the Helmholtz Graduate School for Hadron and Ion Research (HGS-HIRe) and its members for all the good time and interesting weeks we have spent in learning and growing together. I am grateful for the given opportunity and funding provided to attend some of the great meetings, conferences and summer schools during this period, as well as for granted collaboration possibility through the HGS-HIRe Abroad program. With that, I would like to thank my collaborators, Dr. Helena Sofia de Castro Felga Ramos Pais and Prof. Constança Providência from The Centre for Physics of the University of Coimbra (CFisUC) in Coimbra, Portugal, for a warm welcome in their research group, interesting discussions we had during my visit and time and patience they both invested in making our work together a joyful experience.

The last three and a half years that I have spent in Darmstadt have been an unforgettable experience that I will always remember with a smile on my face. Among the pleasant working environment, many opportunities for improvement and learning, and some hard working hours, what I will mostly remember this city for are many wonderful people that I have met during this period. I want to thank my colleagues and friends from the Theory Department of GSI for their everyday company and, in general, for maintaining good atmosphere during working hours, making it enjoyable to be a part of the group. Thanks to all the other once colleagues - now friends, Cesar, Tona, Samuel, Gabor, Enrico, Xiaoyu, Daria, Andrea, Olga and many more working at GSI and at Universities around, for your smiley faces on the early morning bus, complains and grumbles we often shared as well as many laughs, late evenings out and good times. Also, for all the fun, knowledge and experiences shared, a big thank you to Kevin, Marius, Marco, Debarati, Toño and all the other young researchers around the world that I have met while attending many schools and workshops. I hope you will keep making this nuclear physics/astrophysics community as amazing as it was during the years of my Ph.D. Not to forget the wonderful people I have shared my living space with over the years, thank you Dimitri, Romain, Patricia, Mehdi and Amanda, for making everyday life an adventure and for being my second family away from home.

Finally, I want to thank my family, my parents, my sisters and my brother for being there for me when needed, and to my friends in Croatia, for the support and believing in me, for the encouragement to pursue my path away from home and for staying by my side after all these years of my often absence and busy schedule. It is a true joy to still have you all around on my rare visits home. You all have a part in this, and I want to thank you for that.

# Contents

# 1 Introduction

Nuclear matter is an interesting subject of study for many research fields in physics, from condensed matter to Lattice Quantum Chromo-Dynamics (QCD)[1]. It is an idealized system composed of interacting neutrons and protons, studied over a wide range of baryon densities $\rho_B$ and temperatures T and a topic of intense research in nuclear physics for decades. On Earth, nuclear matter is present in the interiors of atoms where it builds up their nuclei. The nucleus holds 99.9% of the atom's mass within a volume with a radius of $1/100,000$ the one of an atom. As a consequence matter inside a nucleus has a very high density, more than $10^{14}$ times the one of normal matter, e.g. water, and it is the densest substance known to naturally exist on Earth. In search for other natural environments of such and even higher densities we look toward different places in the Universe. A well known source of extremely high densities are compact astrophysical objects such as neutron stars (NS) [1, 2, 3, 4], final remnants of the collapse of a massive star. In this scenario, the core of a massive star collapses under gravity and explodes as type II or core-collapse supernovae (CCSN) [5, 6, 7, 8, 9, 10] producing high densities and temperatures while forming a proton-neutron star (PNS) [11, 12] that eventually becomes a NS or a black hole (BH). Similar temperatures and densities, along with higher isospin asymmetries (excess of neutrons over protons), are reached during the merging of two NSs (NS-NS) or NS and BH (NS-BH) in a close binary system [13, 14, 15]. Valuable data is collected through observations of CCSN and NSs in different environments and at different evolution stages. Still, the information collected in this way is limited because of observational difficulties and the rare events provided by nature. Therefore, we don't count only on natural sources as possible sites to explore high density matter. Within a laboratory environment, compressed matter is produced through nuclear collisions where two ions are accelerated and smashed against each other. In such reactions we create a system that lets us study nuclear matter properties for a very short period of time before expanding. Depending on the mass of the colliding nuclei, on their energy and on impact parameter, nuclear matter in a wide range of temperatures and densities is accessible.

Nuclear matter densities range from the saturation density $\rho_0$ found in the interiors of nuclei up to several times that value reached in CCSN and going as high as ten times the saturation density, possible to exist in NS cores and to be reached in heavy-ion collisions (HIC) [16, 17] (summarized in Table 1). For temperatures reached in these scenarios, it is important to have in mind that we are talking about temperatures on a nuclear scale, generally expressed in MeV. The temperature of a star, e.g. the core of the Sun, has a value of about $1.5 \cdot 10^7$ K which we consider pretty hot. However, this temperature corresponds to $10^{-3}$ MeV ($1\ K \simeq 8.6 \cdot 10^{-11}$ MeV) on the nuclear scale, which is negligible compared to the binding energy per nucleon in the nuclear matter ($E_B \sim 16$ MeV) or in a nucleus ($E_B \sim 8$ MeV). Since the nuclear temperature scale goes up to $\sim 200$ MeV in CCSN or NS mergers, the Sun, as well as most NSs with temperatures of few 10 or 100 keV, are considered to be cold and are approximated in model calculations with $T = 0$ MeV. For many other astrophysics scenarios temperature does play a role,

[1] A well-established non-perturbative approach for solving the QCD theory of quarks and gluons. It is a lattice gauge theory formulated on a grid or lattice of points in space and time.

**Table 1:** Typical densities of different systems.

| System | Density | |
|---|---|---|
| | [g/cm$^3$] | [fm$^{-3}$] |
| Water | $\sim 1$ | $\sim 5 \cdot 10^{-13}$ |
| Nuclei (saturation density $\rho_0$) | $\sim 3 \cdot 10^{14}$ | $\sim 0.16$ |
| Supernovae explosions | up to $\sim 10^{15}$ | up to $\sim 0.5$ |
| NS cores and HIC | up to $\sim 3 \cdot 10^{15}$ | up to $\sim 1.5$ |

**Table 2:** Temperature scale of nuclear systems.

| Nuclear system | Temperature [MeV] |
|---|---|
| Sun | $\sim 10^{-3}$ |
| Neutron stars | $\sim 10^{-2}$ |
| Supernovae explosions | $\sim 10-20$ |
| Heavy-ion collisions | $\sim 10-200$ |

e.g. in studies of the NS crust at sub-saturation densities where the existence of inhomogeneous nuclear matter and cluster formation is expected, or in CCSNe where associated temperatures reach 10 to 20 MeV. Much higher temperatures are reached through high-energy HICs which investigate nuclear matter under very extreme densities and temperatures as their primary goal. The temperature scale of nuclear systems is summarized in Table 2.

Temperature T and the net baryon density $n_B$ are the two parameters we mentioned so far in order to specify different sites and conditions in which dense nuclear matter exists or can be produced. These parameters characterize the phase diagram of nuclear matter, known also as the QCD diagram of strongly interacting matter given in figure 1. It sums up the major phase structures and phase transitions of strongly interacting matter. Cold nuclear matter, as found in normal nuclei with net baryon density equal to saturation density, consists of nucleons only. At moderate temperatures and densities, nucleons are excited to short-lived states (baryonic resonances) which can decay, e.g. by the emission of mesons. At higher temperatures also baryon-antibaryon pairs are created. The mixture of strongly interacting baryons, anti-baryons and mesons is in general called hadronic matter, represented by the white area in figure 1. At either very high temperatures or densities, the hadrons melt into quarks and gluons and new phases of nuclear matter are formed. For the high-temperature region, results of Lattice QCD [19] indicate that at zero net-baryon density, close to the T axis, the transition from hadronic to deconfined matter occurs in a crossover at a temperature $T_C$, which is equal to $T_C = 154 \pm 9$ MeV [20], the temperature above which deconfined matter of quarks and gluons, the so-called Quark-gluon plasma (QGP), appears. It is expected that the QGP at extremely high temperature and high energy density existed in the early universe during a few micro seconds after the Big Bang. Major research efforts, the advance of technology and the availability of enlarged accelerators have resulted in at first an announcement of

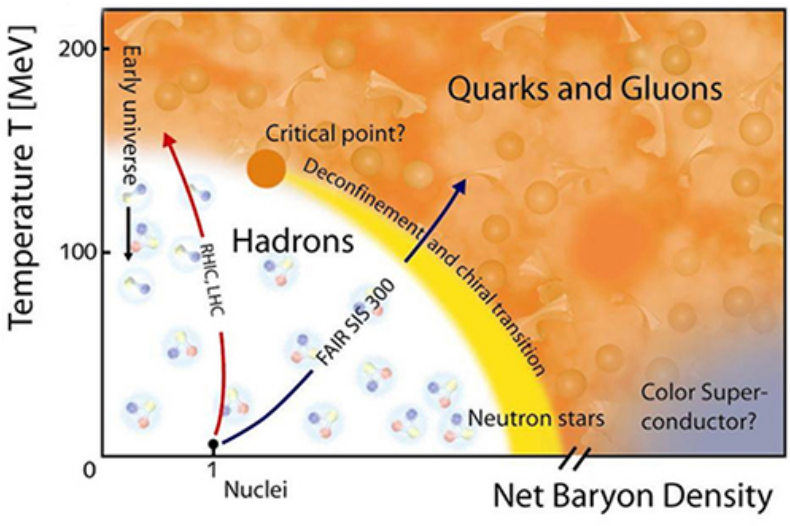


**Figure 1:** The QCD phase diagram as conceived today, with the net baryon density and temperature T on x and y axes, respectively. Taken from [18].

indirect evidence for a “new state of matter” by the European Organization for Nuclear Research (CERN) [21] in the year 2000 [22, 23], and later in 2010 by creation of QGP at the Relativistic Heavy Ion Collider (RHIC) [24] at Brookhaven National Laboratory (BNL) [25, 26, 27]. The high-density region of the QCD phase diagram could be an origin of even more exotic phases, like color superconductivity formed by correlated quark-quark pairs. It is a phenomenon predicted to occur in quark matter if the net-baryon density is sufficiently high (well above nuclear density, as indicated in Figure 1) and the temperature is low, which on a nuclear scale can be often approximated with $T = 0$ MeV. The only known site in the universe where these conditions are possibly fulfilled is in the core of a compact star, that is a NS, which opens a possibility that their cores contain quark matter in a color superconducting state [28, 29, 30, 31]. At present, neither experiments nor the lattice QCD provide a clear guide on the density for which the expected phase transition to quark matter at low temperatures would occur. The occurrence of quark matter in the core of a NS is only one of the possibilities. Already at the densities of two to three times $\rho_0$ we can not be sure about the composition of matter. There are different models suggesting ”traditional“ homogeneous nuclear matter composed mostly of neutrons, with some fraction of protons and electrons, but at such high densities, additional particle species are expected to occur [1, 2]. More exotic scenarios are possible such as matter containing mesons, e.g. pions or kaons in addition to neutrons, that can possibly form condensates at low temperatures [1], hyperons [32, 33] (baryons that contain one or more strange quarks, e.g. $\Sigma$, $\Lambda$, $\Xi$), more massive baryon resonances (e.g. $\Delta$) or, as already said, dense quark-degenerate matter. All of the possibilities which involve fermions may also show superconductivity. An overview of the wide range of possibilities is depicted in figure 2. The most promising frontier for probing the composition of the NS core is through the various NS observations, among which the cooling of isolated neutron stars [34], the cooling of the crust of a low-mass X-ray binary which was recently accreting but entered a quiescent (non-accreting) period, X-ray bursts and superbursts, NS oscillations including r-modes [35, 36] and magnetar flare oscillations [37]. All of these observations are potentially sensitive to the core composition.

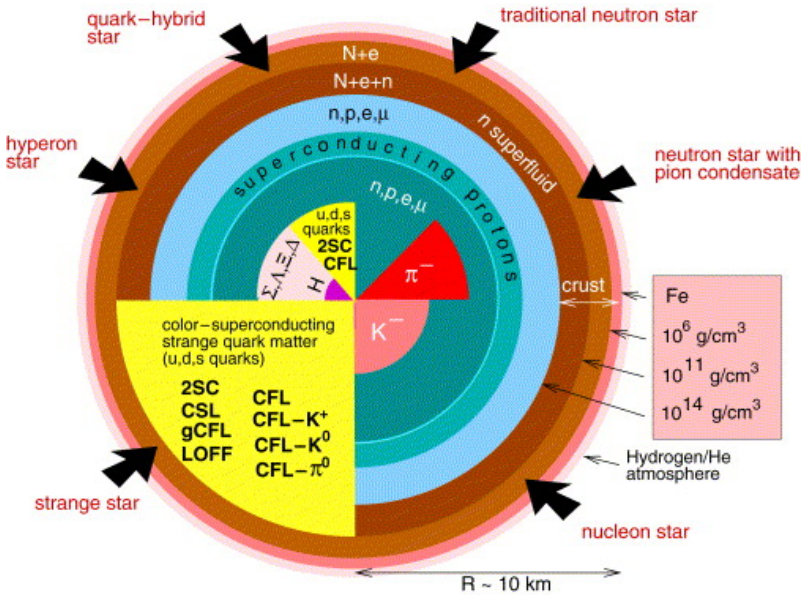


**Figure 2:** The composition of matter in the NS with different composition scenarios for the NS core. Besides the possible phases mentioned in the text, the color-flavor locked (CFL) phase of color-superconducting strange quark matter is also shown as one of the options, where various condensation patterns such as the CFL-$K^0$, CFL-$K^+$, CFL-$\pi^0$, gapless color-spin locked (CSL) phase, and crystalline pairing (LOFF) phases are possible. The figure is taken from [38], where more details and further references can be found for specific cases.

The general question is "What is the purpose of studying dense matter properties?" The phase diagram, phase structures and phase transitions of strongly interacting matter are among the fundamental issues of nuclear physics. Therefore, the topic is relevant for multiple open questions, such as understanding the basic theory of strong interaction - QCD, the mechanism of color confinement, the early history of our universe, its formation and evolution, explosion mechanism of supernova, the structure and evolution of compact stars etc. For that purpose, what we actually study are the thermodynamic properties of matter in different conditions and phase transitions between different states of nuclear matter, both in the ground state and in a hot and dense state. The thermodynamic properties of highly compressed dense matter are characterized, among others, by the equation of state (EOS), one of the most basic properties of matter given by the dependence of pressure on density and temperature. It is an essential ingredient for numerous applications, e.g. it determines the dynamical evolution of violent events such as CCSN and NS mergers, defines the structure of the emerging compact stars and impacts the conditions for nucleosynthesis and the emerging neutrino spectra. This makes the EOS modeling one of the main concerns of nuclear astrophysics in the recent years, resulting in many approaches for the description of dense matter from both purely theoretical and phenomenological perspectives. Numerous laboratory experiments and astronomical observations are conducted in order to constrain the parameters of various EOS models and to provide the EOS of stellar matter in conditions relevant to the description of compact stars, CCSNe and NS mergers [39, 40, 41]. The construction of the EOS is a very challenging task that has to take into account many degrees of freedom and cover a wide range of values for thermodynamic variables, that is for baryon density $\rho_B$, temperature $T$ and isospin asymmetry $\delta = \frac{\rho_n - \rho_p}{\rho_B}$ (where $\rho_n$ and $\rho_p$ are standing for neutron and proton densities), depending on the problem in question. Building the EOS model is the main preoccupation of the first part of this work where the aim is to develop a very general EOS describing nuclear and stellar matter properties while agreeing with known constraints from different experiments and observations. One of the applications of the developed EOS is to consider its behavior for infinite nuclear matter and neutron stars, cases of very high density and zero temperature, covering the whole range of asymmetries. The EOS developed in the first part of the work is focused on the high-density nuclear matter region, where its stiffness plays an important role in satisfying the known constraints. The second part of this work, the new EOS is implemented to the low-density nuclear matter at finite temperatures of values up to $T \sim 20$ MeV. These are the conditions in which we expect the liquid-gas phase transition of nuclear matter to occur. It is also an important subject on its own, regardless of the astrophysical application, since coexisting phases are a very general phenomenon. Its importance in the context of compact stars will be further discussed in chapter 7.

The present thesis is organized as follows. In chapter 2 we are introducing the EOS as a basic ingredient needed to describe nuclear matter. Different models widely used today are listed and the basic set of characteristic EOS parameters are presented. The constraints on these parameters are discussed, coming from observations of NSs and many different laboratory experiments. Chapter 3 presents the formalism of standard relativistic mean-field (RMF) models as well as the extensions developed through the years for a better description of nuclear matter. One of them is introducing density-dependent (DD) meson nucleon couplings, presented more thoroughly in chapter 3.4. The main point of this work is reached in chapter 4 where the generalized RMF model formalism that includes an energy dependence of the nucleon self-energies is presented. The extension is introduced in order to reproduce the optical potential of nucleons in nuclear matter extracted from experimental data of elastic proton scattering on nuclei. The adjustments of developed model to describe stellar matter as well are considered in section 4.5. The following chapter provides the parametrization procedure of fitting model parameters to nuclear matter properties at the saturation density as well as selected properties of several finite nuclei. The new development of the present work is to combine the generalized non-linear derivative meson-nucleon couplings with a density dependence and to determine the parameters of the phenomenological model from a fit to properties of finite nuclei which has not been done before. Finally, the application of the developed EOS model to infinite nuclear matter as well as NSs is presented in chapter 6 and the results of the calculations are discussed. In chapter 7 we introduce the temperature dependence and discuss the

thermodynamics of nuclear matter for temperatures up to $\sim 20$ MeV. We are investigating the region of instability between the gas and liquid phases in nuclear matter and look for the transition densities. At last, we summarize our results, draw conclusions and give an outlook to possible future work in chapter 8.

# 2 Equation of state (EOS) of dense matter: models and constraints

The EOS for dense matter can be very complicated with dependencies on many variables. The requirements on the EOS are different depending on the astrophysical situation to which they are applied. The most general EOS for applications in astrophysics requires e.g., a dependence of pressure on baryon density $n_B$ and additionally on temperature T and proton fraction $Y_p = \frac{1-\delta}{2}$ ($\delta = 1$ for pure neutron and $\delta = -1$ for pure proton matter), giving $P = P(n_B, T, Y_p)$. Such EoSs, that cover the full thermodynamic parameter range of temperature, density and isospin asymmetry are called "general purpose EoSs" and are able to describe cold NSs, NSs in binary mergers and CCSNe. The necessary ranges of thermodynamic variables are 0 MeV $\leq T <$ 150 MeV for temperature, $10^{-11}$ fm$^{-3}$ $< n_B <$ 10 fm$^{-3}$ for baryon density and $0 < Y_P < 0.6$ for proton (electron) fraction. The overview of currently available general purpose EoSs is given in the reference [42].

For the purpose of this work it is not necessary to take into account the full range of the mentioned thermodynamic variables, which already simplifies the task. The goal of the first part of this work is to provide a model that describes infinite nuclear matter and NSs. Immediately it is evident that the assumption $T = 0$ simplifies the problem significantly. We are keeping the wide density range, while the proton fraction can be taken in the full range from 0 (neutron matter) to 1 (proton matter) in the case of theoretical infinite nuclear matter. $Y_q$ is determined by the $\beta$-equilibrium and charge neutrality conditions in NSs that have to be fulfilled for stellar matter, as it will be further discussed in chapter 2.2.2. As a note, the model we are developing is quite general and in principle it could be extended to describe the full range of thermodynamic variables in the future. For now, only the extension to low temperatures is done in the second part of this work where we will discuss the thermodynamics of infinite nuclear matter for the low density (0 fm$^{-3}$ $< n_B \lesssim$ 0.2 fm$^{-3}$) and low temperature (0 MeV $< T \lesssim$ 20 MeV) region, in search for the liquid-gas phase transition. Depending on the application, there is a vast number of theoretical EOS models developed through the years. Let us present in quite a general manner some of the various approaches that exist and are used today in order to describe dense matter.

## 2.1 Various approaches to describe dense matter

The theoretical description of strongly interacting matter has to capture the essential thermodynamic properties of the many-body system. This is a very challenging task, since there are many things to be taken into account. The relevant degrees of freedom have to be identified, that is which particle species are contributing to the nuclear matter content. As we discussed already, at high densities and/or temperatures many exotic particles can appear, while at low densities and temperatures (as in the NS crust) nuclei are present. However, the simple approach to nuclear matter based on nucleons may suffice in many cases and it is often a prevailing choice. The main effort is to specify the interactions between the constituents of nuclear matter, which requires a nontrivial effort since the strong interaction is of a very complex nature. Traditionally, nuclear physics wants to understand the properties of atomic nuclei in terms of the "bare" interaction between pairs of nucleons. With the emergence of QCD, it became clear that the nucleon-nucleon (NN) interaction is not fundamental. Despite the efforts to describe nuclear matter within QCD, there is no *ab initio* model available yet for the thermodynamic conditions characteristic for NSs or CCSNe. For that reason, in nuclear physics even today one assumes the nucleons to be elementary particles.

Different approaches to describe nuclear matter are developed through the years, depending on the degrees of freedom, the interaction and the selection of the many-body method to be used. We will divide them in two separate categories:

1. *Ab initio many-body methods*, which assume realistic few-body NN interaction (two- and three-nucleon forces) designed to describe NN scattering in vacuum and properties of light nuclei. The many-body problem can then be treated with different techniques, some of which are listed in the reference [42].

2. *Phenomenological approaches* are on other hand based on the effective interactions and depend on a number of parameters (usually between $10-15$) fitted to nuclear matter properties and selected properties of several nuclei over the full nuclei chart. Today, these approaches are interpreted in terms of energy density functional (EDF) theory and are the most widely used methods in construction of astrophysical EOSs.

The oldest attempt to explain the nature of NN-interaction was made in 1935 by Yukawa [43]. He proposed the first significant theory of strong interaction by stating that the nucleons are holding together through the exchange of a virtual massive particle, the pion. This model successfully explained the range of the nuclear interaction and since then many phenomenological models have been developed based on Yukawa's idea of meson exchange. When hadrons are treated as elementary particles, the meson-exchange concept still represents the best working model for quantitative NN potentials.

There are some basic considerations about the NN interactions. For few-body systems like light nuclei it is usually enough to define the dominant two-body interaction between nucleons to describe them. The three-body interaction starts to matter at high densities where their contribution is necessary in order to reproduce the saturation properties of nuclear matter. The interaction between more nucleons is hard to construct and can be neglected in many circumstances. There are different approaches to obtain phenomenological forces between nucleons. The first approach includes the meson exchange models based on the idea of Yukawa like e.g. classical Nijmegen interactions, the Paris NN potential, Bonn potential etc. The second approach consists the potential models that adopt a sum of local operators (the essential ones are central, tensor and spin-orbit terms) in addition to the well established long-range one-pion exchange (e.g. the Urbana and Argonne potentials). A more detailed overview of the mentioned models with references is given in the review paper [42]. These models all share one pion exchange (OPE) at long distances but have model-dependent mid-range attraction and short-range repulsion. They can have 20 to 60 adjustable parameters fitted to several thousand data points of nucleon-nucleon scattering. However, when applied to systems with many interacting particles, we are restricted by computational challenges as the model space explodes rapidly. To deal with this we need approaches that will avoid an exact treatment of all interactions among the active particles and focus only on the degrees of freedom identified as important ones. For this purpose different many-body methods to treat homogeneous matter are developed.

A widely used method to treat the interacting many-body system in physics is through the concept of a "mean-field". The idea is to describe the interaction of one particle with all the remaining ones through the average potential that the remaining particles are creating, instead of summing up all two-body interactions among the constituents of the many-body system. The method to treat such a system is then called mean-field (MF) approximation. Originally, it corresponds to the Hartree approximation, where the many-body state is written as a simple product of single particle wave functions,

$$\Psi(r_1, r_2, \dots r_N) = \Psi_1(r_1)\Psi_2(r_2)\dots\Psi_N(r_N)\,. \tag{1}$$

However, the term is often used to denote the Hartree-Fock (HF) approximation, too. Although the Hartree equations are numerically tractable via the self-consistent mean-field method, such a crude approximation unsurprisingly fails to capture elements of the essential physics. The Pauli exclusion principle demands that the many-body wave-function must be antisymmetric with respect to interchange of any two particles, (e.g. $\Psi(r_1, r_2, \dots r_N) = -\Psi(r_2, r_1, \dots r_N)$ ), which is clearly not fulfilled by a wave-function of the form (1). To satisfy the exchange condition a Slater determinant of single particle orbitals is formed

$$\Psi(r_1, r_2, \dots r_N) = \frac{1}{\sqrt{N}}\mathscr{A}|\Psi(r_1)\Psi(r_2)\dots\Psi(r_N)| \tag{2}$$

where $\mathscr{A}$ is an anti-symmetrising operator; i.e. it ensures that all possible anti-symmetric combinations of orbitals are taken into account with the proper sign. This leads to the single particle HF equations that

have an additional exchange term that manifests the Pauli exclusion principle and adds considerably to the complexity of the equations. Even though the HF equations deal with exchange exactly the more detailed correlations, like short-range correlations between the particles arising from their mutual interaction, are neglected. Because of that, even though the method is in general very successful in atomic physics and chemistry, in nuclear systems the HF method isn't sufficient to reproduce known properties of nuclear matter. There are two ways to overcome this problem:

- we can explicitly include correlations within the many-body approaches
- or use an effective, usually medium dependent interaction within the HF approach instead of the realistic few-body one.

The first option offers several different theoretical *ab-initio* frameworks in which the correlations can be included in the strongly interacting many-body system. The general idea of different approaches is given in reference [42]. Here, we are just mentioning some of them, as: Self-consistent Green's function (SCGF) method, Brueckner-Hartree-Fock (BHF) approximation, Quantum Monte Carlo methods, Chiral effective Field theory ($\chi$EFT), Lattice methods etc. Among these approaches, let us point out the Dirac-Brueckner Hartree-Fock (DBHF) approach [45, 46, 47], the relativistic version of BHF method that we will refer to later in the text. The main advantages of DBHF are that an additional repulsion at high densities is obtained, since part of the three-body interaction is automatically generated, and that the problem of non-relativistic BHF calculations, which can result in a superluminal speed of sound at the high central densities of massive NSs, is avoided.

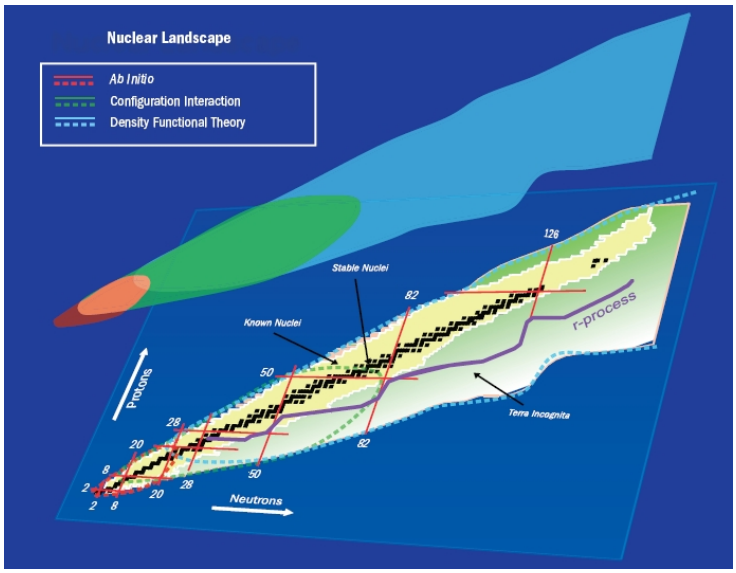


**Figure 3:** Theoretical methods and computational techniques used to solve the nuclear many-body problem. The black squares in the (N,Z)-plane represent stable nuclei, yellow squares indicate unstable nuclei produced and studied in the laboratory while the green ones are unstable nuclei yet to be explored (terra incognita). The thick dotted lines indicate domains of major theoretical approaches to the nuclear many-body problem. For the lightest nuclei, ab-initio calculations based on the bare nucleon-nucleon interaction, are possible (red). Medium-mass nuclei can be treated by configuration interaction techniques (in green), a method that involves diagonalization of the Hamiltonian within a basis constructed by the configuration-interaction (CI) shell model approach. The CI shell model provides an attractive framework as it accounts for both shell effects and correlations. However, combinatorial growth of the dimension of the many-particle space hinders its application in mid-mass and heavy nuclei. For those, the density functional theory based on self-consistent/mean field theory (blue) is the tool of choice. Taken from [44].

As a second approach, the requirement for a computationally applicable scheme that successfully incorporates the effects of both exchange and correlation leads us to consider the conceptually simple and elegant density functional theory (DFT) [48, 49]. This kind of approach to many-body quantum systems is used in many other fields, such as condensed matter physics and quantum chemistry, where it was originally developed. The DFT provides a powerful and perhaps unique framework for the accurate calculation of the ground-state properties and collective excitations of medium-to-heavy nuclei (see figure 3. By the minimization of a suitable functional of the density, the complicated many-body wave function is "reduced" to the much simpler one-body density and provides the ground state energy. The price of this simplification is that DFT does not offer any guidance on how the density functional has to be built. Nevertheless, the constraints coming from measurable quantities and our physical intuition are good enough to construct realistic functionals. DFT is still the only microscopic approach that is applicable to the entire nuclear landscape and NSs. The phenomenological calculations developed in this framework are based on the use of effective nuclear interactions. In the past decades numerous *energy density functionals* (EDFs) have been proposed and we can group them in two main branches: non-relativistic and relativistic. The main distinctions between them are the specific form of the interaction and the resulting dispersion relation of the quasi-particles. Non-relativistic approaches start with Hamiltonian for the many-body system with usual kinetic and potential terms. The potential term contains two- and three- body interactions and it changes with the model. There are certain assumptions for the many-body wave-function form under which the energy of the system is calculated, normally within the HF approximation. The non-relativistic models however tend to fail in the description of high density matter. The most popular non-relativistic functionals in the HF frame are of Skyrme- [50, 51] (with zero range effective interaction) and Gogny- [52] (the finite range approach) type where nucleons interact via density-dependent effective potentials. The functional form is here well established and the parameters are constrained by nuclear experiments, while we have ad-hoc density dependent terms ($\sim n^{\gamma}$) which simulate many-body effects. Arbitrariness is present in the functional form and in the extrapolations. On the other hand, relativistic mean-field (RMF) models, developed in the 1970s and widely used ever since, are based on a quantum field theory, having nucleons represented by Dirac four spinors $\Psi_i$ and interacting via the exchange of various mesons. This description, called quantum hadro dynamics (QHD) [53, 54, 55, 56], was originally seen as a fully field theoretical approach and treated with the respective formalism. Later, the view of an effective description to be applied in rather simple approximations prevailed since nucleons as composite objects cannot be considered as fundamental degrees of freedom. These models had a great success and provided a covariant description of both finite nuclei and nuclear matter. We will introduce the RMF models in detail in the next chapter. The RMF model is a good starting point as a framework of hadronic systems that include nuclei and nuclear matter. Many extensions of RMF models, addressed in chapter 3.3, were developed in recent years to provide better agreement with experiments. The extended models are still prone to improvement and this is an ongoing effort as it will be presented in this work. Before describing the RMF model in more detail, we will introduce more closely the properties of the many-body systems and sketch some of their basic features in the following.

## 2.2 Basic features of dense matter

The first step in studying strongly interacting matter is often the investigation of homogeneous matter at vanishing temperature. Let us introduce the subjects of our study, the infinite nuclear matter and NS matter in more detail.

### 2.2.1 Infinite nuclear matter

The simplest, yet already highly non-trivial system, is infinite nuclear matter. The infinite system is homogeneous and isotropic and therefore the wave functions are given by plane waves $e^{i\vec{k}\vec{x}}$ when there

is no explicit nucleon-nucleon correlations. The density of particles is obtained as a sum over all occupied states inside the phase space volume $(2\pi)^3$

$$\rho = \frac{N}{V} = \sum_{k,\lambda} \Psi^*_{k,\lambda}(\overrightarrow{r})\Psi_{k,\lambda}(\overrightarrow{r}) \rightarrow \frac{\gamma}{(2\pi)^3}\int d^3k \;\; n(\overrightarrow{k}) \,. \tag{3}$$

In the continuum limit the sum in eq. (3) is replaced by the integral over the momentum distribution $n(\overrightarrow{k})$. Since we deal with fermions the quantum states inside the volume $(2\pi)^3$ have to be different. Therefore all states $\overrightarrow{k}$ are occupied up to the Fermi momentum $k_F$. The distribution of occupied states is given by the Fermi sphere with radius $k_F$

$$n(\overrightarrow{k}) = \Theta(k_F - |\overrightarrow{k}|) \,. \tag{4}$$

The evaluation of eq. (3) leads to the following relation between density and Fermi momentum

$$\rho = \frac{\gamma}{6\pi^2} k_F^3 \tag{5}$$

where $\gamma$ is a degeneracy factor. For isospin symmetric nuclear matter (SNM) that has equal number of protons and neutrons $\gamma = 4$, which means that each momentum state $\overrightarrow{k}$ can be occupied by four states that belong to proton and neutron, both of spin up/down. Consequently, for pure neutron matter the spin-isospin degeneracy is $\gamma = 2$.

To describe the properties of the infinite nuclear matter we are using the EOS, that is energy density $\epsilon$ or pressure $P$ as a function of baryon density. Both descriptions are equivalent since $\epsilon$ and $P$ are related through thermodynamical relations. The energy density is simply given as the sum of kinetic energy (in non-relativistic approximation) and the mean field

$$\epsilon(\rho) = \frac{\gamma}{(2\pi)^3}\int d^3k \; \frac{\overrightarrow{k}^2}{2M} \, n(\overrightarrow{k}) + U[\rho(\overrightarrow{r}_i)] \tag{6}$$

where the mean field part $U[\rho(\overrightarrow{r}_i)]$ is the average potential that particle $i$ at the position $\overrightarrow{r}_i$ feels coming from the remaining $j$ particles

$$U[\rho(\overrightarrow{r_i})] \quad \rightarrow \quad U(\overrightarrow{r_i}) = \sum_j V(\overrightarrow{r_i}, \overrightarrow{r_j}) \tag{7}$$

and it depends on the particle density (eq. 3) at its position. It is often more practical to use the energy per particle $E/A$ instead of energy density to characterize nuclear matter, $E/A = \epsilon/\rho$. The most fundamental aspect of the nuclear matter EOS is the phenomenon of saturation. From the existence of stable nuclei it follows that the energy per particle, $E/A$, must have a minimum. This point is called saturation point and the density at which this minimum occurs was already introduced as saturation density, $\rho_0$. It is the density in the interior of heavy nuclei. e.g. in $^{208}$Pb, with typical value e.g. $\rho_0 = (0.160 \pm 0.005)$ fm$^{-3}$ [57] or $\rho_0 = (0.152 \pm 0.008)$ fm$^{-3}$ [58].

The energy per nucleon $E/A$ at this point can be derived from the Weizsäcker mass formula

$$E = a_V A - a_S A^{\frac{2}{3}} - a_C \frac{Z^2}{A^{1/3}} - a_A \frac{(N-Z)^2}{A} \pm \delta(A,Z) \tag{8}$$

for the energy E of nuclei with mass number $A = N + Z$, neutron number N and charge number Z. There are five terms that provide a rather accurate fit of energies across the periodic table of nuclei. The first term is the volume term, describing the nuclear bulk properties, i.e. the conditions in the interior of a

heavy nucleus. It is caused by the attractive strong forces between the nucleons and it is proportional to A since strong force has a very limited range which means that a given nucleon may only interact with its direct neighbors. The coefficient $a_V$ is usually about $\sim 16$ MeV. Next is the surface term also based on the strong force that is, in fact, correction to the volume term. It accounts for the surface tension and is therefore proportional to the surface area $A^{2/3}$. The Coulomb term describes the Coulomb repulsion between the uniformly distributed protons and is proportional to the number of proton pairs, $Z^2$ with $R \sim A^{1/3}$. This effect lowers the binding energy because of the repulsion between charges of equal sign. The asymmetry term, that scales with the difference of proton and neutron numbers $(N-Z)^2$, is based on the Pauli exclusion principle (no two fermions can occupy exactly the same quantum state in an atom) and the isospin symmetry of the strong force. The heavier nuclei contain more neutrons than protons which is necessary for the stability since neutrons provide some compensation for the repulsion between protons via the attractive forces between neutrons and protons. The last term is pairing term that captures the effect of spin-coupling. Nuclei with an even number of protons and an even number of neutrons are more stable thanks to the occurrence of 'paired spin'. On the other hand, nuclei with an odd number of protons and neutrons are less stable. With the aid of the Weizsäcker formula the binding energy can be calculated fairly well for nearly all isotopes but shell effects are missing. In order to calculate the binding energy, the coefficients $a_V$, $a_S$, $a_C$, $a_A$ and $a_P$ must be known. They are determined by a fitting to experimentally measured masses of nuclei. For infinite, isotropic and homogeneous nuclear matter that we consider, only the volume and asymmetry terms contribute in the limit $A \to \infty$ (neglecting the Coulomb contribution) and the Weizsäcker mass formula gives us a value of $E/A \simeq -16$ MeV at the saturation point for symmetric matter $(N = Z)$. Therefore, in order to have a realistic density functional we have to meet the nuclear saturation properties, the given values of energy per nucleon and the nuclear saturation density.

Properties of nuclear matter are usually characterized by a number of parameters that are related to the leading contributions in a Taylor expansion of the energy per nucleon around the saturation point

$$E(x,\delta) = E_0(x) + E_{sym}(x)\delta^2 + \mathcal{O}(\delta^4) \tag{9}$$

where $E = \epsilon/n_B$, $x = \frac{\rho_B - \rho_0}{\rho_0}$ is the density deviation and $\delta = \frac{\rho_n - \rho_p}{\rho_B}$ is the isospin asymmetry. The quantity $\rho_B$ represents the baryon density while neutron and proton densities are given by $\rho_n$ and $\rho_p$ and the saturation density is marked with $\rho_0$. In symmetric nuclear matter (SNM), i.e. $\delta = 0$, only the first term contributes and it can be expanded as

$$E_0(x,0) = -B_0 + \frac{1}{18}Kx^2 + \frac{1}{162}Qx^3 + \dots . \tag{10}$$

excluding the contribution of the nucleon rest masses. The form of the EOS is determined by the binding energy per nucleon at saturation $B_0$ (or $\frac{E}{A}$), the incompressibility or compression modulus $K$, a quantity which is used to characterize the stiffness of the EOS, and the skewness Q. $K$ is a measure for the energy needed to compress the matter and it is given by

$$K = 9\frac{\partial P}{\partial n_B}|_{n_B=n_0} = 9n_B^2\frac{\partial^2(\epsilon/n_B)}{\partial n_B^2}|_{n_B=n_0} \tag{11}$$

where $P(n_B)$ is the pressure. Since pressure vanishes at the saturation point $(P(n_0) = 0)$, the incompressibility is given by the curvature of the energy per nucleon or the slope of the pressure. In early RMF models the values obtained for $K$ were around 540 MeV which is rather large and leads to very stiff, highly repulsive EOS at higher densities. Constraints for the nuclear incompressibility $K$ can be deduced from fitting results of theoretical models to experimental data on the isoscalar giant monopole resonance (ISGMR), the vibration modes of excited nuclei where the nucleus performs collective density fluctuations around its ground state, also called the breathing mode. The corresponding value of $K$ generally

accepted today is $K = 248 \pm 6$ MeV [59] or $K = (240 \pm 20)$ MeV [60]. For asymmetric nuclear matter (ANM) the second term in eq. (9), the symmetry energy, given by

$$E_{sym}(x) = J + \frac{1}{3}Lx + \frac{1}{18}K_{sym}x^2 + \dots \tag{12}$$

is also important. It contains the symmetry energy at saturation $J$, which represents the energy difference between the pure neutron matter and symmetric nuclear matter with an expected value in the range of $32 \pm 2$ MeV [41]. The symmetry energy slope parameter $L$ is given by derivative of the symmetry energy

$$L = 3n_0 \frac{\partial E_{\rm sym}(x)}{\partial n_B} \tag{13}$$

and the symmetry energy curvature $K_{sym}$ by

$$K_{sym} = 9n_0^2 \frac{\partial^2 E_{\rm sym}(x)}{\partial n_B^2}\,. \tag{14}$$

Nuclear matter parameters are in general strongly correlated among each other, as well as to properties of nuclei and NSs [41, 61, 62, 63]. The actual parameters of EOS models can be expressed as functions of these empirical parameters ($B_0$, $n_0$, $K$, $J$, $L$, $K_{sym}\dots$) within RMF models. The coefficients are constrained through model comparison with empirical data. The most important constraints on the nuclear matter parameters and the EOS will be discussed in detail in the subsection 2.3.

The expansion of energy per nucleon is given around the saturation point. Up to this density the modeled EOS is well constrained by experimental data. The value of the saturation density is intuitively easy to understand: a nucleon has a radius of $\sim$ 1.2 fm, which means that it occupies a volume of about 8 fm$^3$. This means that at the density of $1/8$ fm$^{-3}$ nucleons will start to touch. From the van-der-Waal's like behavior of the nuclear forces this configuration is the energetically most favorable one since the contribution from the strong intermediate range attraction is maximal in this case. A further compression of nucleons is strongly hindered due to the repulsive hard core of the potential. For this reason nuclear systems at densities which exceed much the saturation density $\rho_0$ are usually not found in nature. The exception of this case is a NS, which can overcome the repulsive potential due to the very high gravitational pressure enabling further compression of stellar matter up to five to ten times saturation density, as shown by model calculations. The models are in general fitted to nuclear data and then extrapolated to higher densities that are reached in NS interiors. In such models the NS properties depend crucially on the high density behavior of the nuclear EOS. In the following subsection NSs are introduced through a brief history on their discovery, followed by some of the fascinating properties unique to these dense objects and the description of NS EOS properties.

### 2.2.2 Neutron stars

The existance of NSs was first proposed in the early thirties by W. Baade and F. Zwicky [64], only two years after the discovery of the neutron by J. Chadwick [65]. Trying to explain the origin of supernovae, in their own words they state: *"With all reserve we advance the view that a super-nova represents the transition of an ordinary star into a neutron star, consisting mainly of neutrons. Such a star may possess a very small radius and an extremely high density."* For a long time NSs were thought to be too faint to be detectable and there was a little interest in them as more than a hypothetical phenomenon. The topic revived in the late sixties when English graduate student Jocelyn Bell working with radio astronomer Antony Hewish detected the sources of pulsating radio beams [66], now known as the rotating neutron stars with strong magnetic fields, the pulsars. This generated a greater amount of interest and activity in the field which resulted in many other discoveries with more than 2500 pulsars known up to date [67], most of which are radio pulsars. As the most important ones we can point out the discoveries of the first

binary pulsar in 1974 by Joseph Taylor and Russell Hulse [68], the first millisecond pulsar in 1982 by Don Backer et al. [69], the double pulsar system in 2004 by Lyne et al. [70] and recent observations of two pulsars with approximately two solar masses ($\sim 2$ M$_\odot$) by Paul Demorest et al. [71] in 2010 and John Antoniadis et al. [72] in 2013. The latest discoveries of NSs with such high masses presents a severe challenge to the theoretical description of cold high-density matter in $\beta$-equilibrium. The EoS has to be sufficiently stiff in order to support such high masses of compact stars. Many models that are solely based on nucleonic (neutrons and protons) and leptonic (electrons and muons) degrees of freedom are able to reproduce maximum NS masses above 2 M$_\odot$ if the effective interaction between the nucleons becomes strongly repulsive at high baryon densities. However, above $2-3$ $\rho_0$ the possible appearance of hadronic particle species in most cases leads to a substantial softening of the EoS resulting in reduced maximum mass of the compact star below the observed values. This feature is well known for models with hyperons - the so-called "hyperon puzzle", see, e.g., [73, 74] and the references therein - but was also observed in approaches that take excited states of the nucleons such as $\Delta(1232)$ resonances into account, see, e.g., [75, 76] and the references therein.

NSs are formed when the central iron core of massive stars with about $8-20$ $M_\odot$ collapses. Fusion reactions can no longer release energy and the thermal pressure cannot counterbalance gravity. High-energy photons dissociate the iron nuclei and electrons merge with protons to produce neutrons and neutrinos reducing the electron degeneracy pressure. Both processes accelerate the collapse that re-bounces as soon as the compression of the neutron-rich matter is halted by the increasing stiffness of the EOS or an outward traveling shock wave is generated. In the center of the star a hot PNS is left that cools predominantly by emitting a copious number of neutrinos. The resulting NSs are extremely dense, with typical masses of 1 to 2 $M_\odot$ and radii of only of 10 to 20 km. They are hold together by gravity. As a consequence the surface gravity is very high, more than $10^{11}$ times that of the Earth. Except for being the densest objects in Universe besides BHs, NSs are extreme cases in many other properties. NS magnetic fields are known as the highest magnetic fields ever observed with the values of about $10^{11}-10^{13}$ G present in most objects (the bulk of the so-called 'classical pulsars'), while going as low as $10^8-10^9$ G in the old, but rapidly spinning "millisecond pulsars", and as high as $10^{14}-10^{15}$ G in the slowly spinning, but very energetic "soft gamma repeaters" (SGRs) [77] and "anomalous X-ray pulsars" (AXPs), collectively known as 'magnetars' with low rotation periods of $P \sim 2-12$ s. The comparison of NS magnetic field and gravitation strengths to several other objects are given in Tables 3 and 4, respectively. Furthermore, NSs are also the fastest known rotating objects in the universe, spinning up to 716 times a second for the fastest pulsar known today, the PSR J1748-2446ad discovered by Jason W. T. Hessels et al. in 2004 [78].

When we look into the NS structure (figure 4) we find that it changes significantly starting from its surface and going toward its core. A thin layer of "atmosphere" is hypothesized to be at most several micrometers thick, and its dynamics are fully controlled by the NS's magnetic field. Below that we encounter a hard and very smooth solid "crust", with maximum surface irregularities of $\sim 5$ mm, due to

**Table 3:** Comparison of magnetic fields for different objects.

| System | Magnetic field [Gauss] |
|---|---|
| Microwave oven (in use) | $40\cdot10^{-3}-80\cdot10^{-3}$ |
| Earth | $0.25-0.65$ |
| Milisecond pulsars | $10^8-10^9$ |
| "Classical" pulsars | $10^{11}-10^{13}$ |
| Magnetars (SGRs and AXPs) | $10^{14}-10^{15}$ |
| Higest observed magnetic field (SGR 0418+5729) | $2\cdot10^{14}-10^{15}$ |
| Upper limit to neutron star magnetism | $10^{17}$ |

**Table 4:** Comparison of gravity for different objects in the Universe in units of surface gravitational acceleration on Earth, $1g = 9.80665\ m/s^2$.

| System | Surface gravity [g] |
|---|---|
| Moon | 0.1654 |
| Mars | 0.376 |
| Earth | 1 |
| Jupiter | 2.53 |
| Sun | 28.02 |
| White dwarf | $35 \cdot 10^5$ |
| Neutron star | $\sim 2 \cdot 10^{11}$ |

the very strong gravity. At the top of the outer crust nuclei of $^{56}$Fe ions are arranged on a body-centered cubic (bcc) lattice embedded in an almost homogeneous gas of electrons. With increasing depth the ions become more massive and neutron rich. At densities of $\sim 10^{-4}$ fm$^{-3}$ we reach the inner crust with the "neutron drip" layer at which it becomes energetically more favorable for neutrons to float out of the nuclei and move freely around. Going further toward the center of the star, the heavy nuclei merge and form inhomogeneous structures of different geometry, for which the term "nuclear pasta" [80] has been introduced. The nuclear pasta structures evolve with increasing density until they melt, and the transition to uniform matter occurs, as depicted in Fig. 4. The matter is now homogeneous and the core of the NS is reached. At densities more than two to three times the saturation density we are still not sure about the composition of matter, as it was discussed in the introduction. Again, there are different models that describe different layers of the NS structure. The EOS for outer layers is considered to be well known since enough data are available for the low density region from many different measurements. Several models are regularly used, such as Baym-Pethick-Sutherland (BPS) from 1971 [81], Haensel and Pichon [82] (1994) or Ruester, Hempel, Schaffner-Biellich [83] (2006) for the outer crust of a NS, that is for densities below the neutron drip, $\rho < 10^{-4}$ fm$^{-3}$. The inner crust can also have a separate EOS and some of them are e.g. the Baym-Bethe-Pethick (BBP) [84] from 1971, Negele-Vautherin (1973) [85], Douchin & Haensel (2001/2011) [86, 87], Inner crust EOS within a Thomas-Fermi (TF) approximation [88] etc. The generally used construction is often the BPS + BBP + homogeneous matter above $\rho \approx \rho_0/3$ [89].

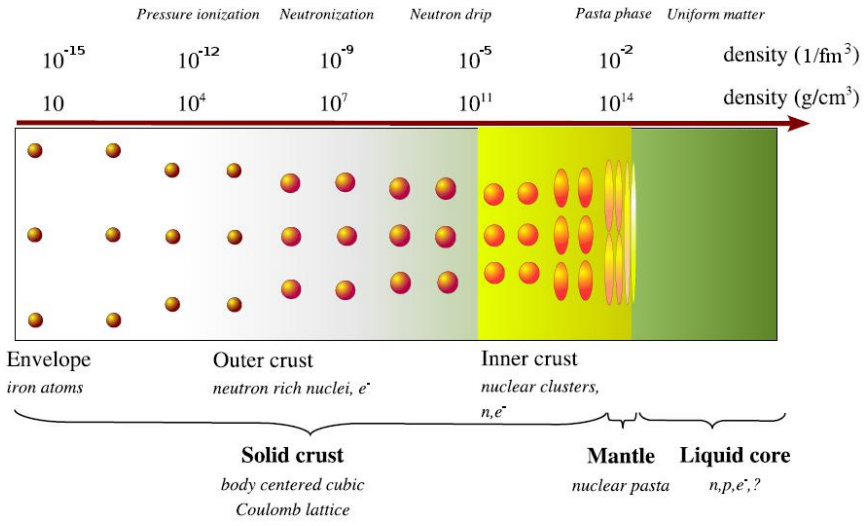


**Figure 4:** The composition of neutron star layers of matter. Modified from [79] by including the densities measured in fm$^{-3}$.

The EOS for NSs is calculated in the same manner as for the infinite nuclear matter, giving the energy density $\epsilon$ or pressure $P$ in dependence of baryon density $n_B$. It is usually presented with the mass-radius relation, which gives the EOS of a NS in terms of its mass and radius, as in Fig. 6 (details explained in the next subsection). When modeling static and spherically symmetric stars in Newtonian mechanics we derive the fundamental equations of hydrostatic equilibrium to connect the mass and radius of the star to its EOS. These equations are working well in cases where general relativity (GR) effects can be neglected, such as for e.g. white dwarfs (WD). Since we are describing NSs where general relativity plays an important role, we need to include the relativistic corrections. Within the work of Tolman, Oppenheimer, and Volkoff [90, 91] the system of differential equations in GR, which has to be solved, is provided for spherically symmetric stars, the so-called TOV equations

$$\frac{dP(r)}{dr} = -\frac{M(r)\epsilon(r)}{r^2}\left[1+4\pi r^3\frac{P(r)}{M(r)}\right]\left[1+\frac{P(r)}{\epsilon(r)}\right]\left[1-2\frac{M(r)}{r}\right]^{-1} \tag{15}$$

$$\frac{dM(r)}{dr} = 4\pi\epsilon r^2 \tag{16}$$

where r is the radius of a NS and $M(r)$ is mass at a certain radius. The EOS relating pressure $P$ to the energy density $\epsilon$ closes the system of equations. Note that we are using natural units, where Newton's gravitational constant G and the speed of light c are equal to one. It is the equation for pressure (15) that differs from the corresponding Newtonian theory equation of hydro-statical equilibrium

$$\frac{dP(r)}{dr} = -\frac{M(r)\epsilon(r)}{r^2} \tag{17}$$

by three additional dimensionless factors, all working in favor of gravity. In the non-relativistic limit, the energy density $\epsilon$ becomes the mass density and the first two factors go to 1. The last factor is a GR correction due to the curvature of space in the strong gravitational field of the star. Whether it is important to take it into account or not is determined by the size of $M/r$. These corrections each act to strengthen the gravitational interaction. The TOV equations are applied for the barotropic EOSs, the ones in which the pressure and energy density are functions of the baryon density alone, as in this work.

Both infinite nuclear matter and NS matter are described with the EOS model that has a certain number of parameters. The parameter values are fitted to different experimental data for nuclei and nuclear matter at saturation density or constrained to a range of possible values by data from different sources. The main data sources used to constraint EOS models parameters are introduced in the next chapter.

## 2.3 Constraining the model parameters

EOS models are constrained by a number of adjustable parameters that have to be determined by data coming from different sources. These are mainly: 1. observations in astronomy, 2. laboratory experiments and 3. theoretical ab-initio calculations. For the high-density region the first two points are the main sources of constraints, as we elaborate in the following. Improved and novel measurements provide stricter constraints on parameter values to be used in many studies, both for nuclear structure and astrophysical applications. It is essential for the further development of the field to determine the most realistic parameter sets and to use them consistently.

### 2.3.1 Astrophysical observations

Astrophysical observations of NSs are important in constraining their EOS and for developing theoretical models of their composition. The energy for electromagnetic radiation from NSs is not produced through nuclear reactions like in normal stars. Isolated NSs are visible because charged particles, like electrons,

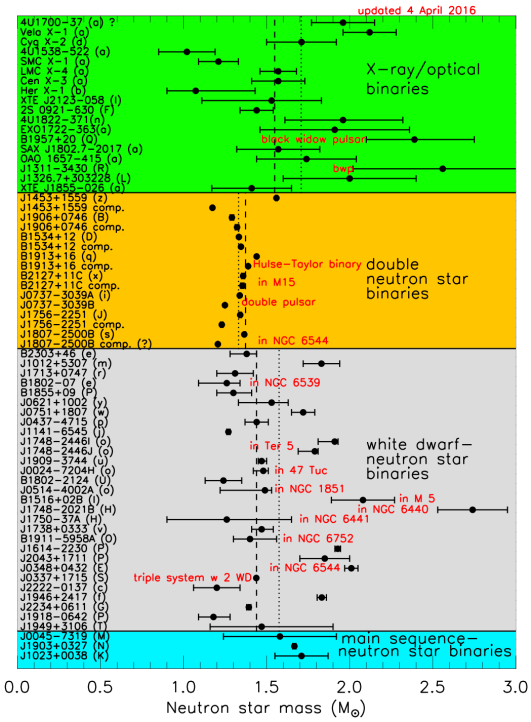


**Figure 5:** Measured NS masses from different binary systems. The figure is the latest update of the original Fig. published in reference [94].

radiate when accelerated by the magnetic field of the star. Radiation is emitted from two opposite regions and if the radiated "beam" passes through our line of sight, we see it as a pulsation, from which their name, pulsars, comes from. Pulsars are mostly observed in radio, but also in other parts of the electromagnetic spectrum: visible light, near infrared, ultraviolet, X-rays and gamma rays. When NSs appear in a binary system, with e.g. a WD or another NS, it is possible to deduce their mass. In recent years two pulsars with approximately two solar masses were observed, both as part of a NS - WD binary, challenging the theoretical description of cold high-density stellar matter. The observations of the binary millisecond pulsar $J1614-2230$ were performed in 2010 with the National Radio Astronomy Observatory Green Bank Telescope (GBT). Through the detection of Shapiro delay (a GR effect) of very high significance, the pulsar mass was measured being equal to $(1.97 \pm 0.04)\ M_\odot$ [71], which was then by far the highest precisely measured NS mass. Few years later the radio-timing observation of the pulsar $J0348+0432$ reveals its mass to be $(2.01 \pm 0.04)\ M_\odot$, as reported in [72]. This was, and still is, only the second NS with a precisely determined mass around $2\ M_\odot$. To make it more challenging, there are indications of even more massive NSs, e.g. in black widow and redback systems ([92, 93]), indicated also in the latest update of figure 5 from J. Lattimer [94]. In this cases, the pulsar is accompanied by a low mass companion of a few $0.01\ M_\odot$ (black widows) or near $0.2\ M_\odot$ (redbacks), which is bloated and strongly irradiated by the pulsar. However, we have to keep in mind that the analysis of these systems is much more model dependent than the NS-WD systems. By using different methods of mass measurement for NSs in binary system, a verification of the NS maximum mass constraint on the EOS of superdense matter is provided.

As we explained already, the EOS for a NS is usually presented in a mass-radius diagram as the one shown in figure 6, where the NS mass is given in solar masses ($M_\odot$) while the radius is in km. In order to satisfy the NS maximum mass constraint, the EOS models have to be able to reproduce the value of $2\ M_\odot$. Only with this constant, many of existing EOSs can already be ruled out. Usually, models that are based on nucleonic (neutrons and protons) and leptonic (electrons and muons) degrees of freedom are able to reach this maximum mass if the effective interaction between nucleons becomes strongly repulsive at high baryon densities. Some of the existing models are shown as black curves on figure 6.

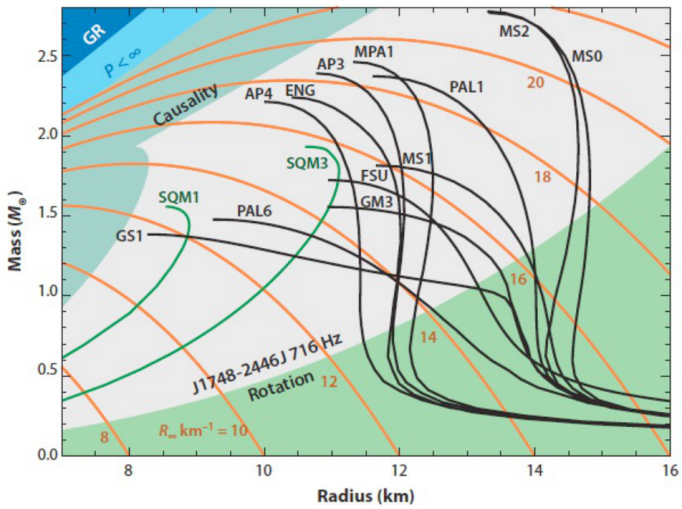


**Figure 6:** Neutron star mass-radius diagram including the constraints on the EOS. Hadronic EOSs are given in black full lines while the strange matter ones are presented in green. Taken from [4] (original version in [40]).

The appearance of the additional degrees of freedom at higher densities would lead to a drastic softening of the EoS, which shifts the maximum possible NS mass below the observed values. This feature is known for models including hyperons as "hyperon puzzle" [73, 95] but it also appears in approaches that take into account excited states of nucleons such as $\Delta(1232)$ resonances [96, 97]. The same is the case for the possible self-bound quark stars whose mass-radius relation is given as green lines on the figure 6. In the phenomenological modeling of EOS with hyperons so far only specifically designed interactions can avoid the problem of too low maximum masses. The additional excluded regions of the NS mass-radius diagram are the dark blue region of figure 6, excluded by the GR constraint $R > 2GM/c^2$, the light blue region excluded by the finite pressure constraint $R > 9GM/4c^2$ and the green region excluded by causality, $R < 2.824GM/c^2$. The light green region marked with "rotation" is bounded by the realistic mass-shedding limit for the highest known pulsar frequency, 716 Hz, for PSR J1748-2446J [98]. Orange curves are contours of constant radiation radius, $R_\infty = R/\sqrt{1-2GM/Rc^2}$.

Except for the maximum mass condition, the determination of mass and radius of the same object would be the ultimate constraint on the EOS, as discussed in [99, 100, 101, 102]. As we have seen, the masses of particular NSs can already be measured quite precisely. The radius observations are, however, much more model dependent since the measurements are more indirect. There are different possible sources of systematic error and depending on the type of object observed different uncertainties are of importance in determining the radius. At the moment, the radius determinations do not have strict constraints as the mass measurements. However, many efforts are put in observations with the goal to measure NSs radii. Future projects such as NICER (The Neutron star Interior Composition ExploreR) [103], ATHENA+ (Advanced Telescope for High Energy Astrophysics) [104] and LOFT (The Large Observatory for X-ray Timing) [105] as well as the expected detection of gravitational waves from NS mergers at LIGO (Laser Interferometer Gravitational-Wave Observatory) [106] will help to significantly constrain radii, and by that the EOS, of NS matter.

### 2.3.2 Laboratory experiments

Further constraints on EOS models come from a variety of laboratory experiments. Different measurements provide information about the nuclear symmetry energy that is usually encoded in the $J$ (marked as $S_v$ in Fig. 7) and $L$ parameters. At the present time, it is not possible to determine their exact values. Instead, we obtain a correlation between them which is specific for each type of measurement. By combining different experiments and studying different correlations it is possible to restrict ranges of the

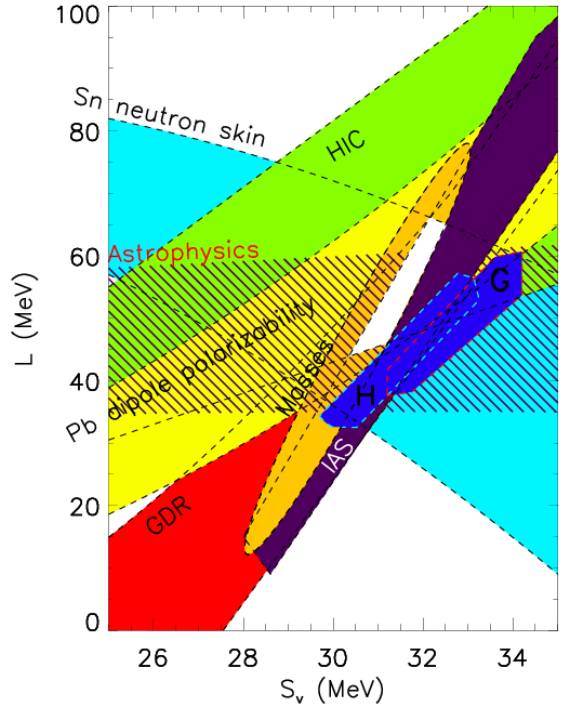


**Figure 7:** Experimental constraints for symmetry energy parameters, taken from [63], adapted and revised from [41]. The enclosed white area is the experimentally allowed overlap region. See text for details.

parameters values. This was explored in the work of Lattimer and Steiner [63] and the updated results are given in figure 7, where the parameter's ranges are plotted regarding different experiments.

1. *$L-J$ correlation from different experiments*
   The most basic constraints on EOS comes from the properties of nuclei, that is their masses and density distributions. The nuclear matter parameters are obtained after the extrapolation to infinite mass number is performed. The obtained constraints are the saturation density $\rho_0$, ground state binding energy $B_0$ and the correlation between the symmetry energy at saturation $J$ and the slope parameter $L$, as given in figure 7, with the region indicated with "Masses". The correlation of the same values is calculated for the excitation energies to isobaric analog states (IAS), tightening the constraint on possible values of the two parameters. Further experiments include the nuclear resonances like the already mentioned ISGMR that constrains the incompressibility $K$ or the nuclear isovector giant dipole resonance (IVGDR) that is used to constraint the symmetry energy. The $L-J$ correlation can also be obtained for the electric dipole polarizability $\alpha_D$ extracted from the electric dipole response of $^{208}$Pb from proton inelastic scattering and through the neutron skin thickness measurements. It is possible to get a correlation also from HIC experiments and astrophysical calculations, all indicated in figure 7. Plotting these parameter ranges from different sources on the same graph reveals the enclosed overlap region (in white) that narrows down the possible values for the $J$ and $L$ parameters significantly.

2. *Optical potential*
   Besides the above mentioned experiments, elastic nucleon-nucleon scattering is in general a powerful tool to investigate nuclear structure. While electron scattering is sensitive only to charge distributions, proton scattering allows to study both proton and neutron distributions at interme-

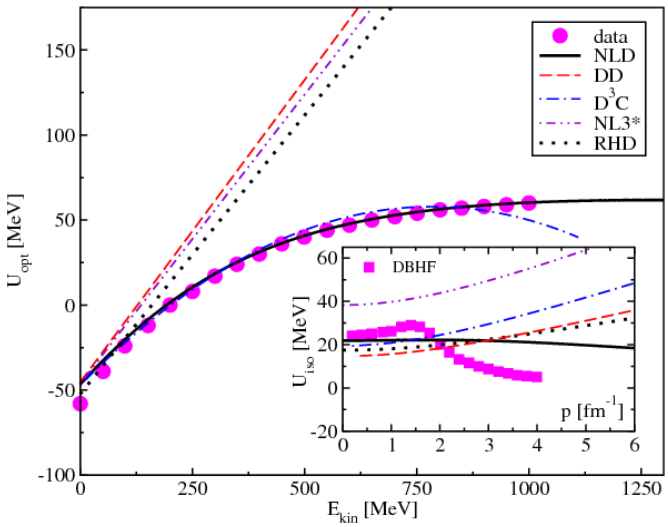


**Figure 8:** Energy (momentum) dependence of the real part of the optical (Lane) potential in the main (inserted) panel. Taken from [109].

diate energies up to 1 GeV. It provides a detailed information on nuclear density distributions that can be compared to different theoretical predictions. Through the measurements of elastic proton scattering on nuclei with different mass number $A$ [107, 108] the behavior of the nucleon optical potential with increasing kinetic energy and in the limit $A \rightarrow \infty$ was obtained. The optical potential $U_{\text{opt}}$ characterizes the in-medium interaction of a nucleon, representing what a proton "feels" when it travels through nuclear matter. It can be calculated from a nonrelativistic reduction of the Dirac equation or the difference of the nucleon energy in the medium and the kinetic energy of a free nucleon without interaction at the same momentum $\overrightarrow{p}$. The real part of the optical potential enters the momentum dependent mean-field dynamics of a nucleon in nuclear matter. The imaginary part is beyond the scope of this work. The main panel of figure 8 taken from paper [109] shows that the commonly used RMF models (e.g. RHD, NL3*, DD, depicted by lines) described later in chapter 3.3 do not reproduce the (real) optical potential behavior consistent with the empirical data. They show a linear dependence of $U_{\text{opt}}$ with energy while the data clearly show a saturation as we approach 1 GeV. The data (pink circles) are extracted from Dirac phenomenology for the in-medium proton optical potential in symmetric nuclear matter at saturation density. In order to reproduce the experimental behavior, an additional energy dependence of $U_{\text{opt}}$ has to be implemented and some of the models, like NLD [109] and D$^3$C [110] given in the same figure include this feature. The new approach of this work introduces an additional energy dependence by including higher order derivatives in the meson-nucleon couplings. This will be explained in detail in chapter 4. The aim is to obtain a very general, flexible model capable of describing both nuclear matter and finite nuclei while satisfying the $U_{\text{opt}}$ constraint.

3. *Heavy-ion collisions*

Studying nuclear collisions also plays an important role in constraining the EOS for high density matter. For short times superdense matter can be created on Earth by means of relativistic heavy-ion collisions. During these collisions, the achieved pressures strongly influence the motion of ejected matter and provide the sensitivity to the EOS needed for its determination. The observables sensitive to the EOS are primarily related to the flow of particles from the high-density region in direction perpendicular to the beam axis. Initially this flow is zero but it grows with time, increasing density and development of pressure gradients in directions transverse to the beam axis. In the work of Danielewicz, Lacey and Lynch [111] the experimental observables associated with the motion of ejected matter in simulations of Au + Au collisions were studied and the range

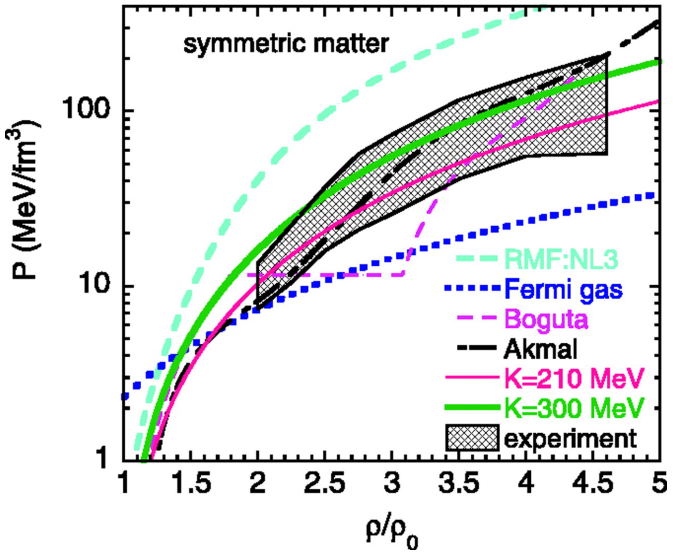


**Figure 9:** Zero-temperature EOS for symmetric nuclear matter. The shaded region correspond to the pressure and experimental flow data consistency region. Taken from [111].

for the allowed pressure-density relationship was assessed (Fig. 9). With this a constraint on the symmetric nuclear matter EOS is obtained, that rule out very repulsive EOSs from some RMF models and very soft EOSs with a strong phase transition at densities lower then $3n_0$. The softening of the EOS at higher densities due to the transformation to quark matter is not excluded.

### 2.3.3 Theoretical *ab-initio* calculations

For completeness, let us shortly address the constraints coming from theoretical calculations that include *ab-initio* interactions. In case of general asymmetric nuclear matter (ANM) the interaction Hamiltonian can be quite complicated after including two- and three- body interactions between particles. A simplification of the interaction is achieved because of the isospin structure of pure neutron matter that suppresses certain contributions. Many models already mentioned in section 2.1 are used for these calculations (see figure 10). Details can be found in [42] and references therein.

The conclusion of ab-initio calculations is that different models are in reasonable agreement with each other up to the saturation density which shows that the many-body calculations with realistic interactions

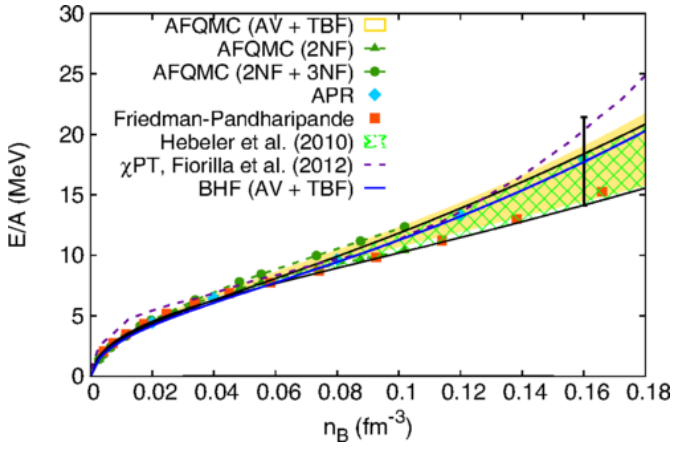


**Figure 10:** Comparison of results for the energy per baryon of neutron matter at T = 0 from different ab initio approaches. Taken from [42].

give a reliable constraint on the EoS of neutron matter up to nuclear densities. For the calculations of SNM the theoretical many-body calculations are not as reliable as for neutron matter and at present can not serve as a strong constraint on the EOS.

# 3 Standard RMF models

In this chapter we will go through the main steps needed to develop a consistent RMF model. The idea is, in a first step, to build a Lagrangian density containing all the interaction terms of nucleons and mesons. This will depend on the choice of the interaction and is model dependent. Second, by an application of the least action principle, one gets a set of equations of motion. The nucleons obey the Dirac equation, while the mesons obey the Klein-Gordon equation. Through an iterative procedure and fitting of parameters regarding the selected constraints, we eventually obtain the needed meson fields, couplings and densities. From the continuity equations of the conserved current and the energy-momentum tensor the energy density and pressure are obtained. Their dependence on the baryon density gives the EOS of nuclear matter.

## 3.1 Nuclear interaction

In most of the relativistic-mean field models the system is composed of nucleons that interact via the exchange of photons and virtual mesons while neglecting their substructure. Therefore, they define the degrees of freedom of the studied system. The types of the meson fields are assigned according to their quantum properties which are spin ($J$), isospin ($T$) and parity ($\Pi$). In the interactions, the mesons are classified as scalar ($J = 0$) or vector ($J = 1$), isoscalar ($T = 0$) or isovector ($T = 1$) mesons. The possibly exchanged mesons and their propertie are given in the table 5.

The first model of this kind took into account only $\sigma$ and $\omega$ mesons and is known as $\sigma\omega$- or Walecka model, due to J. D. Walecka who developed the first version of Quantum Hadron Dynamics (QHD) in 1974 [53]. However, the original idea of an effective scalar and vector exchange goes back to H. P. Dürr in 1956 [112]. It was born in the attempt to formulate a renormalizable meson theory of the strong interactions. Today it is considered as an effective theory applied only at the mean field level. It is effective in the sense that the coupling constants of mesons with nucleons are treated as free parameters adjusted to the properties of nuclear matter (mostly at the nuclear saturation point) and finite nuclei, instead of being determined from free nucleon-nucleon scattering. This makes the Walecka model to have the simplest form of a relativistic density functional for the nuclear EOS. The $\sigma$ and $\omega$ mesons are introduced to consider the attractive and repulsive contributions of the nucleon-nucleon potential and are represented by isoscalar Lorentz scalar and Lorentz vector fields $\sigma$ and $\omega_\mu$. Since we are aiming for a model that describes both asymmetric nuclear matter and finite nuclei, we will include the charged $\rho$ meson triplet ($\rho^0, \rho^\pm$) in order to model the isospin dependence of the interaction. It does not contribute in infinite symmetric nuclear matter but it is important once the isospin asymmetry is introduced, as well as for an accurate description of finite nuclei properties (binding energies, neutron skins etc.). It will be denoted by the isovector Lorentz vector field $\overrightarrow{\rho}_\mu$ in the following text. The isovector Lorentz scalar $\delta$ meson contributes to a slight difference in the scalar nuclear potential for protons and neutrons affecting their effective masses. For simplicity, we omit it. The pion is a pseudoscalar ($J^\Pi = 0^-$) and isovector ($T = 1$) meson. Because of these characteristics, the pion field does not contribute even if we include it, since we assume the parity symmetry of a nuclear mean field as it is usually done in many mean-field models. The Lagrangian will be invariant under parity transformation and, since we only consider solutions with well-defined parity, the expectation value of the pseudoscalar pion field vanishes in the

**Table 5:** Potential candidates for the meson degrees of freedom.

| Meson | $(J^\Pi, T)$ | Field | interaction |
|---|---|---|---|
| $\sigma$ | $(0^+, 0)$ | scalar-isoscalar | middlerange attraction |
| $\omega$ | $(1^-, 0)$ | vector-isoscalar | shortrange repulsion |
| $\rho$ | $(1^-, 1)$ | vector-isovector | isospin part of nuclear force |
| $\delta$ | $(0^+, 1)$ | scalar-isovector | isospin part of nuclear force |

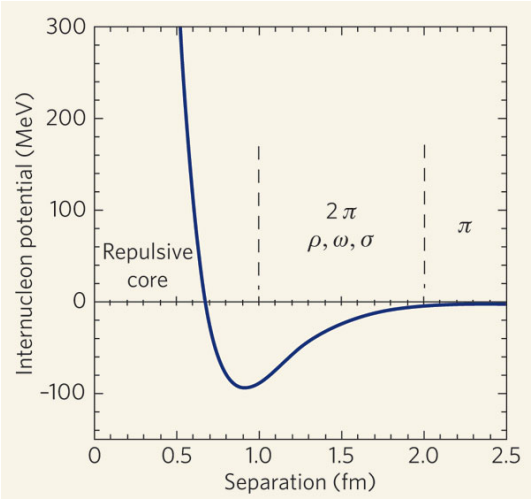


**Figure 11:** The nucleon-nucleon potential for the strong force. At distances of a few fm, the force between two nucleons is weakly attractive, indicated by a negative potential. According to Yukawa's model, this force is mediated by the exchange of particles known as mesons. The $\pi$-meson, or pion, the lightest of the mesons, accounts for the attractive force at the largest distances where it is felt, whereas heavier mesons ($\rho$, $\omega$, $\sigma$) take over closer in. Below a separation of just under 1 fm the picture changes abruptly since the force becomes strongly repulsive, preventing nucleons merging. Taken from [113]

Hartree approximation. This is the reason why we do not treat the pion in RMF theory and it justifies it's exclusion, even though the pion field is responsible for the long-range nuclear interactions ($r > 2fm$) as indicated in figure 11. Therefore, we consider the simple model containing the $(\sigma, \omega, \rho)$ mesons.

## 3.2 Lagrange density and field equations

The Lagrangian density in the standard RMF approach[2]

$$\mathscr{L} = \mathscr{L}_{\text{nuc}} + \mathscr{L}_{\text{mes}} + \mathscr{L}_{\text{int}} \tag{18}$$

contains three main contributions. The first is the one of free nucleons $\Psi = (\Psi_p, \Psi_n)$, $\overline{\Psi} = \Psi^\dagger \gamma^0$ with mass $m$

$$\mathscr{L}_{\text{nuc}} = \frac{1}{2}\left(\overline{\Psi}\gamma_\mu i\overrightarrow{\partial^\mu}\Psi - \overline{\Psi} i\overleftarrow{\partial^\mu}\gamma_\mu\Psi\right) - m\overline{\Psi}\Psi \tag{19}$$

in a symmetrized form where the arrows in the above equation denote the direction of differentiation. The second term describes the free mesons and photons

$$\begin{aligned}\mathscr{L}_{\text{mes}} &= \frac{1}{2}\Big(\partial_\mu\sigma\partial^\mu\sigma - m_\sigma^2\sigma^2 - \frac{1}{2}F^{(\omega)}_{\mu\nu}F^{(\omega)\mu\nu} + m_\omega^2\omega_\mu\omega^\mu \\ &\quad -\frac{1}{2}\overrightarrow{F}^{(\rho)}_{\mu\nu}\cdot\overrightarrow{F}^{(\rho)\mu\nu} + m_\rho^2\overrightarrow{\rho}_\mu\cdot\overrightarrow{\rho}^\mu - \frac{1}{2}F^{(\gamma)}_{\mu\nu}F^{(\gamma)\mu\nu}\Big)\end{aligned} \tag{20}$$

where the masses $m_\sigma$ , $m_\omega$, and $m_\rho$ are those of the $\sigma$, $\omega$ and $\rho$ mesons fields. The field tensors of the isoscalar $\omega$ meson, the isovector $\rho$ meson and of the photon field $A_\mu$ are given by

$$\begin{aligned}F^{(\omega)}_{\mu\nu} &= \partial_\mu\omega_\nu - \partial_\nu\omega_\mu \\ \overrightarrow{F}^{(\rho)}_{\mu\nu} &= \partial_\mu\overrightarrow{\rho}_\nu - \partial_\nu\overrightarrow{\rho}_\mu \\ F^{(\gamma)}_{\mu\nu} &= \partial_\mu A_\nu - \partial_\nu A_\mu\,,\end{aligned} \tag{21}$$

[2] Natural units with $\hbar = c = 1$ are used in the following.

respectively. The last term in eg. (18) is the interaction term that assumes a minimal coupling of the nucleons to the meson fields and leads to

$$\mathscr{L}_{\text{int}} = \Gamma_\sigma \sigma \overline{\Psi}\Psi - \Gamma_\omega \omega_\mu \overline{\Psi}\gamma^\mu\Psi - \Gamma_\rho \overrightarrow{\rho}_\mu \overline{\Psi} \cdot \overrightarrow{\tau}\gamma^\mu\Psi - \Gamma_\gamma \overline{\Psi}\gamma^\mu \frac{1+\tau_3}{2} A_\mu \Psi \tag{22}$$

where $\overrightarrow{\tau}$ is the isospin operator. The meson-nucleon coupling constants $\Gamma_i$ $(i = \sigma, \omega, \rho)$ and meson masses $m_i$ are parameters, adjusted to reproduce nuclear matter properties at the saturation density and ground-state properties of finite nuclei, while $A_\mu$ stands for the photon field with coupling $\Gamma_\gamma$. The field equations result from the Euler Lagrange equation

$$\frac{\partial \mathscr{L}}{\partial \varphi} - \frac{\partial}{\partial x_\mu} \frac{\partial \mathscr{L}}{\partial \left(\partial \varphi / \partial x_\mu\right)} = 0 \tag{23}$$

where $\varphi$ can be substituted by nucleons $\Psi, \overline{\Psi}$ or mesons $\sigma, \omega_\mu, \overrightarrow{\rho}_\mu$. In case of nucleons we obtain the Dirac equation

$$\left[\gamma_\mu \left( i\partial^\mu - \Gamma_\omega \omega^\mu - \Gamma_\rho \overrightarrow{\tau}\overrightarrow{\rho}^\mu - \Gamma_\gamma \frac{1+\tau_3}{2} A^\mu \right) - (m - \Gamma_\sigma \sigma)\right]\Psi = 0 \tag{24}$$

in which vector field appears with the derivative while the scalar field goes into the mass term. The field equations for mesons and the photon with the source-terms on the right-hand side are given by

$$\begin{aligned}
\left(\partial_\mu \partial^\mu + m_\sigma^2\right)\sigma &= \Gamma_\sigma \overline{\Psi}\Psi \\
\partial_\mu F^{(\omega)\mu\nu} + m_\omega^2 \omega^\nu &= \Gamma_\omega \overline{\Psi}\gamma^\nu\Psi \\
\partial_\mu \overrightarrow{F}^{(\rho)\mu\nu} + m_\rho^2 \overrightarrow{\rho}^\nu &= \Gamma_\rho \overline{\Psi}\gamma^\nu \overrightarrow{\tau}\Psi \\
\partial_\mu F^{(\gamma)\mu\nu} &= \Gamma_\gamma \overline{\Psi}\gamma^\mu \frac{1+\tau_3}{2}\Psi\,.
\end{aligned} \tag{25}$$

Source terms are proportional to the corresponding densities (which will be denoted with $n$ in the following, since $\rho$ is used for the vector-isovector meson), where

$$\hat{n}_S = \overline{\Psi}\Psi \tag{26}$$

is the scalar density operator and

$$\hat{j}_\mu = \overline{\Psi}\gamma_\mu\Psi = \left(\hat{n}_B, \hat{\overrightarrow{j}}\right) \tag{27}$$

represents the four-vector baryon current operator where $\hat{n}_B$ is the baryon density and $\hat{\overrightarrow{j}}$ represents vector current. One novel and essential feature of the relativistic description is the distinction between the scalar density $n_S$ and the baryon density $n_B$, the time-like component of the four-current (27), which will have strong consequences for the entire dynamics.

## 3.3 RMF model extensions

The simplest RMF model with constant baryon-meson couplings and linear Proca and Klein-Gordon equations for the meson fields (such in Walecka's $\sigma\omega$ model) is not sufficient to provide a quantitative agreement between theory and experiment for nuclear matter and finite nuclei. Properties of nuclear matter are not satisfactory (too large incompressibility and too small effective mass) and finite nuclei are not described well. Extensions of this simple model were needed. Three typical examples of such extended models that are widely used today are the following:

- **Non-linear (NL) models**, proposed by Boguta et al. [114]. In order to lower the incompressibility of nuclear matter additional non-linear self-interactions of meson fields are introduced. In this way the size and density dependence of the effective mass can be tuned and successful models for finite nuclei have been constructed.

- **Density dependent (DD) coupling models** [115] are an alternative approach suggested by relativistic DBHF theory of nuclear matter where the scalar and vector coupling functions in the Lagrangian density are replaced by density dependent vertex functions.

$$\Gamma_\sigma \to \Gamma_\sigma(n_v) \qquad \Gamma_\omega \to \Gamma_\omega(n_v) \qquad \Gamma_\rho \to \Gamma_\rho(n_v) \tag{28}$$

  where $n_v = \sqrt{J^\mu_v J_{v,\mu}}$ is the vector density and $J^\mu_v = \sum_{i=p,n} \langle \overline{\Psi}_i \gamma_\mu \Psi_i \rangle$ is the conserved baryon current. In this way the higher order effects are efficiently introduced into Lagrangian.

- **Relativistic point-coupling models** are another approach where the meson exchange picture is abandoned and the Lagrangian, which is exclusively formulated in terms of nucleon fields and point-like couplings, is systematically expanded in powers of nucleon fields and vertices. The vertices are constructed by contractions of the Dirac structures (scalar, vector, tensor, ...) and derivatives. Instead of the mesons, the derivatives now mimic the finite range of the forces.

In principle, the nucleon-nucleon interaction is controlled by the underlying effective Lagrangian. The ad-hoc density dependence or non-linear couplings simulate many-body effects. These extensions provide a quite successful description of finite nuclei properties and are widely used in today's models. Naturally the occurrence of additional parameters arises which allows a better reproduction of the saturation point. The DD and NL extensions, that keep the meson exchange picture, are both tuned to finite nuclei which is why they both give similar EOSs for moderate densities (in the region $0 \leq n \leq n_0$) where the model parameters are constrained by the data. By extrapolation to supra-normal densities strong deviations within phenomenological models occur and the predictive power of these models becomes limited. Here we can not rely on approaches that fit parameters only to the nuclear bulk properties. A comparison of these NL and DD models for neutron and nuclear matter is given in Fig. 12. In addition we see the results from the QHD-I model that represents the original $\sigma\omega$-model. It gives a quite unrealistic EOS, which is why the extensions are needed in the first place. The microscopic DBHF calculation of infinite matter, which is based on realistic nucleon-nucleon potentials, is also plotted (here obtained with the Bonn-A OBE potential) for comparison.

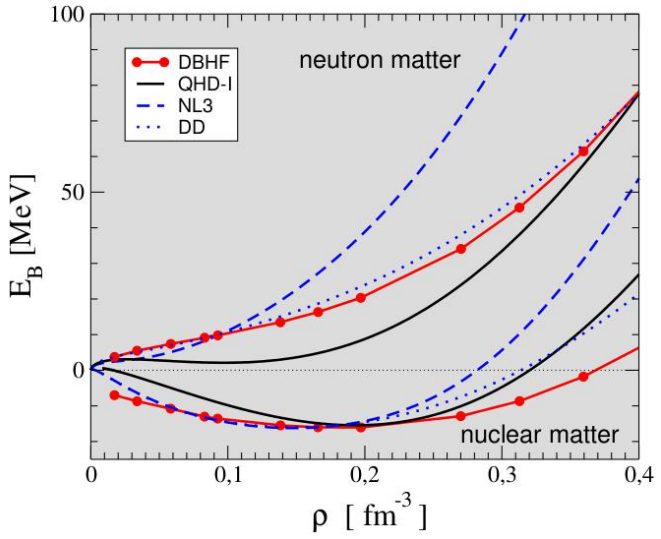


**Figure 12:** Equations of state for symmetric and pure neutron matter for different models. Taken from [116].

## 3.4 Density-dependent (DD) meson-nucleon couplings

The introduction of a density-dependence in the couplings was suggested by the microscopic DBHF theory of nuclear matter. In this theory there is a connection between a bare nucleon-nucleon interaction, given by one-boson exchange potentials, and the effective in-medium interaction that depends on density and momentum. Below the Fermi surface the momentum dependence is weak, so there is no big difference in models if we neglected it. However, at a few-times saturation density the strong influence of the momentum or energy dependence is obvious, as it will be discussed in the next chapter. As a first step, let us introduce the density dependence of the couplings as in Ref. [117].

The density dependence of the couplings has to be formulated as a Lorentz-scalar functional of the baryon fields in order to obtain a Lorentz-covariant Lagrangian and covariant field equations from the Euler-Lagrange equations. The Lagrangian interaction density has the same form as in standard RMF eq. (22), with couplings $\Gamma_i$ $(i = \sigma, \omega, \rho)$ that are no longer constant but density dependent. The scalar and vector meson field contributions in the Dirac equation (24)

$$\left[\gamma_\mu (i\partial^\mu - \Sigma^\mu) - (m - \Sigma)\right]\Psi = 0 \tag{29}$$

are incorporated in the the scalar and vector self-energies, where

$$\Sigma = \Gamma_\sigma \sigma \tag{30}$$

is a scalar, and

$$\Sigma^\mu = \Gamma_\omega \omega^\mu + \Gamma_\rho \overrightarrow{\tau} \cdot \overrightarrow{\rho}^\mu + \Gamma_\gamma \frac{1+\tau_3}{2} A^\mu + \Sigma_R^\mu \tag{31}$$

is a vector self-energy. With this, an additional term $\Sigma_R^\mu$ appears in the vector self-energy, the so-called "rearrangement" contribution if the couplings depend on the vector density $n_v$. It has the form

$$\Sigma_R^\mu = \frac{j^\mu}{n_v}\left[\Gamma'_\omega \omega^\nu \overline{\Psi}\gamma_\nu \Psi + \Gamma'_\rho \overrightarrow{\rho}^\nu \overline{\Psi}\gamma^\nu \overrightarrow{\tau}\Psi - \Gamma'_\sigma \sigma \overline{\Psi}\Psi\right] \tag{32}$$

containing derivatives

$$\Gamma'_i = \frac{\partial \Gamma_i}{\partial n_v} \tag{33}$$

of the coupling functions for different mesons $(i = \sigma, \omega, \rho)$ . This term is necessary in order to preserve the energy-momentum conservation and the thermodynamic consistency of the model. The form of the density-dependence is determined by an optimal fit to nuclear matter properties and selected nuclei data.

The field equations are solved in the mean-field approximation for stationary systems where the photon field and meson fields are treated as classical fields, that is, the meson field operators and the electromagnetic field operator are replaced by their expectation values

$$\sigma \rightarrow \langle\sigma\rangle = \sigma \tag{34}$$
$$\omega_\mu \rightarrow \langle\omega_\mu\rangle = \omega_0 \delta^0_\mu \tag{35}$$
$$\overrightarrow{\rho}_\mu \rightarrow \langle\overrightarrow{\rho}_\mu\rangle = \overrightarrow{\rho_0}\delta^0_\mu \tag{36}$$
$$A_\mu \rightarrow \langle A_\mu\rangle = A_0 \delta^0_\mu \tag{37}$$

where $\sigma$ is the expectation value of the scalar meson field operator, $\omega_0$ and $\rho_0$ are the expectation values of the time-like components of $\omega$ meson and neutral $\rho$ meson field operators, respectively, and $A_0$ denotes the scalar potential of the electromagnetic field in the nuclear system. Because of the long-range Coulomb repulsive interaction between protons, nuclear matter would not be bound and the

electromagnetic interaction is ignored. In finite nuclei however, it should be considered in the structure calculation.

Since in the Hartree approximation we consider stationary problems and we assume time-reversal symmetry, we will have only the zero-components of the currents and vector fields remaining. For the isovector field, because of charge conservation, only the third component does not vanish. Our field equations for mesons keep the form of a standard RMF (25) while looking only to the zero components of currents and vector fields. We are using the abbreviations $\omega = \omega_0$ and $\rho = \rho_0$ and will obtain the meson fields directly from the meson-field equations in nuclear matter

$$\begin{aligned}
\partial_\mu \partial^\mu \sigma + m_\sigma^2 \sigma &= \Gamma_\sigma n_S = \Gamma_\sigma \sum_{i=p,n} \langle \overline{\Psi}_i \Psi_i \rangle \\
\partial_\mu \partial^\mu \omega + m_\omega^2 \omega &= \Gamma_\omega n_B = \Gamma_\omega \sum_{i=p,n} \langle \overline{\Psi}_i \gamma^0 \Psi_i \rangle \qquad (38) \\
\partial_\mu \partial^\mu \overrightarrow{\rho} + m_\rho^2 \overrightarrow{\rho} &= \Gamma_\rho n_I = \Gamma_\rho \sum_{i=p,n} \langle \overline{\Psi}_i \gamma^0 \tau_3 \Psi_i \rangle \qquad (39) \\
\partial_\mu \partial^\mu A_0 &= e\, n_p = \Gamma_\gamma \sum_{i=p,n} \langle \overline{\Psi}_i \gamma^0 \frac{1+\tau_3}{2} \Psi_i \rangle
\end{aligned}$$

where $\langle \ldots \rangle$ denotes the summation over all occupied states. This will give source terms on the right side of field equations proportional to scalar density $n_S = n_p^S + n_n^S$ for the scalar field, to the baryon density $n_B = n_p^V + n_n^V$ for the vector field and to the isospin density $n_I = n_p^V - n_n^V$ for isospin field, where $n_i^S$ and $n_i^V$ stand for scalar and vector density for protons and neutrons ($i = p, n$), respectively.

## 3.5 Beyond the DD coupling model

In order to satisfy the optical potential constraint the real part of optical potential at high kinetic energies has to saturate as it is presented by the data in Fig. 8. To achieve that, the existing DD model has to be further modified by introducing a momentum or energy dependence of the self-energies in addition to the density dependent meson-nucleon couplings. In this way, the linear behaviour of the real part of the optical potential can be modified and fitted to reproduce the saturation at high energies. In general, one would expect that the nucleon self-energies depend explicitly on the particle momentum or energy as, e.g., in Dirac-Brueckner calculations of nuclear matter [118] or in simulations of heavy-ion collisions [119], which is not the case in standard RMF models.

There are various methods to derive the optical potential from the Dirac equation. We are obtaining it from the difference of the in-medium dispersion relation

$$p_i^{*\mu} p_{i\mu}^* = \left(m_i^*\right)^2 , \qquad (40)$$

that contains effective momenta

$$p_i^{*\mu} = p_i^\mu - \Sigma_i^\mu \qquad (41)$$

and the effective masses

$$m_i^* = m_i - \Sigma_i \qquad (42)$$

to the one in free space, $p_i^\mu p_{i\mu} = m_i^2$, where $i = n, p$ stands for neutrons and protons. For infinite nuclear matter where there is no preference for a particular direction, the spatial conponents vanish and we are left with the dependence on the zero component of the four-momenutm ($\mu = 0$), that is the energy.

With simple algebra (see Appendix A for details) the difference of the two is expressed in terms of optical potential

$$U_{\mathrm{i,opt}} = E_i - \sqrt{(E_i - \Sigma_i^\mu)^2 + \Sigma_i \left(2m_i - \Sigma_i\right)} \qquad (43)$$

whose behaviour with energy $E_i$ we addressed as one of the important constraints on the EOS stiffness. The optical potential defined in this way is a general relativistic definition and it always leads to a constant $U_{\rm opt}$ value for large nucleon momenta for energy independent self-energies.

With the introduction of scalar and vector potentials, $S_i = \Sigma_i$ and $V_i = \Sigma_i^0$ as in references [109, 110, 120, 121, 122], the alternative expression

$$U_{\rm i,opt}(E_i) = \frac{E_i}{m_i} V_i - S_i + \frac{S_i^2 - V_i^2}{2m_i} \tag{44}$$

is derived in non-relativistic reduction of the Dirac equation. The linear dependence of $U_{\rm i,opt}$ on the energy is obvious in the first term of the expression (44). With the introduction of an energy dependence in potentials $S_i(E_i)$ and $V_i(E_i)$, $U_{\rm i,opt}$ can be fitted to reproduce the saturation when approaching energies of 1 GeV, as shown in figure 8. $U_{\rm opt}$ is also called Schrödinger-equivalent optical potential since it is exactly the potential which occurs when the non-relativistic Schrödinger equation is derived from the in-medium Dirac equation.

Particular models that contain explicit energy or momentum dependent nucleon self-energies have already been developed. This dependence can not be introduced in a relativistic model in a simple parametric form because it affects, e.g., the definition of the conserved currents. One of the earliest RMF models with scalar derivative couplings was presented by Zimanyi and Moszkowski [123]. A rescaling of the nucleon fields removed the explicit momentum dependence of the self-energies but lead to a considerable softening of the EoS. More general couplings of the mesons to linear derivatives of the nucleon fields were considered by Typel, von Chossy and Wolter [120] with an application to uniform nuclear matter. With appropriately chosen coupling constants a reduction of the optical potential was found as compared to the strong linear energy dependence in conventional RMF models. The model was further extended in [110] assuming a density dependence of the couplings. Named D$^3$C model, it was successfully applied to the description of finite nuclei. Notable new features were the increase of the effective nucleon masses (usually rather small in order to explain the strong spin-orbit interaction in nuclei) and correspondingly higher level densities close to the Fermi energy in nuclei in better concordance with expectations from experiments. However, using couplings only linear in the derivatives leads to a quadratic dependence of the optical potential on the kinetic energy with a decrease for energies exceeding 1 GeV, which is also visible in figure 8. Couplings to all orders in the derivative of the nucleons were introduced in the so-called nonlinear derivative (NLD) model by Gaitanos and Kaskulov [121, 122] assuming a particular exponential dependence on the derivatives but no density dependence of the nucleon-meson couplings or self-couplings of the mesons. The general formalism was developed and applied to infinite isospin symmetric and asymmetric nuclear matter with a particular choice of the non-linear derivative terms that lead to an energy dependence of the self-energies. In Ref. [109] the approach was extended with generalized non-linear derivative couplings of any functional form in the field-theoretical formalism allowing for a momentum or energy dependence. Nonlinear self-couplings of the $\sigma$ meson field were added in order to improve the description of characteristic nuclear matter parameters at saturation. The application of this version of the NLD model to stellar matter yielded a maximum NS mass of 2.03 $M_\odot$ barely satisfying the observational constraints but the dependence of the result on the model parameters was not explored in detail. The NLD model was also applied to the description of bulk properties of nuclear matter by Chen [124]. A softening of the EOS and maximum masses of NSs substantially below 2 $M_\odot$ were found with different parametrizations assuming an energy dependence of the couplings, but nonlinear self-couplings of the mesons or density dependent meson-nucleon couplings were not considered. Properties of finite nuclei were studied in reference [125] after adding meson self-interactions in the Lagrangian. A qualitative description similar to conventional RMF models was achieved but NS properties were not examined in this extended model.

The next step is to introduce the energy/momentum dependence in the just defined scalar and vector potentials of the RMF model with density dependent couplins, in order to modify the energy dependence of optical potential. The formalism for this procedure is explained in the next chapter.

# 4 Generalized RMF model with density-dependent non-linear derivative couplings

We introduce an extension of the nonlinear derivative (NLD) model assuming density dependent (DD) meson-nucleon couplings, the DD-NLD model, that is more flexible than previous versions. Instead of using derivative operators that generate an explicit momentum dependence of the self-energies, we will use a functional form that leads to an energy dependence. This approach will also be more suitable for an applications of the DD-NLD model to nuclei since the relevant equations and their numerical implementation are simplified. Here, the EOS of symmetric and asymmetric nuclear matter will be calculated for different choices of the derivative coupling operators that lead to a saturation of the optical potential at high energies as derived from experiments. They are compared to the results of a standard RMF model with density dependent couplings that is consistent with essentially all modern constraints for the characteristic nuclear matter parameters at saturation. The parameters of the DD-NLD models are chosen such that these saturation properties are reproduced. We study the effect of the optical potential constraint on the stiffness of the EOS and on the M-R relations of NSs.

## 4.1 Lagrangian density and field equations

In the DD-NLD model the Lagrangian density of free nucleons (19) and free mesons (20) stays the same as in the standard RMF model with density dependent couplings, taking into account the $\sigma$, $\omega$ and $\rho$ mesons. The generalization appears in the interaction part, where the minimal nucleon meson coupling is modified to include higher-order derivative terms. The nucleon field $\Psi$ ($\overline{\Psi}$) in $\mathscr{L}_{int}$ is replaced by $D_m\Psi$ ($\overline{D_m\Psi}$) with operator functions $D_m$, where $m$ stands for different meson species $m = \sigma, \omega, \rho$ since in general we can choose different operator functions for them. The additional operators $D_m$ can be expanded in an infinite series of higher-order derivative terms

$$D_m(x) = \sum_{n=0}^{\infty} \frac{d_n^{(m)}}{n!} x^n \,, \tag{45}$$

where $x$ is the argument that contains derivatives $i\partial_\beta$ that act on a nucleon field. We write it as

$$x = v^\beta i\partial_\beta - sm \,, \tag{46}$$

a hermitian Lorentz scalar operator with an auxiliary vector $v^\beta = (v_0, \overrightarrow{v})$ and a scalar factor $s$. The quantities $d_n^{(m)}$ are numerical coefficents given by the partial derivatives of $D$ with respect to the operator argument $x$

$$d_n^{(m)} = \frac{\partial^n}{\partial x^n} D_m|_{x\to 0} \,. \tag{47}$$

With this, the conventional interaction term (22) in the Lagrangian density (18) now has the form

$$\begin{aligned} \mathscr{L}_{\text{int}} \;=\; & \frac{1}{2}\Gamma_\sigma\sigma\left(\overline{\Psi}\overleftarrow{D}_\sigma\Psi + \overline{\Psi}\overrightarrow{D}_\sigma\Psi\right) \\ & -\frac{1}{2}\Gamma_\omega\omega_\mu\left(\overline{\Psi}\overleftarrow{D}_\omega\gamma^\mu\Psi + \overline{\Psi}\gamma^\mu\overrightarrow{D}_\omega\Psi\right) \\ & -\frac{1}{2}\Gamma_\rho\overrightarrow{\rho}_\mu\cdot\left(\overline{\Psi}\overleftarrow{D}_\rho\gamma^\mu\overrightarrow{\tau}\Psi + \overline{\Psi}\overrightarrow{\tau}\gamma^\mu\overrightarrow{D}_\rho\Psi\right) , \end{aligned} \tag{48}$$

symmetrized with respect to the derivative operators $D_m$, i.e.

$$\overrightarrow{D}_m = \sum_{k=0}^{\infty} C_k^{(m)} (v^\beta i \overrightarrow{\partial}_\beta)^k \tag{49}$$

$$\overleftarrow{D}_m = \sum_{k=0}^{\infty} C_k^{(m)} (-v^\beta i \overleftarrow{\partial}_\beta)^k \tag{50}$$

with coefficients

$$C_k^{(m)} = \sum_{k=0}^{n} \frac{d_n^{(m)}}{n!} \binom{n}{k} (-sm)^{n-k} . \tag{51}$$

(see appendix B.1 for details). Obviously, no derivatives appear for the choice $D_m = 1$ (corresponding to $d_n^{(m)} = \delta_{n0}$) and the standard form of the interaction (22) is recovered. The full DD-NLD Lagrangian density with generalized nucleon-meson interaction part is summed up in the following equation

$$\begin{aligned}
\mathscr{L}^{DD-NLD} = & \frac{1}{2}\left(\overline{\Psi}\gamma_\mu i\overrightarrow{\partial^\mu}\Psi - \overline{\Psi} i\overleftarrow{\partial^\mu}\gamma_\mu\Psi\right) - m\overline{\Psi}\Psi \\
& + \frac{1}{2}\Big(\partial_\mu\sigma\partial^\mu\sigma - m_\sigma^2\sigma^2 - \frac{1}{2}F_{\mu\nu}^{(\omega)}F^{(\omega)\mu\nu} + m_\omega^2\omega_\mu\omega^\mu \\
& - \frac{1}{2}\overrightarrow{F}_{\mu\nu}^{(\rho)} \cdot \overrightarrow{F}^{(\rho)\mu\nu} + m_\rho^2\overrightarrow{\rho}_\mu \cdot \overrightarrow{\rho}^\mu - \frac{1}{2}F_{\mu\nu}^{(\gamma)}F^{(\gamma)\mu\nu}\Big) \\
& + \frac{1}{2}\Gamma_\sigma\sigma\left(\overline{\Psi}\overleftarrow{D_\sigma}\Psi + \overline{\Psi}\overrightarrow{D_\sigma}\Psi\right) - \frac{1}{2}\Gamma_\omega\omega_\mu\left(\overline{\Psi}\overleftarrow{D_\omega}\gamma^\mu\Psi + \overline{\Psi}\gamma^\mu\overrightarrow{D_\omega}\Psi\right) \\
& - \frac{1}{2}\Gamma_\rho\overrightarrow{\rho_\mu}\cdots\left(\overline{\Psi}\overleftarrow{D_\rho}\gamma^\mu\overrightarrow{\tau}\Psi + \overline{\Psi}\overrightarrow{\tau}\gamma^\mu\overrightarrow{D_\rho}\Psi\right) \\
& - \frac{1}{2}\Gamma_\gamma\,\overline{\Psi}\gamma^\mu\frac{1+\tau_3}{2}A_\mu\Psi
\end{aligned} \tag{52}$$

where the first row stands for free nucleons, the following two rows describe free mesons and photons respectively, the next two rows give the nucleon-meson interaction while the last row stands for photon interaction.

To obtain field-equations we need to use the generalized Euler-Lagrange equation whose Lagrangian density contains the higher-order field derivatives

$$\mathscr{L}\left[\varphi_r(x), \partial_{\alpha_1}\varphi_r(x), \ldots, \partial_{\alpha_1,\ldots,\alpha_n}\varphi_r(x)\right] . \tag{53}$$

where $\partial_\alpha \equiv \frac{\partial}{\partial x^\mu}$. The derivation follows from the variation principle for the action $S = \int d^4x\mathscr{L}(x)$ with the Lagrangian of eq. (53) where $\varphi_r(x), \partial_{\alpha_1}\varphi_r(x), \partial_{\alpha_1,\ldots,\alpha_n}\varphi_r(x)$ are considered to be independent generalized coordinates. Through the principle of least action $\delta S = 0$ and by the variation of generalized coordinates we obtain the generalized Euler-Lagrange equation

$$\frac{\partial\mathscr{L}}{\partial\varphi_r} + \sum_{i=1}^{\infty}(-)^i\partial_{\alpha_1,\ldots,\alpha_i}\frac{\partial\mathscr{L}}{\partial(\partial_{\alpha_1,\ldots,\alpha_i}\varphi_r)} = 0 \tag{54}$$

for nucleons ($\varphi_r = \Psi, \overline{\Psi}$). For the meson fields $\varphi_r = \sigma, \omega_\mu, \rho_\mu$ the standard Euler-Lagrange equation applies, i.e. only the $i = 1$ term in equation (54) is relevant because only the first-order derivatives of the meson fields appear in the Lagrangian density $\mathscr{L}$. Details can be found in references [121, 109].

The field equation of nucleons, the Dirac equation derived in appendix B.2, is given by

$$\left[\gamma_\mu(i\partial^\mu - \Sigma^\mu) - (m - \Sigma)\right]\Psi = 0 , \tag{55}$$

which at first looks the same as in the standard RMF approaches. However, the difference occurs in scalar ($\Sigma$) and vector ($\Sigma^\mu$) self-energies. In addition to the multiplication of meson-nucleon couplings and the meson field that is present in standard RMF, they now contain the derivative operators $D_m$

$$\begin{aligned} \Sigma &= \Gamma_\sigma \sigma \overrightarrow{D}_\sigma \,, & (56)\\ \Sigma^\mu &= \Gamma_\omega \omega^\mu \overrightarrow{D}_\omega + \Gamma_\rho \overrightarrow{\tau} \cdot \overrightarrow{\rho}^\mu \overrightarrow{D}_\rho + \Gamma_\gamma \frac{1+\tau_3}{2} A^\mu + \Sigma_R^\mu \,. & (57) \end{aligned}$$

The so-called "rearrangement contribution" in eq. (57) now also includes additional derivative operators and has the form

$$\begin{aligned} \Sigma_R^\mu = \frac{j^\mu}{n_v} \Big[ & \Gamma'_\omega \omega^\nu \frac{1}{2} \left( \overline{\Psi} \overleftarrow{D}_\omega \gamma_\nu \Psi + \overline{\Psi} \gamma_\nu \overrightarrow{D}_\omega \Psi \right) \\ & + \Gamma'_\rho \overrightarrow{\rho}^\nu \cdot \frac{1}{2} \left( \overline{\Psi} \overleftarrow{D}_\rho \gamma_\nu \overrightarrow{\tau} \Psi + \overline{\Psi} \gamma_\nu \overrightarrow{\tau} \overrightarrow{D}_\rho \Psi \right) \\ & - \Gamma'_\sigma \sigma \frac{1}{2} \left( \overline{\Psi} \overleftarrow{D}_\sigma \Psi + \overline{\Psi} \overrightarrow{D}_\sigma \Psi \right) \Big] \,. \end{aligned} \tag{58}$$

In the case of inhomogeneous systems and a non-vanishing three-vector component $\vec{v}$ of the auxiliary vector $v^\beta$, additional terms in (56) and (57) will appear. In the present application of the DD-NLD model we do not consider this case.

The field equations of mesons (see appendix B.3) maintain the same shape as before but with the source terms containing derivative operators

$$\begin{aligned} \partial_\mu \partial^\mu \sigma + m_\sigma^2 \sigma &= \frac{1}{2} \Gamma_\sigma \left( \overline{\Psi} \overleftarrow{D}_\sigma \Psi + \overline{\Psi} \overrightarrow{D}_\sigma \Psi \right) \\ \partial_\mu F^{(\omega)\mu\nu} + m_\omega^2 \omega^\nu &= \frac{1}{2} \Gamma_\omega \left( \overline{\Psi} \overleftarrow{D}_\omega \gamma^\nu \Psi + \overline{\Psi} \gamma^\nu \overrightarrow{D}_\omega \Psi \right) \\ \partial_\mu \overrightarrow{F}^{(\rho)\mu\nu} + m_\rho^2 \overrightarrow{\rho}^\nu &= \frac{1}{2} \Gamma_\rho \left( \overline{\Psi} \overleftarrow{D}_\rho \gamma^\nu \overrightarrow{\tau} \Psi + \overline{\Psi} \overrightarrow{\tau} \gamma^\nu \overrightarrow{D}_\rho \Psi \right) . \end{aligned} \tag{59}$$

## 4.2 Baryon current and energy-momentum tensor

The Noether theorem follows from invariance of the Lagrangian density (53) with respect to the infinitesimal transformation of all the fields and their coordinates, which implies

$$\mathscr{L}\left[ \varphi'_r(x'), \partial'_{\alpha_1} \varphi'_r(x'), \ldots, \partial'_{\alpha_1,\ldots,\alpha_n} \varphi'_r(x') \right] = \mathscr{L}\left[ \varphi_r(x), \partial_{\alpha_1} \varphi_r(x), \ldots, \partial_{\alpha_1,\ldots,\alpha_n} \varphi_r(x) \right] . \tag{60}$$

We can define a total variation of the Lagrange density as

$$\delta_T \mathscr{L} = \mathscr{L}\left[ \varphi'_r(x'), \partial'_{\alpha_1} \varphi'_r(x'), \ldots, \partial'_{\alpha_1,\ldots,\alpha_n} \varphi'_r(x') \right] - \mathscr{L}\left[ \varphi_r(x), \partial_{\alpha_1} \varphi_r(x), \ldots, \partial_{\alpha_1,\ldots,\alpha_n} \varphi_r(x) \right] = 0 \,. \tag{61}$$

Starting from here, the goal is to derive a continuity equation of the form

$$\partial_\mu f^\mu = 0 \tag{62}$$

with $f^{\mu}$ being a conserved current to be determined. Detailed derivation can be found in appendix B of Ref. [109]. The final and general expression for the Noether theorem is obtained as

$$\begin{aligned}
\delta\mathscr{L} \;=\; & \partial_{\mu}\Bigg[\Big(\frac{\partial\mathscr{L}}{\partial(\partial_{\mu}\varphi_r)}-\partial_{\alpha_1}\frac{\partial\mathscr{L}}{\partial(\partial_{\mu\alpha_1}\varphi_r)}-\ldots+(-)^n\partial_{\alpha_1,\ldots,\alpha_n}\frac{\partial\mathscr{L}}{\partial(\partial_{\mu\alpha_1,\ldots,\alpha_n}\varphi_r)}\Big)\\
&(\delta_T\varphi_r-\partial_{\alpha}\varphi_r\delta x^{\alpha})\\
&+\Big(\frac{\partial\mathscr{L}}{\partial(\partial_{\mu\sigma_1}\varphi_r)}-\partial_{\alpha_1}\frac{\partial\mathscr{L}}{\partial(\partial_{\mu\sigma_1\alpha_1}\varphi_r)}+\ldots+(-)^n\partial_{\alpha_1,\ldots,\alpha_n}\frac{\partial\mathscr{L}}{\partial(\partial_{\mu\sigma_1\alpha_1,\ldots,\alpha_n}\varphi_r)}\Big)\\
&\partial_{\sigma_1}(\delta_T\varphi_r-\partial_{\alpha}\varphi_r\delta x^{\alpha})\\
&+\Big(\frac{\partial\mathscr{L}}{\partial(\partial_{\mu\sigma_1\sigma_2}\varphi_r)}-\partial_{\alpha_1}\frac{\partial\mathscr{L}}{\partial(\partial_{\mu\sigma_1\sigma_2\alpha_1}\varphi_r)}+\ldots+(-)^n\partial_{\alpha_1,\ldots,\alpha_n}\frac{\partial\mathscr{L}}{\partial(\partial_{\mu\sigma_1\sigma_2\alpha_1,\ldots,\alpha_n}\varphi_r)}\Big)\\
&\partial_{\sigma_1\sigma_2}(\delta_T\varphi_r-\partial_{\alpha}\varphi_r\delta x^{\alpha})+\\
&\vdots\\
&+\Big(\frac{\partial\mathscr{L}}{\partial(\partial_{\mu\sigma_1\sigma_2\ldots\sigma_n}\varphi_r)}-\partial_{\alpha_1}\frac{\partial\mathscr{L}}{\partial(\partial_{\mu\sigma_1\ldots\sigma_n\alpha_1}\varphi_r)}+\ldots+(-)^n\partial_{\alpha_1,\ldots,\alpha_n}\frac{\partial\mathscr{L}}{\partial(\partial_{\mu\sigma_1\sigma_2\alpha_1,\ldots,\alpha_n}\varphi_r)}\Big)\\
&\partial_{\sigma_1,\ldots,\sigma_n}(\delta_T\varphi_r-\partial_{\alpha}\varphi_r\delta x^{\alpha})\\
&-g^{\mu\alpha}\mathscr{L}\delta x_{\alpha}\Bigg].
\end{aligned}\tag{63}$$

We look at the invariance of the Lagrange density under the transformations in order to find conserved quantities. Invariance of the Lagrangian density with respect to global phase transformations

$$\varphi_r(x)\to\varphi_r'(x)=e^{-i\epsilon}\varphi_r(x)\tag{64}$$

leads to continuity equation $\partial_{\mu}J^{\mu}=0$ for the conserved Noether current $J^{\mu}$. If we look at the invariance with respect to a constant displacement $\delta_{\mu}$ of the coordinates $x_{\mu}$

$$x_{\mu}\to x_{\mu}'=x_{\mu}+\delta_{\mu}\,,\tag{65}$$

we obtain the continuity equation $\partial_{\mu}T^{\mu\nu}=0$ for energy-momentum tensor $T^{\mu\nu}$.

For the DD-NLD model, when the Lagrangian density $\mathscr{L}^{DD-NLD}$ (52) is used, the conserved baryon current is evaluated to be

$$J^{\mu}=\sum_{i=p,n}\langle\overline{\Psi}_i N^{\mu}\Psi_i\rangle\tag{66}$$

where $N^{\mu}$ is the norm operator equal to

$$N^{\mu}=\gamma^{\mu}+\Gamma_{\sigma}\sigma\left(\partial_p^{\mu}D_{\sigma}\right)-\Gamma_{\omega}\omega_{\alpha}\gamma^{\alpha}\left(\partial_p^{\mu}D_{\omega}\right)-\Gamma_{\rho}\overrightarrow{\rho}_{\alpha}\cdot\gamma^{\alpha}\overrightarrow{\tau}\left(\partial_p^{\mu}D_{\rho}\right).\tag{67}$$

The $\partial_p^{\mu}D_m$ is the derivative of $D_m$ operator with respect to the momentum $p_{\mu}=i\partial_{\mu}$, i.e.

$$\partial_p^{\mu}D_m=v^{\mu}\sum_{k=1}^{\infty}kC_k^{(m)}(v^{\beta}i\partial_{\beta})^{k-1}\,.\tag{68}$$

In eq. (67) the first term corresponds to the standard expression for the vector current

$$J_v^{\mu}=\sum_{i=p,n}\langle\overline{\Psi}_i\gamma^{\mu}\Psi_i\rangle\,,\tag{69}$$

which is used to define the vector density

$$n_v = \sqrt{J^\mu_v J_{v\mu}} \tag{70}$$

appearing as the argument of the coupling functions $\Gamma_i$. The vector and baryon current differ from each other by additional contributions in the baryon current that arise due to the additional higher-order field derivatives.

With a similar evaluation procedure the energy-momentum tensor's general form is obtained

$$T^{\mu\nu} = \sum_{i=p,n} \langle \overline{\Psi}_i N^\mu p^\nu \Psi_i \rangle - g^{\mu\nu} \langle \mathscr{L} \rangle \,. \tag{71}$$

The higher-order derivative terms will introduce additional kinetic terms that will be important for the thermodynamic consistency of the model. The energy density $\varepsilon$ and pressure $P$ are found from $\varepsilon = T^{00}$ and $P = \sum_{i=1}^{3} T^{ii}/3$, respectively. They provide the EOS of nuclear matter as a function of the baryon density $n_B = J^0$.

## 4.3 DD-NLD model for nuclear matter

A considerable simplification of the equations occurs if we apply our model to infinite nuclear matter, an idealized system of nucleons interacting only by nuclear forces but not Coulomb forces. The volume and the number of particles are infinite which implies no surface effects and translational invariance where only difference in position matters, not the absolute position. It is the simplest, yet already highly non-trivial system. Since infinite nuclear matter is homogeneous and isotropic, the meson fields, which are treated as classical fields, are constant in space and time. Positive-energy solutions of the Dirac equation (55) are found with the plane wave ansatz

$$\Psi_i(\overrightarrow{p}_i, \sigma, \tau) = u_i(\overrightarrow{p}_i, \sigma, \tau) \exp\left(-i p_i^\mu x_\mu\right) \tag{72}$$

for protons and neutrons with four momentum $p_i^\mu = (E_i, \overrightarrow{p}_i)$, positive energy $E_i$ and quantum numbers of spin and isospin marked with $\sigma$ and $\tau$, respectively. Dirac spinors $u_i$ are normalized according to

$$\overline{\Psi}_i N^0 \Psi_i = \bar{u}_i N^0 u_i = 1 \tag{73}$$

with the time component of the norm operator (67). They depend on the effective mass

$$m_i^* = m_i - \Sigma_i \tag{74}$$

and effective momentum

$$p_i^{*\mu} = p_i^\mu - \Sigma_i^\mu \tag{75}$$

which are related by the dispersion relation (40).

A further simplification appears in the $D_m$ operators where the $i\partial^\beta$ can be replaced by the corresponding four-momentum $p_i^\beta = (E_i, \vec{p}_i)$ resulting in a simple function $D_m$ depending on the energy $E_i$ and the momentum $\vec{p}_i$ of the nucleon. Using the identity

$$N^\mu \Psi_i = \left[\gamma^\mu + \partial_p^\mu \Sigma_i - \gamma_\alpha \partial_p^\mu \left(\Sigma_i^\alpha - \Sigma_R^\alpha\right)\right] \Psi_i \tag{76}$$

the conserved current and the energy-momentum tensor in infinite nuclear matter can be written as

$$J^\mu = \sum_{i=p,n} \kappa_i \int \frac{d^3p}{(2\pi)^3} \frac{\Pi_i^\mu}{\Pi_i^0} \tag{77}$$

and

$$T^{\mu\nu} = \sum_{i=p,n} \kappa_i \int \frac{d^3p}{(2\pi)^3} \frac{\Pi_i^\mu p^\nu}{\Pi_i^0} - g^{\mu\nu}\langle \mathscr{L} \rangle \,, \tag{78}$$

respectively, with the four-momentum

$$\Pi_i^\mu = p_i^{*\mu} + m_i^* \left(\partial_p^\mu \Sigma_i\right) - p_{i\beta}^* \left[\partial_p^\mu \left(\Sigma_i^\beta - \Sigma_R^\beta\right)\right] \tag{79}$$

and spin degeneracy factors $\kappa_i = 2$. The integration runs over all momenta $p$ with modulus lower than the Fermi momenta $p_{Fi}$ in the no-sea approximation. They are defined through the individual nucleon densities

$$n_i = \kappa_i \int_o^{p_{Fi}} \frac{d^3p}{(2\pi)^3} \,. \tag{80}$$

Without the preference for a particular direction in infinite nuclear matter, the spatial components of the Lorentz vector meson fields vanish and the auxiliary vector in equation (46) is set to $v^\beta = \delta_{\beta 0}$ such that the $D_m$ functions only depend on the nucleon energy $E_i$. Without isospin changing processes, only the third component of the isovector $\rho$ field has to be considered in the field equations for the mesons. The meson fields are immediately obtained from the field equations (59) with source densities $n_\sigma$, $n_\omega$, and $n_\rho$ defined as

$$\begin{aligned} n_\sigma &= n_p^{sD} + n_n^{sD} = \sum_{i=p,n} \langle \overline{\Psi}_i D_\sigma \Psi_i \rangle \\ n_\omega &= n_p^{vD} + n_n^{vD} = \sum_{i=p,n} \langle \overline{\Psi}_i \gamma^0 D_\omega \Psi_i \rangle \\ n_\rho &= n_p^{vD} - n_n^{vD} = \sum_{i=p,n} \langle \overline{\Psi}_i \gamma^0 \tau_3 D_\rho \Psi_i \rangle \,. \end{aligned} \tag{81}$$

The new "scalar" and "vector" source densities (marked with (sD) and (vD) in the superscript) for neutrons and protons in the above equations are defined similar as the nucleon densities (80) but now the integration over the momentum is more complicated since the self-energies are energy dependent. If we introduce the energy-dependent scalar potential $S_i(E_i) = \Sigma_i$ and vector potential $V_i(E_i) = \Sigma_i^0$, the dispersion relation reads

$$E_i = \sqrt{p^2 + [m_i - S_i(E_i)]^2} + V_i(E_i) \,. \tag{82}$$

For the calculation of nucleon densities it is more convinient to introduce an energy integration by substitution, since the scalar and vector potentials are explicit functions of the energy $E_i$ of the nucleon $i$. The details of the integration variable exchange are given in the appendix (B.4). The final density expressions are given by

$$\begin{aligned} n_i^{(sD)} &= \kappa_i \int_0^{p_{Fi}} \frac{d^3p}{(2\pi)^3} \frac{m_i^*}{\Pi_i^0} D(E_i) \\ &= \frac{\kappa_i}{2\pi^2} \int_{E_i^{(\min)}}^{E_i^{(\max)}} dE_i \, p(E_i)[m_i - S_i(E_i)] D(E_i) \end{aligned} \tag{83}$$

and

$$\begin{aligned} n_i^{(vD)} &= \kappa_i \int_0^{p_{Fi}} \frac{d^3p}{(2\pi)^3} \frac{E_i^*}{\Pi_i^0} D(E_i) \\ &= \frac{\kappa_i}{2\pi^2} \int_{E_i^{(\min)}}^{E_i^{(\max)}} dE_i \, p(E_i)[E - V_i(E_i)] D(E_i) \end{aligned} \tag{84}$$

assuming $D = D_\sigma = D_\omega = D_\rho$. The lower and upper boundaries of the integrals are determined by solving the equations

$$\begin{aligned} E_i^{(\min)} &= \left| m_i - S_i(E_i^{(\min)}) \right| + V_i(E_i^{(\min)}) \\ E_i^{(\max)} &= \sqrt{p_{Fi}^2 + \left[ m_i - S_i(E_i^{(\max)}) \right]^2} + V_i(E_i^{(\max)}) \end{aligned} \tag{85}$$

respectively, with the Fermi momenta $p_{Fi}$ from equation (80). The argument of the coupling functions $n_v = n_p^{(v)} + n_n^{(v)}$ can be obtained from

$$\begin{aligned} n_i^{(v)} &= \kappa_i \int_0^{p_{Fi}} \frac{d^3p}{(2\pi)^3} \frac{E_i^*}{\Pi_i^0} \\ &= \frac{\kappa_i}{2\pi^2} \int_{E_i^{(\min)}}^{E_i^{(\max)}} dE_i \, p(E_i) [E_i - V_i(E_i)] \, . \end{aligned} \tag{86}$$

The self-energies simplify to

$$\begin{aligned} \Sigma_i &= \Gamma_\sigma \sigma D_\sigma(E) \\ \Sigma_i^0 &= \Gamma_\omega \omega D_\omega(E) + \Gamma_\rho \tau_{3,i} \rho D_\rho(E) + \Sigma_R^0 \\ \vec{\Sigma}_i &= 0 \end{aligned} \tag{87}$$

with $\tau_{3,i} = +1$ $(-1)$ for protons (neutrons). The 'rearrangement' contribution

$$\Sigma_R^0 = \Gamma'_\omega \omega n_\omega + \Gamma'_\rho \rho n_\rho - \Gamma'_\sigma \sigma n_\sigma \tag{88}$$

is independent of the nucleon energy.

From the energy-momentum tensor (71), the energy density assumes the form

$$\begin{aligned} \varepsilon &= \sum_{i=p,n} \kappa_i \int_0^{p_{Fi}} \frac{d^3p}{(2\pi)^3} E_i - \langle \mathscr{L} \rangle \\ &= \frac{\kappa_i}{2\pi^2} \int_{E_i^{(\min)}}^{E_i^{(\max)}} dE_i \, p(E_i) \Pi_i^0(E_i) E_i - \langle \mathscr{L} \rangle \end{aligned} \tag{89}$$

and the pressure is given by

$$\begin{aligned} P &= \frac{1}{3} \sum_{i=p,n} \kappa_i \int_0^{p_{Fi}} \frac{d^3p}{(2\pi)^3} \frac{p^2}{\Pi_i^0} + \langle \mathscr{L} \rangle \\ &= \sum_{i=p,n} \frac{\kappa_i}{6\pi^2} \int_{E_i^{(\min)}}^{E_i^{(\max)}} dE_i \, [p(E_i)]^3 + \langle \mathscr{L} \rangle \end{aligned} \tag{90}$$

with

$$\langle \mathscr{L} \rangle = \frac{1}{2} \left( \Gamma_\omega \omega n_\omega + \Gamma_\rho \rho n_\rho - \Gamma_\sigma \sigma n_\sigma \right) + \left( \Gamma'_\omega \omega n_\omega + \Gamma'_\rho \rho n_\rho - \Gamma'_\sigma \sigma n_\sigma \right) n_v \, . \tag{91}$$

To summarize, the procedure is the following: in the first step, we build a Lagrangian density containing all the interaction terms of nucleons and mesons. This will depend on our choice of couplings and is model dependent. Second, by an application of the least action principle, one gets a set of equations of motion. The nucleons obey the Dirac equation, whilst the mesons obey Klein-Gordon equations. Through an iterative procedure we obtain the needed meson fields, couplings and densities (the $n_\sigma$, $n_\omega$, $n_\rho$ and $n_v$) for protons and neutrons. With the continuity equations of Noether current and energy-momentum tensor the energy density and pressure are obtained, which gives the EOS of infinite nuclear matter.

## 4.4 Thermodynamic consistency

For RMF models it is sufficient to check that the thermodynamic definition of the pressure

$$P = n_B^2 \frac{\partial(\epsilon/n_B)}{\partial n_B} \tag{92}$$

is identical to the pressure obtained from the energy-momentum tensor

$$P = \frac{1}{3}(T^{xx} + T^{yy} + T^{zz}) \tag{93}$$

with the energy density $\epsilon = T^{00}$ in order to show that thermodynamic consistency is fulfilled. Then also Euler's theorem

$$\epsilon = -P + \sum_{i=p,n} \mu_i \rho_{Bi} \tag{94}$$

holds with the chemical potentials given by $\mu_i = \frac{\partial \epsilon}{\partial \rho_{B_i}}$ (see appendix B.6).

## 4.5 DD-NLD model for stellar matter

The DD-NLD model can be used to predict the properties of NSs. For that, the EoS of stellar matter is required. In this work, when we talk about stellar matter we are refering to matter in the core of a NS, at densities above saturation where the matter is homogeneous. For the crust at lower densities the EOS is relatively well known since enough data is available for this density region from many different measurements. There are several crust EOSs that can be used and matched to the high density EOS. For now the low density part of NS, the solid crust, will not concern us and we will refer to it in more detail in chapter 7. The inner core of NS is the densest part and there are several possibilities for its content, as it was already discussed in the introduction. However, the presence of exotic matter in NS interior softens the EOS considerably and many of these hybrid models are not able to reach the constraint of the maximum NS mass. In this work we assume that stellar matter in the NS core is homogeneous and composed of neutrons, protons and electrons, or more generally charged leptons, without exotic particles.

Stellar matter is obtained by expanding the nuclear matter model by adding the contribution of electrons to the energy density and pressure of the baryons. The electron contribution to the Lagrangian density is

$$\mathscr{L}_e = \overline{\Psi}_e \left( i\gamma^\mu \partial_\mu - m_e \right) \Psi_e \tag{95}$$

with the mass of the electron equal to 0.511 MeV. In addition to this, stellar matter has to satisfy two conditions, charge neutrality and $\beta$ equilibrium that fix the lepton density and the proton-neutron asymmetry uniquely. Charge neutrality requires that the densities of leptons, in this case electrons, and protons are equal $n_e = n_p$ while the $\beta$ equilibrium condition ensures that the total energy density of the system is minimal when weak interaction reactions are allowed. That means that for the system of $p$, $n$ and $e^-$ at fixed baryon density and with charge neutrality condition, we want to minimize $\epsilon(n_p, n_n, n_e)$. This is done by the method of Lagrange multipliers. From here the $\beta$ equilibrium relation follows (derivation in appendix B.7)

$$\mu_n = \mu_p + \mu_e \,. \tag{96}$$

It ensures that the particle levels are filled to such a point that no energy can be extracted from the gas by a neutron undergoing a beta decay or a proton undergoing an inverse beta decay since all levels below the Fermi energies are blocked. With these additional requirements the stellar EOS is obtained in the same way as the EOS of nuclear matter.

## 4.6 The model code and its extensions

The starting point for the calculations in DD-NLD model is the existing code for RMF models [126] by S. Typel. Originally, the code has a possibility to calculate the EOS of infinite nuclear matter, the properties of nuclei, both with spherical and axial symmetry, and to perform a fit of parameters both to nuclear matter properties and properties of nuclei. There are several possibilities for the type of RMF model already implemented, among which we are extending the model with density-dependent meson-nucleon couplings. The extension consists of introducing the new source densities with energy dependent D function as in equations 83 and 84. This is done both in the cases of infinite nuclear matter and finite nuclei calculations.

In case of infinite nuclear matter, the possibility to calculate the EOS for different proton fractions is implemented, so the EOS of stellar matter can be calculated while the $\beta$-equilibrium condition is satisfied. To get the mass-radius relation for a NS, the code to solve TOV equations [127] is used. Additionally, the density used in the parametrization of couplings had to be changed to the vector density (86), not the baryon density, since the two are different after the implementation of the D functions. For the calculation of finite nuclei, also the determination of the single-particle wave functions has to be modified because the potential depends of the single particle energy that is found by solving the Dirac equation. Hence, and additional iteration to obtain self-consistent solutions is needed. In the second part of this work where the thermodynamics of nuclear matter is studied, the temperature dependence had to be implemented in the code, which is done by the introduction of Fermi-Dirac distribution in the densities (104) and thermodynamic quantities (e.g. pressure and energy), explained in section 7.2.

# 5 Parametrization of density and energy dependence

The parameters entering the Lagrangian density have to be specified in order to calculate the actual properties of nuclear matter and atomic nuclei. There are several different ways to parametrize the density dependence of the meson-nucleon coupling functions $\Gamma_i(n)$. We want an approach that will be reliable not only around the saturation density of symmetric nuclear matter, but also in case of extrapolation to small and large densities. For that reason, the parametrization of the density dependence in the meson-baryon interaction is realized by assuming a smooth functional dependence that would give a reasonable behavior also under extreme conditions. The choice is guided by the results from Dirac-Bruckner (DB) calculations of nuclear matter. However, we do not directly use the density dependence obtained from a specific DB calculation but instead introduce an ansatz for the functional form with a small number of parameters that is able to span different DB results, as it was previously used in reference [117]. The actual parameters are obtained after fitting to properties of nuclear matter at saturation and several chosen finite nuclei properties.

## 5.1 Fit to nuclear matter properties at saturation density

For the parametrization of density-dependence of the nucleon-mesons couplings for $m = \sigma, \omega, \rho$ mesons the coupling functions are written as

$$\Gamma_m(n_v) = \Gamma_m(n_{\text{ref}}) f_m(x) \tag{97}$$

with the coupling constants $\Gamma_m(n_{\text{ref}})$ at the reference density $n_{\text{ref}}$ and functions $f_m$ dependent on the ratio $x = n_v/n_{\text{ref}}$. Notice the difference in the definition of the argument $x$ now and in the original reference [117], where it was given by $x = n_B/n_{\text{sat}}$. The vector density $n_v$ in the DD-NLD model is not identical to the baryon density $n_B$. In the DD model the reference density $n_{\text{ref}}$ is equal to the saturation density $n_{\text{sat}}$ of symmetric nuclear matter. In DD-NLD model however, the reference density corresponds to the vector density determined at saturation of symmetric nuclear matter. The functional form of $f_m(x)$ is assumed to be the same as introduced in ref. [117] for all of the mesons. In case of $\sigma$ and $\omega$ it is given by the rational function

$$f_m(x) = a_m \frac{1 + b_m(x + d_m)^2}{1 + c_m(x + d_m)^2} \tag{98}$$

with four coefficients, $a_m$, $b_m$, $c_m$ and $d_m$, that are not independent. In order to reduce the number of free parameters, the conditions $f_\sigma(1) = f_\omega(1) = 1$ and $f'_\sigma(0) = f'_\omega(0) = 0$ are demanded. With this, there are only two independent parameters for density dependence, $r_{21}(x)$ and $r_{10}(x)$, given as the ratios of the function $f_m(x)$ and/or its derivatives (see appendix C). With that, the functions $f_m(n_v/n_{\text{ref}})$ are determined which give the couplings $\Gamma_m(n_v)$.

The functional form is different for the $\rho$-meson coupling. Since DB calculations indicate a strong density dependence for the $\rho$ meson coupling, the chosen function is exponential

$$f_\rho(x) = \exp\left[-a_\rho\,(x-1)\right] \tag{99}$$

with one parameter $a_\rho$. Besides the usual parameters of RMF model with density-dependent couplings defined above, the implemented $D_m$ functions are responsible for the energy dependence of the self-energies. For the purpose of this work we will assume identical functions for all mesons, i.e. $D = D_\sigma = D_\omega = D_\rho$, and consider several different functional dependencies, some of them were previously explored within the NLD model [109, 121]. For application to nuclear matter we consider the following $D$ functions:

- D1 is a constant $D = 1$ that corresponds to a standard RMF model,
- D2 has a Lorentzian form $D = 1/(1 + x^2)$,

- D3 has an exponential dependence $D = \exp(-x)$

with $x = (E_i - m_{\rm nuc})/\Lambda$ and $m_{\rm nuc} = (m_n + m_p)/2$ because we set $v^\beta = \delta_{\beta 0}$ and $s = 1$ in equation (46). A new parameter $\Lambda$ appears, that regulates the strength of the energy dependence and it is interpreted as a cut-off parameter. Its value is assumed to be of natural hadronic scale of around 1 GeV.

In addition to the parameters of the functions $f_m$, the masses and coupling constants at reference density also enter our model. For the proton and neutron masses the experimental values of $m_p = 938.272046$ MeV/c$^2$ and $m_n = 939.565379$ MeV/c$^2$ are used, respectively. The meson masses are set to $m_\sigma = 550$ MeV/c$^2$ , $m_\omega = 783$ MeV/c$^2$, and $m_\rho = 763$ MeV/c$^2$. In principle, the masses of the mesons should also be included in the fit. The $\sigma$ meson mass will be considered as one of the parameters in the fit to properties of finite nuclei while the $\omega$ and $\rho$ meson masses are kept as the bare values, since their values always turn out to be close to the experimental ones. In total, there will be 11 independent parameters:

- mass of the $\sigma$ meson
- reference density for the density dependence of meson couplings $n_{\rm ref}$
- couplings of the mesons at reference density: $\Gamma_\sigma(n_{\rm ref})$, $\Gamma_\omega(n_{\rm ref})$ and $\Gamma_\rho(n_{\rm ref})$
- density dependence of the isoscalar mesons: $b_\sigma$, $b_\omega$, $d_\sigma$ and $d_\omega$
- density dependence of the isovector mesons: $a_\rho$
- cut-off strength parameter $\Lambda$ .

Since several of the parameters are strongly correlated it is convenient to perform the fit not directly in all of these parameters but to use saturation properties of SNM as independent variables in the fit and convert these quantities to the coupling constants analytically. The eight parameters for meson couplings and their density dependence, $\Gamma_m, \Gamma_m'$ for all mesons $m = \sigma, \omega, \rho$ and $\Gamma_m''$ for $\sigma$ and $\omega$ mesons, are completely determined through the values of $C_m$ coefficients and their derivatives at the reference density defined as

$$C_m = \left.\frac{\Gamma_m^2}{m_m^2}\right|_{n_v = n_{\rm ref}} \qquad C_m' = \left.\frac{d}{dn_v}\frac{\Gamma_m^2}{m_m^2}\right|_{n_v = n_{\rm ref}} \qquad C_m'' = \left.\frac{d^2}{dn_v^2}\frac{\Gamma_m^2}{m_m^2}\right|_{n_v = n_{\rm ref}} . \tag{100}$$

The coefficents $C_\omega, C_\sigma, C_\rho, C_\omega', C_\sigma', C_\rho', C_\omega'', C_\sigma''$ can be partially determined from characteristic nuclear matter parameters. The deduced values of the $C_m$ coefficients and their derivatives determine the $\Gamma_m$ values and derivatives for all mesons as

$$\begin{aligned} \Gamma_m &= \sqrt{C_j} m_j \\ \Gamma_m' &= \frac{\Gamma_j}{2}\frac{C_j'}{C_j} \\ \Gamma_m'' &= \frac{\Gamma_j}{2}\left[\frac{C_j''}{C_j} - \frac{1}{2}\left(\frac{C_j'}{C_j}\right)^2\right]. \end{aligned} \tag{101}$$

To summarize, we find the values for $C_m$ coefficients and their derivatives by fitting to nuclear matter properties. This determines the $\Gamma_m$ couplings and their derivatives. With the assumed values of ratios the $r_{21}$ and $r_{10}$ we can find the parameter $d_m$ through the recursion relation C.8 and from there the other coefficients follow (see appendix C). The last parameter $a_\rho$ is also determined through $C_m$ and $C_m'$, that is $\Gamma_\rho$ and $\Gamma_\rho'$ via eq. (C.10).

**Table 6:** Parametrization 1 (PRMT1): Parameters of the meson coupling functions for three choices of the $D$ functions and different values of the cut-off parameter $\Lambda$ when only nuclear matter parameters and the optical potential are fitted.

| Meson | Parameter | D1 | D2 | | D3 | |
|---|---|---|---|---|---|---|
| | $\Lambda$ [MeV] | – | 400 | 500 | 600 | 700 |
| $\sigma$ | $\Gamma_\sigma(n_{\text{ref}})$ | 10.72913 | 10.93466 | 10.86315 | 9.74679 | 9.89158 |
| | $a_\sigma$ | 1.36402 | 1.35816 | 1.36015 | 1.38410 | 1.38064 |
| | $b_\sigma$ | 0.53404 | 0.51914 | 0.52433 | 0.61515 | 0.60127 |
| | $c_\sigma$ | 0.86714 | 0.83989 | 0.84931 | 1.00615 | 0.98211 |
| | $d_\sigma$ | 0.62000 | 0.62998 | 0.62648 | 0.57558 | 0.58258 |
| $\omega$ | $\Gamma_\omega(n_{\text{ref}})$ | 13.29858 | 13.56462 | 13.47215 | 12.0503 | 12.23457 |
| | $a_\omega$ | 1.3822 | 1.3822 | 1.3822 | 1.3822 | 1.3822 |
| | $b_\omega$ | 0.42253 | 0.42253 | 0.42253 | 0.42253 | 0.42253 |
| | $c_\omega$ | 0.71932 | 0.71932 | 0.71932 | 0.71932 | 0.71932 |
| | $d_\omega$ | 0.60473 | 0.68073 | 0.68073 | 0.68073 | 0.68073 |
| $\rho$ | $\Gamma_\rho(n_{\text{ref}})$ | 3.59367 | 3.67852 | 3.64957 | 3.18819 | 3.25233 |
| | $a_\rho$ | 0.48762 | 0.48954 | 0.48872 | 0.34777 | 0.36279 |
| | $n_{\text{ref}}$ [fm$^{-3}$] | 0.15000 | 0.14618 | 0.147485 | 0.16515 | 0.16268 |

The model parameters are adjusted to the bulk properties of the symmetric nuclear matter and to the empirical energy dependence of the in-medium optical potential. When fitting the parameters, we require that the characteristic saturation properties for the three choices of the $D$ function are identical and close to current values extracted from experiments. In particular, we set the saturation density to $n_{\text{sat}} = 0.15$ fm$^{-3}$, the binding energy per nucleon at saturation to $B = 16$ MeV, the incompressibility to $K = 240$ MeV, the symmetry energy to $J = 32$ MeV and the symmetry energy slope coefficient to $L = 60$ MeV. Furthermore, we set the effective nucleon mass at saturation to $m_{\text{eff}} = 0.5625\ m_{\text{nuc}}$ (related to the strength of the spin-orbit potential in nuclei) and fix the ratios $r_{10}(1) = f'_\omega(1)/f_\omega(1) = -0.15$ and $r_{21}(1) = f''_\omega(1)/f'_\omega(1) = -1.0$ in order to determine the coefficients in the functions $f_m$ uniquely. These values are close to the ones of the DD2 parametrization [128] that was fitted to properties of nuclei and predicts a NS maximum mass of 2.4 $M_{\text{sol}}$.

Explicit values of the model parameters are given in Table 6 with two choices of the cut-off parameter $\Lambda$ for each of the energy dependent $D$ functions, Lorentzian and exponential. Note that the coefficients of the function $f_\omega$ are identical for all five parametrizations due to the constraints. The reference density $n_{\text{ref}}$ is not necessarily identical to the saturation density $n_{\text{sat}}$ since in the case of explicit derivative couplings the vector density $n_v$ is different from the conserved baryon density $n_B = J^0 = n_p + n_n$.

## 5.2 Fit to chosen observables of selected finite nuclei

When the parameters are fitted to finite nuclei properties we will abandon the $D3$ function with exponential energy dependence since the function we use should saturate for both particles and antiparticles, that is with both positive and negative energies. Therefore, we will use the $d4$ function instead

- $d4$ is equal to $D = \exp(-x^2)$ .

The functions are marked with a small "d" letter, after they are fitted to properties of nuclei, so we will have d1, d2 and d4 functions.

In fitting model parameters, one has the freedom of choosing different kinds of observables as well as nuclei included in the fit. Some choices are obvious, like binding energies as the most accurately

**Table 7:** Experimental values of observables for several chosen nuclei used in the fitting of model parameters: binding energies per nucleon $BE/A$, charge radii $r_{\text{charge}}$, diffraction radii $r_{\text{diff}}$, surface thickness $\sigma_{\text{surf}}$, and spin orbit splittings $\Delta_{so}^{(n)}(jnl)$ and $\Delta_{so}^{(p)}(jnl)$ for neutron and proton levels with principal quantum number n and orbital angular momentum l.

| Nuclei | Z | BE/A [MeV] | $r_{\text{charge}}$ [fm] | $r_{\text{diff}}$ radius [fm] | $\sigma_{surf}$ [fm] | $\Delta_{so}^{(n)}(nl)$ [MeV] | $\Delta_{so}^{(p)}(nl)$ [MeV] |
|---|---|---|---|---|---|---|---|
| $^{16}$O | 8 | -7.976206 | 2.699 | 2.764 | 0.8506 | 6.18 (0p) | 6.32 (0p) |
| $^{24}$O | 8 | -7.040 | - | - | - | - | - |
| $^{40}$Ca | 20 | -8.551303 | 3.478 | 3.850 | 0.9681 | - | - |
| $^{48}$Ca | 20 | -8.666689 | 3.477 | 3.963 | 0.8902 | 2.03 (1p), 8.39 (0f) | - |
| $^{56}$Ni | 28 | -8.642767 | - | - | - | 1.12 (0f), 7.16 (0f) | - |
| $^{90}$Zr | 40 | -8.709980 | 4.269 | 5.040 | 0.9571 | - | - |
| $^{100}$Sn | 50 | -8.253 | - | - | - | - | - |
| $^{132}$Sn | 50 | -8.354852 | 4.709 | - | - | - | 1.74 (1d), 6.09 (0g) |
| $^{208}$Pb | 82 | -7.867450 | 5.501 | 6.776 | 0.9186 | 0.90 (2p) | 1.33 (1d), 5.56 (0h) |

measured ground-state observables. Possible choices for additional observables include charge and/or diffraction radii, surface thicknesses, neutron skin thicknesses, spin-orbit splittings, single particle energies etc. The chosen nuclei are usually spherical since the adjustments of deformed nuclei are time consuming and would require a substantial extension of the available program code. Since RMF models are aimed to describe nuclei from $A \geq 16$ up to super-heavy nuclei with $A \approx 300$, the current mass range in our adjustment is taken from oxygen to lead isotopes. For that purpose, the following nuclei are included in the fitting procedure: $^{16}$O, $^{24}$O, $^{40}$Ca, $^{48}$Ca, $^{56}$Ni, $^{90}$Zr, $^{100}$Sn, $^{132}$Sn and $^{208}$Pb, including nuclei both close to and far away from the valley of stability. There is no unique and generally accepted strategy for the fitting procedure. We are performing a $\chi^2$ fit of parameters to the experimental values of chosen observables summed up in the table 7, collected from different sources [129, 130]. The $\chi^2$ value is given by

$$\chi^2 = \sum_{i,j} \left[ \frac{Q_i(N_j, Z_j) - Q_i^{\text{exp}}(N_j, Z_j)}{\Delta Q_i} \right]^2 \tag{102}$$

where the numerator is given by the difference between the predicted theoretical value of an observable and it's experimental value. The $\Delta Q_i$ stands for the error accounted for each observable, which are 0.1 MeV for binding energies, 0.01 fm for charge and diffraction radii, 0.005 fm in case of surface thickness and 0.1 MeV for the spin-orbit splittings. The sum goes over all the observables (i) taken into account in the fit procedure and the selected nuclei (j).

When fitting to properties of nuclei, the experimental values of the chosen observables are implemented in the code that is discussed in section 4.6. From there, the set of starting values for the model parameters serves as an imput with the assumed values of meson and nucleon masses, effective mass, saturation density, binding energy per nucleon, coupling $\Gamma_\rho$, incompressibility K, $a_\rho$ coefficent, ratios $r_{10}$ and $r_{21}$ and $\Lambda$ cut-off parameter. These values are then varied to reproduce best several chosen properties of a set of finite nuclei, given in Table 7. With each step of the iteration the coeffiecents $a_m$, $b_m$, $c_m$, $d_m$ and couplings $\Gamma_m$ are calculated, and the lowest $\chi^2$ value indicates the best fit (see table 8).

The "observables" (see [61] for definition) of each of the nuclei are calculated by solving the Dirac equation for the nucleon single-particle states on a Lagrange mesh. The Lagrange mesh method (LMM) [131, 132, 133] is a method that combines the virtues of usual discretization schemes and calculations with basis functions. In the present case it is used to solve the Dirac equation while it was at first

**Table 8:** Parametrization 2 (PRMT2): Parameters of the meson coupling functions for three choices of the $d$ functions and different values of cut-off parameter $\Lambda$ when properties of finite nuclei are included in the fit.

| Meson | Parameter | d1 | d2 | | d4 | |
|---|---|---|---|---|---|---|
| | $\Lambda$ [MeV] | – | 640 | 700 | 800 | 810 |
| $\sigma$ | $\Gamma_\sigma(n_{\rm ref})$ | 10.5392 | 10.54185 | 10.54454 | 10.56405 | 10.56090 |
| | $a_\sigma$ | 1.34854 | 1.34057 | 1.34175 | 1.34765 | 1.34848 |
| | $b_\sigma$ | 0.71263 | 0.36109 | 0.35575 | 0.40338 | 0.40954 |
| | $c_\sigma$ | 0.11063 | 0.59550 | 0.5886 | 0.66261 | 0.67225 |
| | $d_\sigma$ | 0.54892 | 0.74817 | 0.75254 | 0.70927 | 0.70416 |
| $\omega$ | $\Gamma_\omega(n_{\rm ref})$ | 13.1291 | 13.01978 | 13.02448 | 13.08205 | 13.07773 |
| | $a_\omega$ | 1.35253 | 1.3612 | 1.36117 | 1.36631 | 1.36688 |
| | $b_\omega$ | 0.55642 | 0.2668 | 0.26638 | 0.3039 | 0.3087 |
| | $c_\omega$ | 0.88812 | 0.46955 | 0.46891 | 0.52906 | 0.5367 |
| | $d_\omega$ | 0.61265 | 0.84255 | 0.84313 | 0.79376 | 0.78808 |
| $\rho$ | $\Gamma_\rho(n_{\rm ref})$ | 3.65275 | 3.65788 | 3.65786 | 3.65796 | 3.65797 |
| | $a_\rho$ | 0.5298 | 0.46735 | 0.49235 | 0.48675 | 0.49048 |
| | $n_{\rm ref}$ [fm$^{-3}$] | 0.15092 | 0.15401 | 0.15297 | 0.15266 | 0.152726 |

proposed and applied with great success in non-relativistic cases for the solution of the time-independent Schrödinger equation. Due to the dependence of the scalar and vector potentials on the single-particle energies, an additional iteration as compared to calculations in the standard DD-RMF model is required to find self-consistent solutions. The calculation on a mesh is performed by evaluating values of the wave-functions only at $x_i$ fixed mesh points. From the single-particle wave functions, the various source densities in the differential equations for the mesons and the photons are found including the effects of the D functions. The differential equations of the mesons are solved by using the appropriate Green's functions and the Gauss quadrature rule[3]. The Coulomb field is determined with the help of Fourier transformations with an adjustment to respect the correct boundary conditions. The densities and meson fields are discretized on a grid in a Legendre-Gauss basis with non-equidistant points. As an output we get nucleon orbits and occupations, the single particle energies, density distributions and the values of other properties derived from them that we were fitting to.

Additionally, the parameters are fitted to satisfy the optical potential and flow constraints. The requirement from the experimental side is that for a 1 GeV proton the optical potential has the value in the range of $U_{\rm opt} = (25 \pm 5)$ MeV, with the assumed error of 1 MeV. The model has to provide a sufficiently stiff EOS while respecting the flow constraint imposed by heavy-ion collision simulations. This is implemented by a requirement that at density value of $n_B = 0.48$ fm$^{-3}$ the pressure has to be $P = (49.6 \pm 23.8)$ MeV fm$^{-3}$. The assumed error is 2.38 MeV fm$^{-3}$, which is 10 times smaller than the required value to emphasize constraint.

In order to satisfy both requirements, we expect that the pressure-density relation of the EOS will pass along the upper border of the allowed shaded region in Fig. 9. The resulting parameters for models with the d1, d2 and d4 functions are given in Table 8, with two choices of $\Lambda$ value for the d2 and d4 functions. The values $\Lambda = 700$ MeV for d1 and $\Lambda = 800$ MeV were in a first fit of the parameters, and they are used in calculations of nuclear matter thermodynamic properties in section 7. With additional iterations, the lower $\chi^2$ value is obtained for the cases of $\Lambda = 640$ MeV for d2 and $\Lambda = 810$ MeV for d4 functions and the corresponding parameters were used for the calculations of finite nuclei properties in subsection 6.3.

[3] Seeks to obtain the best numerical estimate of an integral by picking optimal $x_i$ at which to evaluate the function $f(x)$

# 6 Application and results

The developed DD-NLD model will be first used to calculate the properties of infinite nuclear matter, both symmetric and neutron. With the new additional energy dependence of the optical potential we are able to come closer to the the experimental data than in the standard DD-RMF model. We will demonstrate how this influences the high-density EOS behavior. The several parametrizations we have developed are used to calculate the EOS of stellar matter, that is, of NS. The results are presented in the form of mass-radius diagrams.

## 6.1 Infinite nuclear matter at T = 0 MeV

In conventional RMF models without derivative couplings, the scalar and vector potentials are independent of energy and the optical potential has linear energy dependence coming from the first term in eq. (44). In figures 13 and 14 this trend can be clearly seen as a full black line for the calculation of $U_{\rm opt}$ with the parametrization D1, where no energy dependence in the self-energies is included. In the same figures the optical potentials derived from the scalar (S) and vector (V) potentials in Dirac phenomenology and using the definition (44) are given in purple color, coming from two different fits [107]. They demonstrate the uncertainty of the extracted data. These are much lower than the optical potential in a conventional DD-RMF model (D1) at high energies and they exhibit a saturation for $E_{\rm kin}$ approaching 1 GeV. By introducing the nonlinear derivative couplings in the RMF model a reasonable description of the experimental optical potential is achieved due to the energy dependence of the self-energies. In figure 13 (14) the results of the DD-NLD parametrization for the function D2 (D3) are depicted. The cut-off parameter $\Lambda$ defines the energy dependence of $U_{\rm opt}$ for the D2 and D3 cases and the values of $\Lambda$ are chosen to most closely reproduce the experimental data. There are two $\Lambda$ values for each function, in order to represent the uncertainty. The parameters are given in the table 6 for all cases. The difference between parametrization D2 and D3 is not very significant. The dependence of $U_{\rm opt}$ on the energy is stronger for D2. The deflection of the DD-NLD curve for that of the standard RMF model D1 appears at lower kinetic energies for the D3 parametrization as compared to the D2 case. In the DD-NLD model, the optical potential can be calculated easily for other baryon densities and arbitrary neutron-proton asymmetries. We will refrain from doing so, since there is no experimental data available for these general cases. The systematics with density in the linear derivative coupling model can be found in the reference [120] where a quadratic energy dependence was observed that leads to a strong reduction of the optical potential at energies above 1 GeV. This is not the case in the present DD-NLD model calculations.

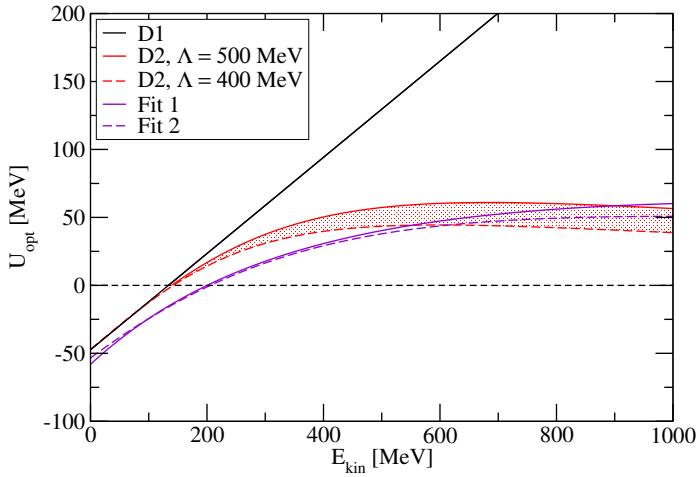


**Figure 13:** The optical potential $U_{\rm opt}$ as a function of the kinetic energy $E_{\rm kin} = E - m_{\rm nuc}$ of a nucleon in symmetric nuclear matter at saturation density in RMF models with parametrizations D1 and D2 compared to two fits from Dirac phenomenology. See text for details.

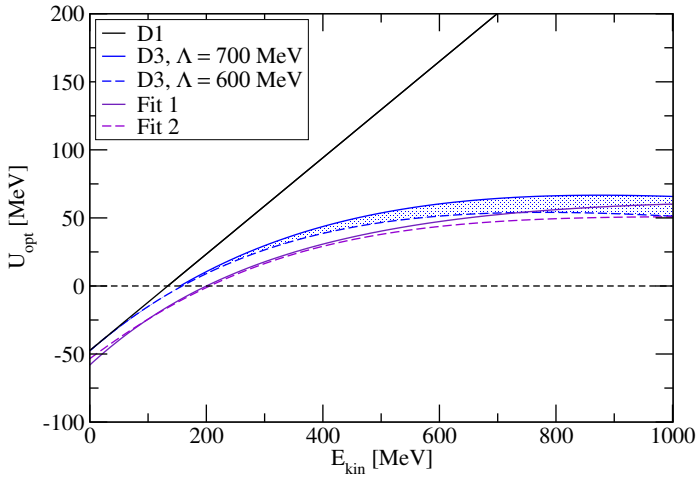


**Figure 14:** The optical potential $U_{\rm opt}$ as a function of the kinetic energy $E_{\rm kin}$ of a nucleon in symmetric nuclear matter at saturation density in RMF models with parametrizations D1 and D3 compared to two fits from Dirac phenomenology. See text for details.

Once the $U_{\rm opt}$ constraint is satisfied, and the parameters of the model are determined, we can explore how the reduction of the optical potential at high kinetic energies reflects in the EOS of nuclear matter. In figure 15 the energy per nucleon $E/A$ (without the rest mass contribution) is depicted as a function of the baryon density $n_B$ for symmetric nuclear matter (left panel) and neutron matter (right panel). For both the D2 and D3 cases, given in red and blue bands, a substantial softening of the EOS is found already at densities of 0.5 $n_0$, as compared to the standard RMF calculation with parametrization D1. The effect is stronger for an exponential energy dependence of the self-energies (D3) than for the case of a Lorentzian dependence (D2). By construction, all EoS are identical at the saturation density $n_{\rm sat}$.

When the model parameters are fitted to properties of nuclei, the function D3 was abandoned and exchanged with the d4 function as discussed earlier. The $U_{\rm opt}$ and flow constraints are taken into account and by fitting the model parameters we can get closer in reproducing their behavior expected from

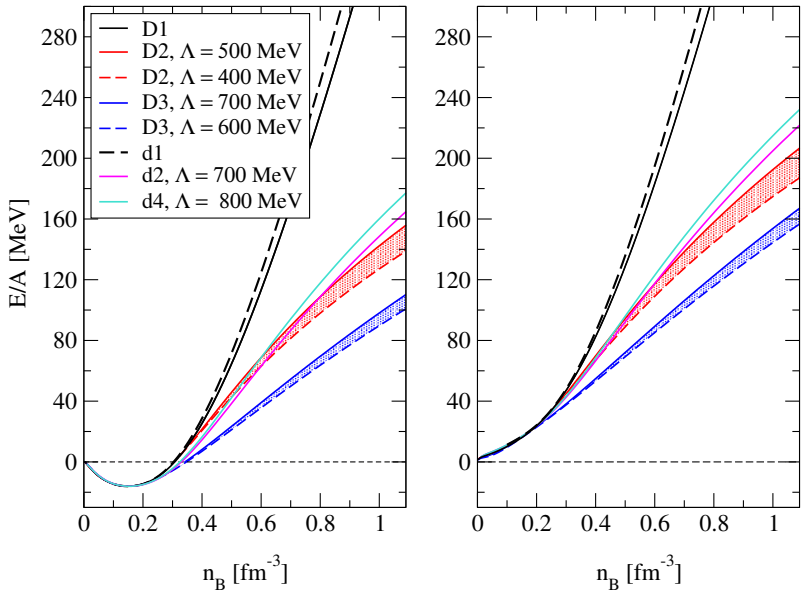


**Figure 15:** Energy per nucleon $E/A$ as a function of the baryon density $n_B$ for symmetric nuclear matter (a) and pure neutron matter (b). Results are given for three different choices of the $D$ function and different values of the cut-off parameter $\Lambda$.

experiments. In figure 16, the real part of optical potential $U_{\rm opt}$ defined through the equation (43), is given in dependence of the energy. The models presented are d1 (which is essentially the same as DD2), the d2 function (left panel) and the d4 function (right panel). The extrapolation from Dirac phenomenology is given again with full and dashed purple lines. What we can notice right away is that by fitting to nuclei it is not as easy to reproduce the optical potential behavior, especially in the middle range of energies between $200-800$ MeV.

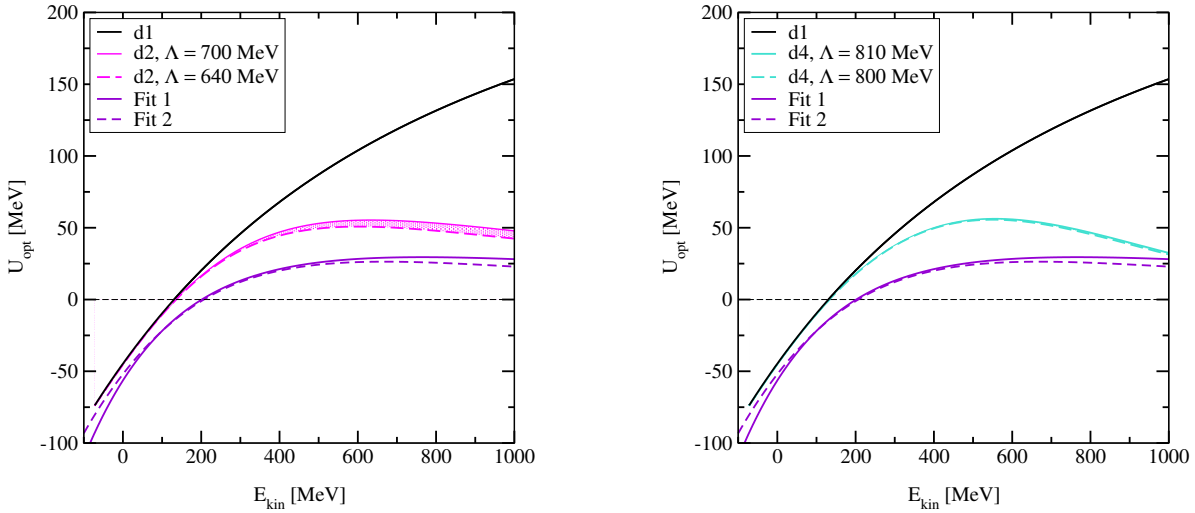


**Figure 16:** The optical potential $U_{\rm opt}$ as a function of the kinetic energy $E_{\rm kin}$ of a nucleon in SNM at saturation density in RMF models with parametrization d1, d2 (left panel) and d4 (right panel) compared to two fits from Dirac phenomenology.

The EOSs for the d2 and d4 cases are also given in figure 15, together with the D1, D2 and D3 functions. By comparison, we see that for both cases, that is for SNM (left panel) and for neutron NM (right panel), the EOS gained back some of the stiffness with a fit to nuclear properties, more in the case of d4 than d2. However, these are still rather soft EOSs which will have consequences on other properties. One of them is the maximum possible mass of a NS, examined in the next subsection.

Concerning the flow constraint from HIC, the results after the fit to nuclear properties are given in figure 17. For both of the functions d2 and d4 the EOS is passing through the required region at high

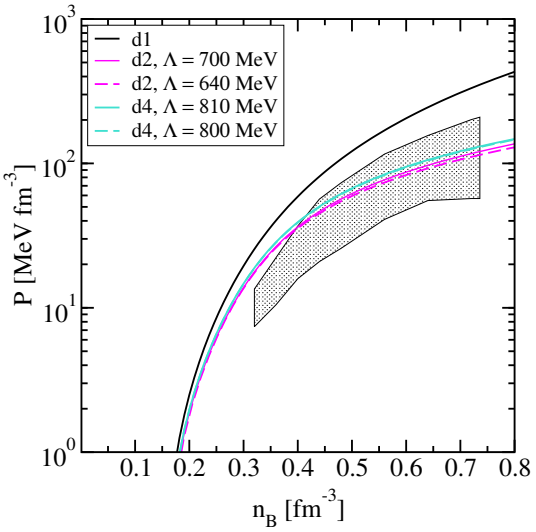


**Figure 17:** Zero-temperature EOSs d1, d2 and d4 for SNM. The shaded region correspond to the pressure and experimental flow data consistency region [111].

densities. The deviation is appearing for the region below the pressure and density we were fitting to, that is for $P \lesssim 40$ MeV and $n_B \lesssim 0.4$ fm$^{-3}$, as pointed out in the subsection 5.2. This could be improved by adding more $(P, n_B)$ points in the fit for the densities below $\sim 0.5$ fm$^{-3}$.

## 6.2 Neutron stars

The DD-NLD model can be used to predict the properties of NSs. In the present model calculations only homogeneous matter appearing in the core of a NS is treated, while the outer layers that build the crust have to be modeled separately. A suitable low-density EOS is added for this region with the idea to match the two EOSs at a certain density where the transition between the two phases, solid crust and liquid core, is expected. We choose to use the standard Baym-Pethick-Sutherland (BPS) crust EoS [81], connected to the DD-NLD EOSs at the density of around $\sim 0.05 - 0.06$ fm$^{-3}$. As already mentioned, for NS matter or stellar matter the contribution of electrons has to be added and the additional conditions on charge neutrality and $\beta$ equilibrium have to be fulfilled, as discussed in sec. 4.5. The energy density and pressure obtained through the EOS calculation for stellar matter with different parametrizations are an input for the TOV equations in order to get the masses and radii of NS. The mass-radius relations are given in figure 18 together with the masses of the two most massive pulsars observed so far. The EOSs with the D1, D2 and D3 functions and the fit to nuclear matter properties at saturation (PRMT1, table 6) are given on the left panel, while the right panel presents models with the fit to nuclear properties (PRMT2, table 8) and the d1, d2 and d4 functions.

For both cases, the model without an energy dependence (black full line) can explain without difficulties the large NS masses from astrophysical observations [71, 72] since the EoS is rather stiff at high densities (see fig. 15). In contrast, for the EoS of NS matter in the DD-NLD models that are consistent with the optical potential constraint, a serious reduction of the maximum NS mass is seen for all of the EOS cases. Starting from models with energy-dependent functions D from the left panel of figure 18, there are problems to reach even typical masses of about 1.4 $M_{\rm sol}$ of ordinary NSs. Deviations from the predictions of the standard model D1 start to appear already at masses below 0.7 $M_{\rm sol}$. The NS radius is also affected and found to be smaller for the same NS mass in the D2 and in the D3 cases of DD-NLD model. Explicit values for the maximum mass as well as the radius and central density at this extreme conditions are given in Table 9. The central densities in a star of maximum mass are considerably higher

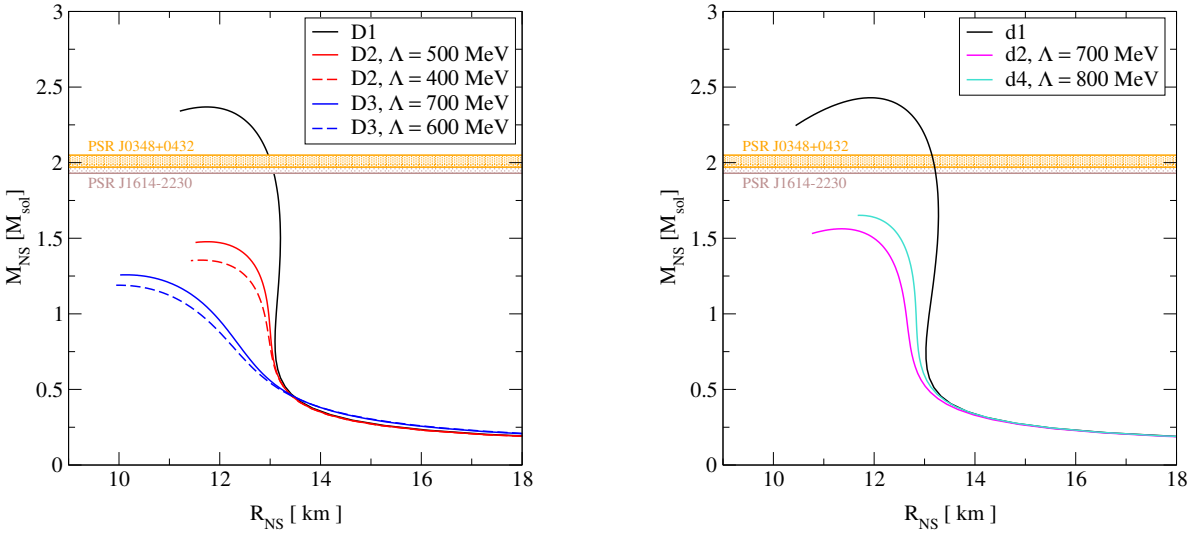


**Figure 18:** Mass-radius relation of NSs for different choices of the D (d) functions and cut-off parameters $\Lambda$ in the DD-NLD model for parametrization PRMT1 (PRMT2). The two shaded bands refer to astrophysical mass measurements of the pulsars PSR $J1614-2230$ [71] and PSR $J0348+0432$ [72].

**Table 9:** Maximum mass, corresponding radius and central density of NSs in the DD-NLD models with different choices of energy-dependent D functions for parametrization PRMT1 and d functions for PRMT2.

| Model | $M_{\max}$ [$M_{\odot}$] | $R(M_{\max})$ [km] | $n_{\text{central}}(M_{\max})$ [fm$^{-3}$] |
|---|---|---|---|
| D1 | 2.37 | 11.57 | 0.88 |
| D2, $\Lambda = 500$ MeV | 1.48 | 11.75 | 0.95 |
| D2, $\Lambda = 400$ MeV | 1.36 | 11.63 | 0.97 |
| D3, $\Lambda = 700$ MeV | 1.26 | 10.13 | 1.41 |
| D3, $\Lambda = 600$ MeV | 1.19 | 9.99 | 1.46 |
| d1 | 2.43 | 11.78 | 0.84 |
| d2, $\Lambda = 700$ MeV | 1.56 | 11.03 | 1.03 |
| d4, $\Lambda = 800$ MeV | 1.65 | 11.72 | 0.95 |

for the DD-NLD models (D2 and, in particular, D3) than for those of the standard RMF model without an energy dependence of the couplings. When the parameters are fitted to properties of finite nuclei the mass-radius relation for the d2, and d4 functions is calculated and given on the right panel of figure 18. Even though some stiffness of the EOS is regained and the NS M-R relation reaches above 1.5 $M_{\odot}$, it is obvious that these DD-NLD models are still far from reaching the two solar mass condition due to the still significantly soft EOS for high densities once the energy dependence is included in the self-energies. Explicit values for the maximum mass, radius and central density in this case are also given in table 9.

It is worthwhile to compare our results for the mass-radius relation of NSs with those of previous versions of the NLD model, where non-linear higher derivative couplings were introduced. In the approach of reference [109], with their choice of parameters, it was possible to reach a maximum NS mass of about 2 $M_{\odot}$. In contrast, the results of reference [124], which are using different functional forms of the couplings, indicate a reduction of the maximum mass below the observed values in line with our calculations. All three versions of the NLD model are adjusted to similar values of the nuclear matter parameters at saturation, such as saturation density, binding energy, compressibility or symmetry energy consistent with experimental constraints. Nevertheless, the predictions for matter properties at supra-saturation densities are rather different due to the various choices in the models to represent the effective in-medium interaction. In our work, an explicit density dependence of the couplings is considered whereas in [109] nonlinear self-couplings of the meson fields were assumed. In the approach of [124] to nuclear matter neither meson self-couplings nor a density dependence of the couplings was used. Due to the additional freedom with the explicit momentum/energy dependence in the NLD approach as compared to standard RMF models, a reasonable description of nuclear matter near saturation does not determine the high-density behavior of the EoS uniquely.

## 6.3 Finite nuclei

To study the predictions of DD-NLD model for finite nuclei the calculation of several basic nuclear properties is performed and compared to experimental data. The mass and binding energies and quantities derived from the charge formfactor are the basic nuclear quantities for nuclei since for these most of the experimental information is available. We will therefore start with the comparison of binding energies by looking into the difference between the calculated and experimental values for a range of nuclei, as in figure 19. In general, there is a good agreement of the model's predictions with the experimental values of the order of $\sim 1$ MeV. All three models showna similar pattern. It is however not possible to say that the introduction of energy dependence in the self-energies gives a better match of predicted and measured values.

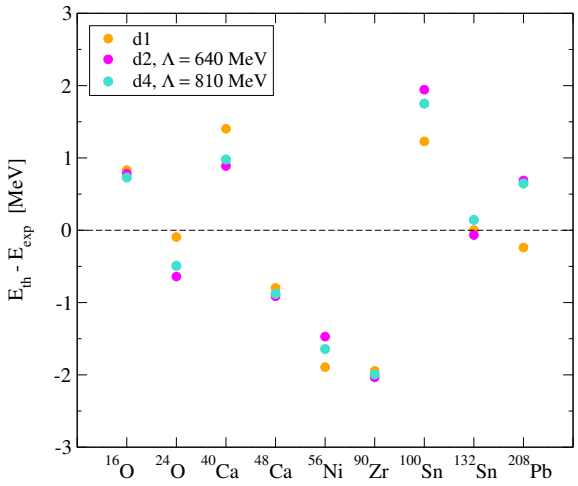


**Figure 19:** Difference between calculated and experimental binding energies for several nuclei as a function of a mass number A.

The characteristic parameters of the nuclear shape and of the charge form factor are the charge radius, diffraction radius and the surface thickness. The calculated values are compared to the experimental data (see table 7) for models with the d1, d2 and d4 function, as given in figure 20. All three models agree well with the experimental data. The difference between the models, both with and without energy dependent self-energies, is very small. They all show the same trend for the radii and the surface thickness.

The single particle energies of neutron and proton states, with the same principal quantum number and the same orbital momentum, allow a more detailed look into the description of finite nuclei. In figures 21 and 22, the theoretical single particle energies around the Fermi energies for models d1 and d2 of the nuclei $^{16}$O, $^{40}$Ca, $^{48}$Ca, $^{56}$Ni, $^{90}$Zr, $^{132}$Sn and $^{208}$Pb are compared with each other and with the experimental values extracted from appropriate one-nucleon separation energies [134] and resonance energies [135]. We note that the single-particle energies were not included in the fit but only spin-orbit splittings. From the previous calculations within the DD model we would expect that the introduction of energy dependence in self-energies would lead to compression of the single particle state spectrum, as it was the case for D$^3$C model [110] where only a linear derivative term in nucleon-meson coupling was introduced. However, from the given figures we conclude that this is not the case for the present model

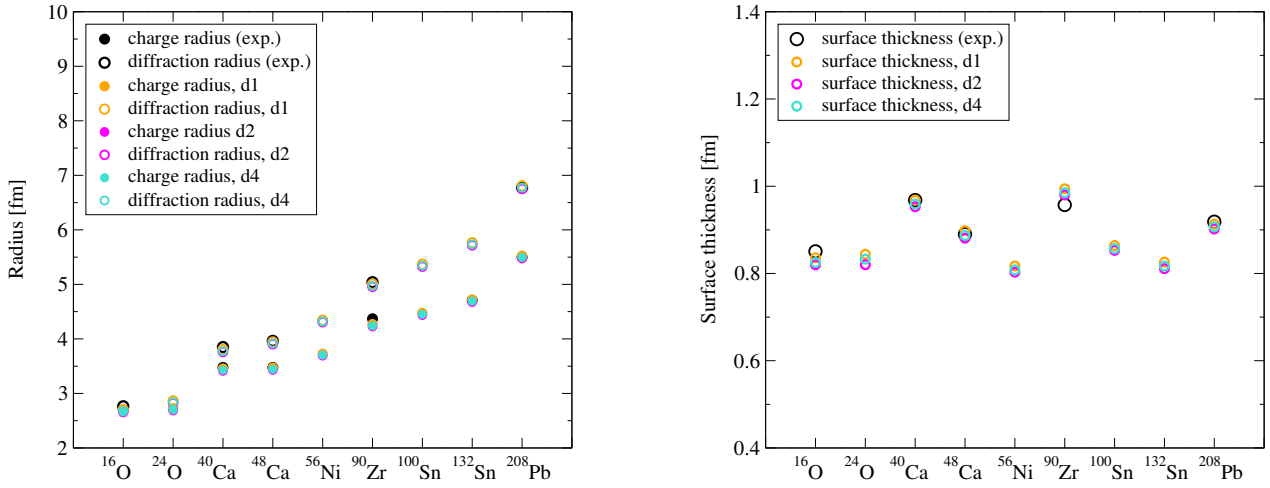


**Figure 20:** Charge radius, diffraction radius (left panel) and surface thickness (right panel) of the fit nuclei for d1, d2 and d4 models compared to the experimental data.

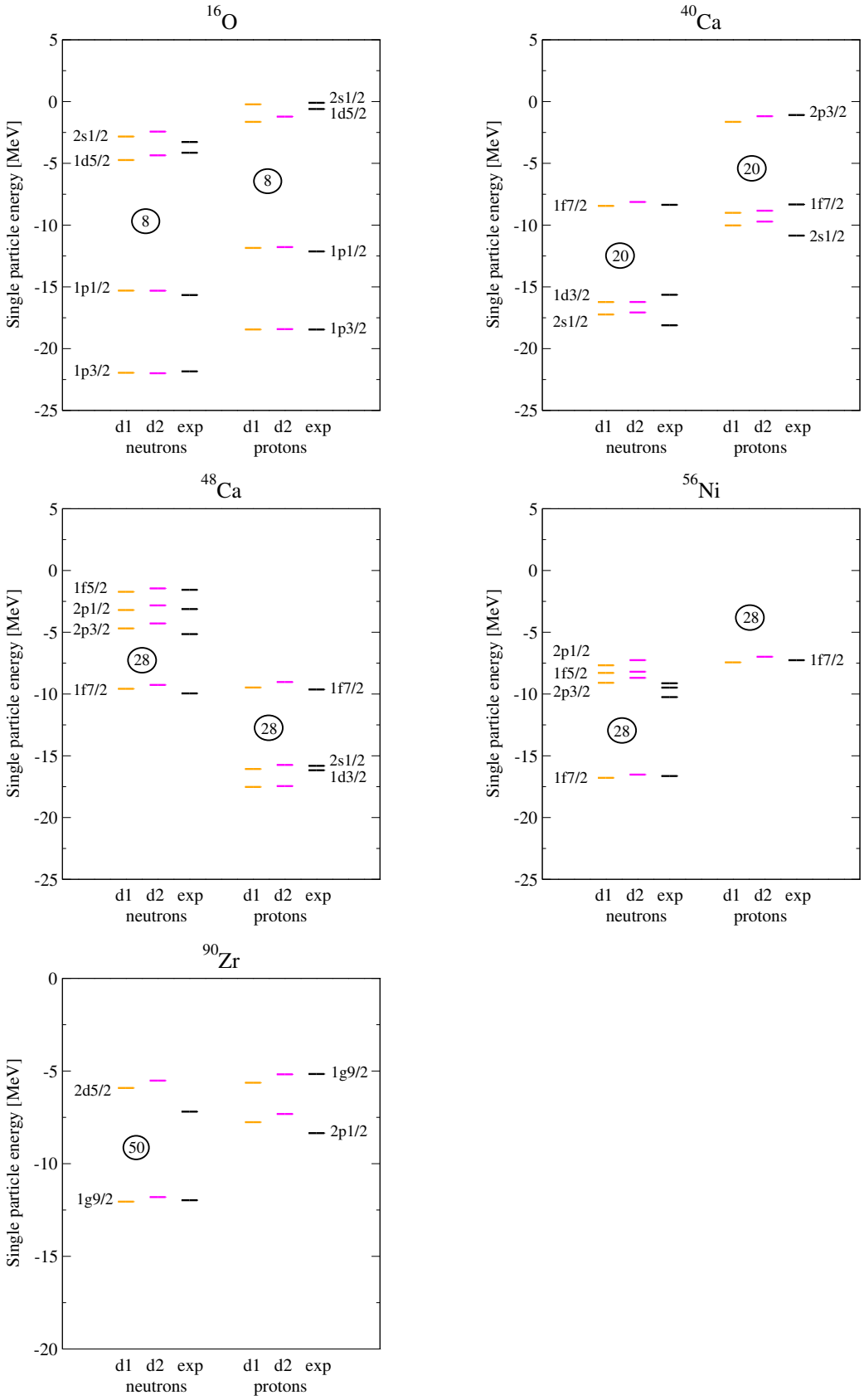


**Figure 21:** Comparison of neutron and proton single particle energies of $^{16}$O, $^{40}$Ca, $^{48}$Ca, $^{56}$Ni and $^{90}$Zr for d1 and d2 models, and experimental levels.

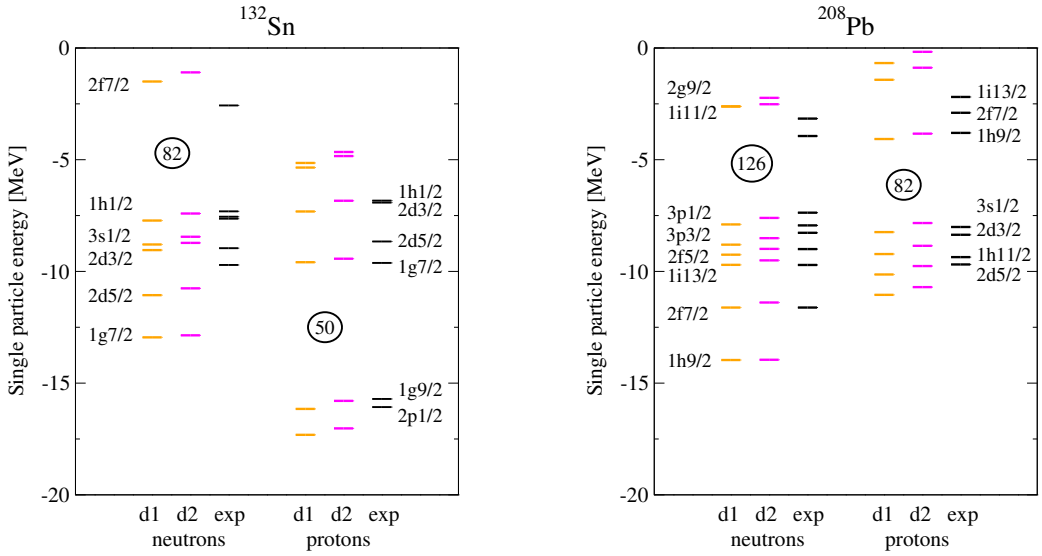


**Figure 22:** Comparison of neutron and proton single particle energies of $^{132}$Sn and $^{208}$Pb for d1 and d2 models, and experimental levels.

calculations. The difference between levels is very small when d1 and d2 models, i.e. models with and without energy dependent self-energies, are compared.

From the single-particle energies we can deduce the spin-orbit splitting between levels. The calculated values are compared to experimental data in figure 23. Again, all three theoretical predictions agree with each other and give equally good results, showing very little differences for different d functions, indicating that the introduction of energy dependence in self-energies in this way doesn't not have a noticeable effect on these properties of finite nuclei.

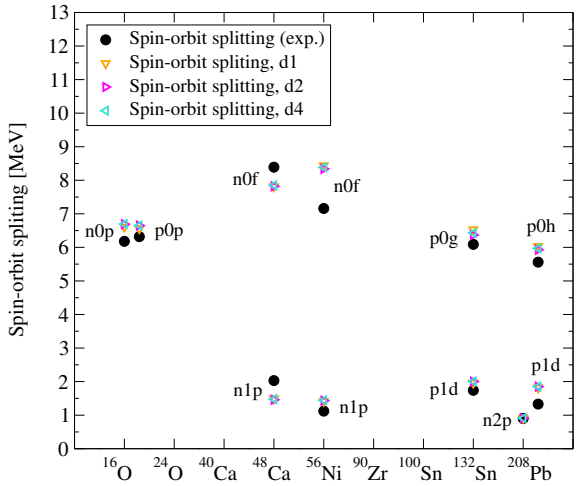


**Figure 23:** Spin-orbit splitting of neutron and proton levels for d1, d2 and d4 models compared to experiment.

# 7 Thermodynamics of uniform nuclear matter

So far we have applied the DD-NLD model only for nuclear systems at vanishing temperature, since NSs are considered to be cold systems, as already discussed in the introduction. For many other astrophysical applications however, finite temperature effects are of particular relevance, e.g. for the study of PNS cooling, to provide the EOS tables for CCSNe simulations or to describe NS mergers. For this reason, in order to have a more general model applicable to many different astrophysical sites, it is necessary to introduce a temperature dependence in the EOS calculation. Besides the temperature range, the nuclear matter density is spanning from very low densities below the saturation up to several times of the saturation density, depending on the site or object of study. As one of densest objects in the known Universe, NSs are associated with the very dense region of nuclear matter phase diagram. The DD-NLD model is originally developed with an idea to modify the EOS behavior at this high densities for $T = 0$ by introducing the energy dependent couplings, in order to check their influence on the EOS stiffness in this region, and eventually on the mass-radius relation of a NS, while satisfying the optical potential constraint.

In this chapter we will focus on the sub-saturation density region of the nuclear phase diagram and the thermal properties of uniform nuclear matter. This is an important subject on its own, regardless of the astrophysical applications. Many studies have been performed through *ab-initio* calculations of neutron matter at finite temperatures, see [136] and references therein, or studies of the nuclear liquid-gas phase transition (LGPT), see., e.g. [137, 138]), at sub-saturation densities when Coulomb and finite size effects are neglected. In general, nuclear matter undergoes different phase transitions. In the introduction we already discussed the phase transition of nucleons to a system of deconfined quarks and gluons, occurring at high temperatures and densities, known as 'QCD phase transition' or 'hadron-quark phase transition' [139, 140]. For the densities below the saturation density and temperatures up to about $\sim 15$ MeV, the nuclear matter is unstable to density fluctuations which leads to the occurrence of the LGPT mentioned above. At small temperatures matter undergoes a first-order phase transition terminating in a critical point, as shown in the lower left corner of Fig.1. This subject has been extensively studied in the literature and it is important for exploring the phase boundary, to locate the critical point and to address many important issues in nuclear astrophysics [141]. For that reason, the LGPT is also a subject of study in this chapter and will be further discussed in subsection 7.1.

Let us point out again that the study is done only for uniform nuclear matter, a theoretically idealized system that completely neglects any possible Coulomb correlations. This would naturally not be the case in real physical systems, e.g. in the low density stellar matter in $\beta$-equilibrium appearing in the outer layers of a NS, depicted in figure 4. In this case the additional presence of electrons causes the screening effect on the proton charge and charge neutrality is achieved. In contrast to nuclear matter where we expect the LGPT to occur, stellar matter at low density and zero temperature is not a gas, but a crystal of nuclei immersed in a homogeneous electron background [142, 143]. With the increase of density, in the NS inner crust, a series of geometrical structures are formed. They are not necessarily spherical and can have many different complex shapes. The origin of different shapes is due to the competition between the nuclear attraction and Coulomb repulsion forces. This leads to the replacement of the first order liquid-gas transition by a continuous transition through a clusterized medium [144], the effect which has been confirmed by different microscopic models [145]. To summarize, $\beta$-equilibrated stellar matter evolves from the Coulomb lattice to a homogeneous nuclear fluid, while passing through the formation of different size clusters and strongly deformed non-homogeneous structures close to the saturation density known also as pasta shapes, both at zero and at finite temperature. This gas/liquid-solid phase transition is relevant in the formation of the crystalline crust during the cooling of PNS [79]. The behavior of $\beta$-equilibrated stellar matter at finite temperatures is beyond the scope of this work. Another possible future application is the CCSN scenario for finite temperatures ($T < 20$ MeV) and different proton fractions, where the addition of electrons to the nuclear matter is necessary. In this case, however, npe matter is not in $\beta$-equilibrium since there is not enough time for matter to reach it. Phase

transitions could also be caused by the appearance of new particle species such as e.g. hyperons in dense hadronic matter [146, 147, 148].

The aim of this section is to investigate how the introduced energy dependent couplings in the DD-NLD model influences the low-density EOS behavior with increasing temperature. Due to this extension, a modification of the LGPT properties can be expected, in particular at high temperatures. For that reason the theoretical description has to be extended to finite temperatures which can be achieved rather straightforwardly by extending the existing code for infinite nuclear matter. This will allow us to study the properties of homogeneous nuclear matter at given temperature covering the full range of isospin asymmetries from neutron matter to symmetric and proton matter. In the following subsections we will describe more closely the nuclear matter liquid-gas phase transition in comparison to the well known phase diagram of water. The temperature dependence will be implemented in the DD-NLD model and a series of calculations for symmetric and asymmetric nuclear matter will be performed, such as the determination of the critical point and the instability and coexistence regions for the two nuclear matter phases. The results of the present approach for both d1 and d2 functionals of DD-NLD model are compared to other standard RMF models such as TW [117], NL3 [149] and DD2 [128].

## 7.1 The liquid-gas phase transition

As we already know, matter in general exists in different forms or phases. When pressure is applied to the system, the transition from one phase to another is possible, which causes the physical properties of matter to change. The study of phase transitions has been an active topic in research for a long time. Just as in the case of water, usually the most common example taken to describe different phases and transitions between them, nuclear matter also exists in different forms under different external conditions. These are given by the so-called control parameters which, in the case of water, are pressure P and temperature T. Under given pressure, water has three phases: solid (ice), liquid (water) and gaseous phase (steam). By adding heat to the system at a constant rate, the system goes from one phase to the other. The transition between two phases is marked by an abrupt, discontinuous change in some of the properties of a system. In water, two distinct transitions are observed: the ice-water and the water-gas transitions. E.g. if we take an ice-cube at 0°C and start to heat it, the ice starts to melt. However, with the additional heating, the temperature of the system does not immediately rise. Instead, we have to overcome the latent heat of melting. As long as there is still ice left, the solid and liquid phases are in coexistence. The same happens at 100°C when liquid water starts to evaporate. Liquid and gas phases are in coexistence and the temperature of the system does not rise since we have to overcome latent heat of vaporization first. This leads to plateaus in the temperature and time (or additional energy) profile, as shown in figure 24a. The transition between the two phases with a latent heat and phase coexistence is a sign of a first order phase transition. The phase diagram of water is given on figure

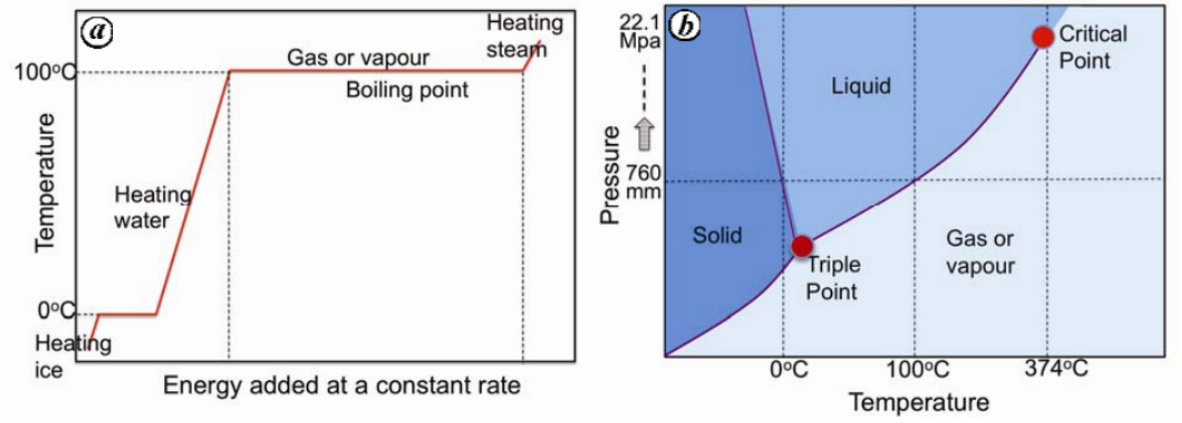


**Figure 24:** Phase diagram of water. Taken from [150].

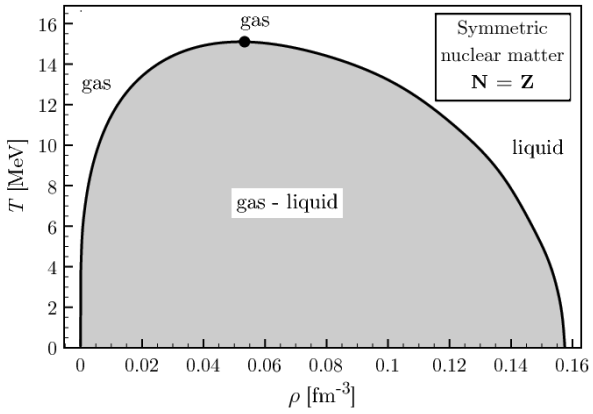


**Figure 25:** Phase diagram of isospin-symmetric nuclear matter. The critical point is indicated by the dot on the boundary of the phase coexistence region. Taken from [151].

24b, as a pressure versus temperature plot. As the temperature grows the first-order transition weakens and eventually ends up with a second order critical point. In case of water, it corresponds to the critical values of pressure ($P_C \sim 218$ atm) and temperature ($T \sim 374°$C).

The nuclear matter behavior with varying thermodynamic conditions is in analogy to the one of water. The reason is the similarity between Van der Waals forces among the molecules of water and the nucleon-nucleon interaction in nuclear matter since they both contain a long-range part, an attractive intermediate range and repulsive short-range parts. They are of similar shape regardless the fact that they have completely different strength and act on a very different length scale. Because of this similarity, already in the early days of EOS modeling it was recognized that the phase diagram of diluted nuclear matter should also give the first-order phase transition of the liquid-gas type. The sketch of nuclear matter LGPT diagram taken from the reference [151] is given in figure 25 in terms of temperature T versus the baryon density $\rho$ of the system. When the nuclear matter is heated, the temperature rises to a few MeV and the nuclear liquid starts to evaporate nucleons which makes system behave like a gas. This happens at sub-saturation densities ($\rho_{\text{sat}} < 0.16$ fm$^{-3}$) and not too high temperatures ($T < 20$ MeV). As in the case of water, until the latent heat of vaporization is overcome, the liquid and gas phases coexist, until the critical point [152] is reached. The critical temperature $T_C$ is expected to be around $T_C \sim 15$ MeV from theoretical RMF models, while somewhat higher values are indicated from experimental data [153, 154, 155, 156], generally falling above 16 MeV. This observation has been confirmed in all phenomenological [157, 158] or microscopic [128] models of symmetric and asymmetric nuclear matter with realistic effective interactions compatible with recent nuclear data.

## 7.2 Temperature dependent DD-NLD model

In the finite temperature formalism for nuclear matter the total baryon number of the system has to also include antiparticles, which means that it will be given as a number of particles minus antiparticles. The antiparticle contribution now has to be added explicitly to the formalism, contrary to the zero temperature calculations, where the vacuum was given by the Dirac sea completely filled with antiparticles. Due to thermal energy, particle-antiparticle pairs are created with a non-vanishing probability which means that a negative energy nucleon from the Dirac sea can overcome the energy gap of $2m^*$ and becomes a particle. In this way, together with the remaining hole in the Dirac sea, a nucleon-antinucleon pair is formed. The cold vacuum is now replaced by the hot vacuum which contains particle-antiparticle excitations. The corresponding particle and antiparticle occupation numbers are given by the Fermi-Dirac distribution

$$n_i = \frac{1}{1+\exp(\frac{E_i-\mu_i}{T})}, \qquad \overline{n}_i = \frac{1}{1+\exp(\frac{-E_i+\mu_i}{T})} \tag{103}$$

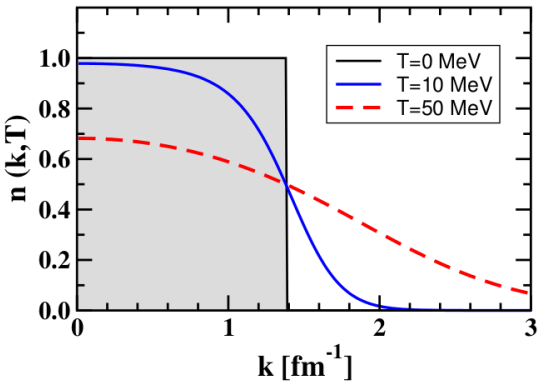


**Figure 26:** Schematic representation of the Fermi-Dirac distributions at zero and finite temperatures. Taken from [116].

where $\mu$ stands for the chemical potential, an intensive variable that is defined as the energy needed in order to add a particle to a thermally and mechanically isolated system. In natural units the Boltzmann constant $k_B$ that would stand next to the temperature is equal to 1. The Fermi-Dirac distribution for particles at zero and finite temperatures is schematically represented in figure 26.

As we mentioned in the introduction to this chapter, the temperatures of interest for this study will not exceed $\sim 20$ MeV. For such a low temperatures, the contribution of anti-nucleons in nuclear matter can be neglected since the masses of nucleons are so high that they do not have an effect at this temperatures. In the case of $\beta$-equilibrated matter when the contribution of electrons is taken into account the positrons will also contribute since the mass of both $e^-$ and $e^+$ is low compared to the temperatures. Since we are not interested in the behavior of stellar matter at finite temperatures at this point, this can be ignored since in the case of uniform nuclear matter both electrons and positrons are not present.

With that in mind, the temperature dependence in DD-NLD model is implemented in quite a simple way, through the addition of the nucleon Fermi-Dirac distribution given in the previous expression, e.g., to the nucleon density (80) (which will from now on be denoted as $\rho$)

$$\rho_i(T) = \frac{\kappa_i}{2\pi^2} \int_0^\infty \frac{p^2 dp}{1 + \exp(\frac{E_i - \mu_i}{T})} \,. \tag{104}$$

and similar for other densities (26, 81, 86), as well as in the integrals for pressure and energy density (89, 90). With this we incorporate the chemical potential $\mu$ in the integrals. For zero temperature $\mu$ was given by the Fermi energy $E_F$, while at finite temperatures it has to be chosen in a way that for a given baryon density the corresponding integral (104) yields that same density. With this, the new code provides a possibility to study the properties of homogeneous nuclear matter at given temperature covering the full range of isospin asymmetries.

## 7.3 Symmetric nuclear matter EOS and properties for finite temperatures

After the implementation of Fermi-Dirac distribution for nucleons in the DD-NLD model, the EOS is calculated for symmetric nuclear matter for a span of temperature values. It is given in terms of pressure P instead of energy per nucleon, $E/A$, which is a more common way to represent the EOS in thermodynamics, even though the two descriptions are equivalent. Figure 27 shows the evolution of the EOS at sub-saturation densities with increasing temperature for the d1 and d2 functions of the DD-NLD model using the parameters fitted to properties of nuclei from table 8. The isotherms P($\rho_B$) are shown for fixed temperature values in the range of $0-18$ MeV. The resemblance to the classical Van der Waals isotherms for the fluid-gas system is obvious. The change of the EOS with density for the $T = 0$ MeV case is explained in the following: at very low densities the system is very dilute and nucleons barely interact.

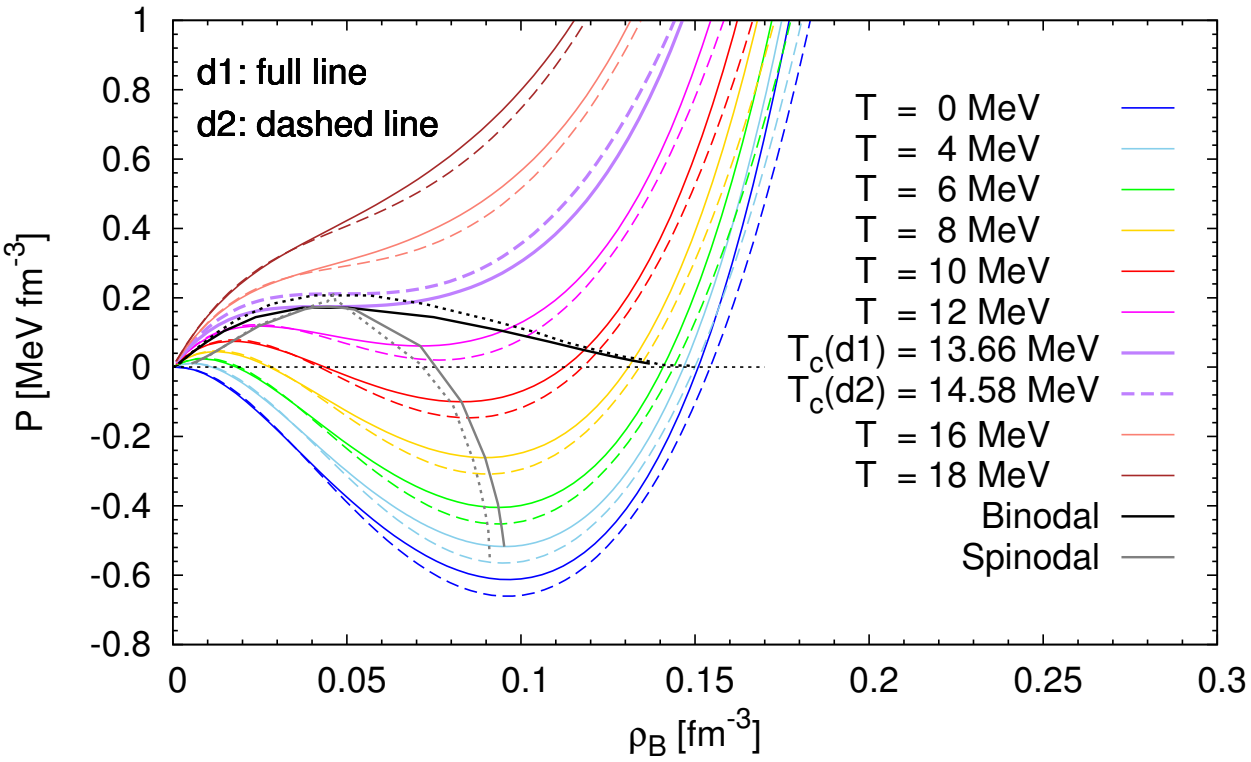


**Figure 27:** Finite temperature EOS of nuclear matter for the DD-NLD model in terms of pressure-density (P - $\rho_B$) diagram for the d1 and d2 functions. The binodal lines are given in black while the gray lines envelope spinodal regions.

Because of that, they are moving almost freely so the pressure is considered to be equivalent to the Fermi gas pressure, which is always positive. The following negative pressure part is purely due to the nuclear interactions. The pressure is negative, which means that the attractive forces among nucleons are superior and the matter wants to contract itself. As the density of nuclear matter increases, the repulsive part of nuclear interaction grows and becomes comparable to the attraction. When saturation density $n_0$ is reached the pressure has to vanish since the energy per particle is minimal at this point. For the densities beyond the saturation point the repulsive part of nucleon-nucleon interaction takes over and the matter wants to expand, resulting in the increase of pressure for nuclear matter. The slight difference between the d1 and d2 EOS is noticeable, where the energy dependent d2 function gives slightly lower pressure values than d1 for the same temperature.

The evolution of the EOS with temperature is given in the same figure. One observes a strong temperature dependence of the EOS, shifting the pressure minimum upwards as the temperature rises. Additionally to the EOSs, there are two sets of lines depicted in figure 27. The binodal lines given in black are defined through points that, for a given temperature, have different densities but same pressure and chemical potential. This means that the two phases of different densities, $\rho_1$ and $\rho_2$, are in coexistence. The second pair of lines given in gray color represents the spinodals for d1 and d2 functions. For a given T, the function $P(\rho_B)$ has two points in which the condition $\partial P/\partial \rho_B = 0$ is fulfilled. The region between them is thermodynamically unstable, characterized by $\partial P/\partial \rho_B < 0$. With the increase of temperature these two points merge and the instability region will disappear. This happens at critical temperature $T_C$ and it is defined by the conditions $\partial P/\partial \rho = 0$ and $\partial^2 P/\partial \rho^2 = 0$. For the temperatures above this value a coexistence of phases is not possible any longer and there is only one phase of homogeneous matter.

The procedure of getting binodal and spinodal points, as well as $T_C$, is given in short in the following:

- *Calculation of binodal*

  For a given T, we can have two points that share the same pressure but have different densities. Through equation (104) the baryon chemical potential for these densities can be calculated, assuming also two different values. When these two values for the chemical potential coincide, that is, when the two densities have identical intensive variables ($T$, $\mu$ and $P$), the coexistence of phases is present. An example is given in figure 28.

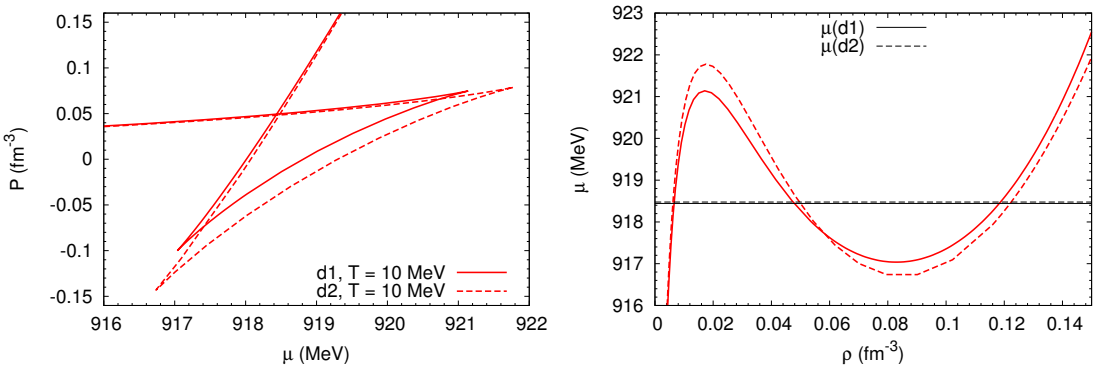


**Figure 28:** Procedure to determine the binodal points for a specific temperature (here, for $T = 10$ MeV) by finding unique values of pressure and baryon chemical potential coincident for both phases at different densities.

- *Calculation of spinodal*

  For SNM, finding the two points belonging to a spinodal curve is a simple search for maximum and minimum values of pressure for the EOS at given T. The calculation of the spinodals for asymmetric matter is explained in subsection 7.4.1.

- *Critical temperature $T_C$*

  The critical temperature in SNM is defined as the temperature for which a minimum of pressure ceases to exist and the plateau in pressure over density appears. It is the temperature above which two phases do not coexist any longer, and the pair of binodal points collapsed to a point. The procedure is to find the binodal points with identical intensive variables while increasing temperature, until we reach the $T_C$ for which only one binodal point is obtained, see figure 29.

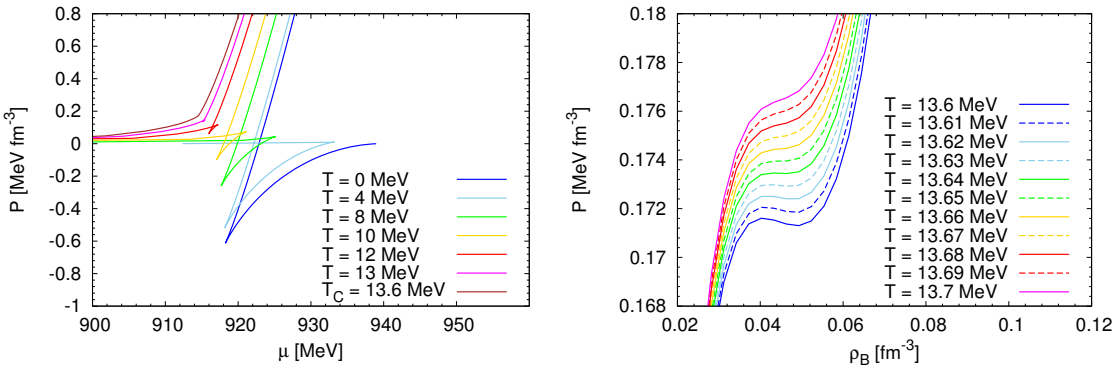


**Figure 29:** Procedure of finding the critical temperature from the disappearance of the binodal points for the d1 function as an example.

**Table 10:** Transition densities for a range of temperatures between $4-13$ MeV for d1 and d2 models of SNM calculated from binodals (table 1) and from thermodynamical spinodal (table 2).

**Binodal:**

| Model | Density [fm$^{-3}$] | T [MeV] 4 | 5 | 7 | 8 | 10 | 12 |
|---|---|---|---|---|---|---|---|
| d1 | $\rho_{t,b1}$ | 0.0001 | 0.0011 | 0.0016 | 0.0027 | 0.0066 | 0.0147 |
| | $\rho_{t,b2}$ | 0.1751 | 0.1619 | 0.1371 | 0.1321 | 0.1182 | 0.0949 |
| d2 | $\rho_{t,b1}$ | 0.0001 | 0.0010 | 0.0016 | 0.0033 | 0.0062 | 0.0129 |
| | $\rho_{t,b2}$ | 0.150 | 0.148 | 0.140 | 0.135 | 0.122 | 0.104 |

**Spinodal:**

| Model | Density [fm$^{-3}$] | T [MeV] 4 | 5 | 7 | 8 | 10 | 12 |
|---|---|---|---|---|---|---|---|
| d1 | $\rho_{t,s1}$ | 0.0054 | 0.0068 | 0.0102 | 0.0122 | 0.0172 | 0.0247 |
| | $\rho_{t,s2}$ | 0.0952 | 0.0945 | 0.0918 | 0.0897 | 0.083 | 0.0711 |
| d2 | $\rho_{t,s1}$ | 0.0065 | 0.0071 | 0.0105 | 0.0125 | 0.0174 | 0.0245 |
| | $\rho_{t,s2}$ | 0.0911 | 0.0906 | 0.081 | 0.0862 | 0.0805 | 0.0710 |

The transition densities given by the spinodal and binodal calculations for a whole range of temperatures for SNM are given in the table 10. We can notice that the instability region for the d1 case is somewhat larger then for the d2 case giving higher transition densities between the unstable and stable (coexisting and homogeneous) phases, while the larger coexistence region for d1 gives lower values for the transition density between the coexisting and homogeneous phases in comparison to the d2 model. The critical temperatures $T_C$ of d1 and d2 models are equal to is $T_C(d1) = 13.66$ MeV and $T_C(d2) = 14.58$ MeV, respectively. We notice that $T_C$ for d2 is slightly higher compared to d1 case, of about 1 MeV, moving the value closer to the other RMF model results as discussed in subsection 7.1.

## 7.4 Asymmetric nuclear matter properties for finite temperatures

In addition to the SNM calculations presented in figure 27, we will determine the spinodal and binodal regions for ANM and present them in the $(\rho_n,\ \rho_p)$ plane. The theoretical framework for the spinodal calculation is outlined and the reduction of the unstable region with increasing temperature is compared for different models. The calculation of binodals for asymmetric matter is outlined later in the chapter.

### 7.4.1 Spinodal calculation and comparison of different models

To determine the region of instability for asymmetric nuclear matter we have to fulfill the stability conditions while volume and temperature are kept constant. These are obtained from the free energy density $\mathscr{F}$, by imposing that this function is a convex function of the densities $\rho_p$ and $\rho_n$. The curvature matrix $\mathscr{C}$ of the free energy density [159, 138, 160]

$$\mathscr{C}_{ij} = \left(\frac{\partial^2 \mathscr{F}}{\partial \rho_i \partial \rho_j}\right)_T, \tag{105}$$

must be positive. If we use $\mu_i = (\partial \mathscr{F}/\partial \rho_i)|_{T,\rho_{j\neq i}}$ it follows that

$$\mathscr{C}_{ij} = \frac{\partial}{\partial \rho_j}\left(\frac{\partial \mathscr{F}}{\partial \rho_i}\right) = \frac{\partial \mu_i}{\partial \rho_j} = \begin{pmatrix} \frac{\partial \mu_p}{\partial \rho_p} & \frac{\partial \mu_p}{\partial \rho_n} \\ \frac{\partial \mu_n}{\partial \rho_p} & \frac{\partial \mu_n}{\partial \rho_n} \end{pmatrix}_T \tag{106}$$

where i and j stand both for proton and neutron. By imposing the trace and the determinant of $\mathscr{C}_{ij}$ to be positive [161],

$$\mathrm{tr}(\mathscr{C}) = \frac{\partial \mu_p}{\partial \rho_p} + \frac{\partial \mu_n}{\partial \rho_n} > 0 \tag{107}$$

$$\det(\mathscr{C}) = \frac{\partial(\mu_p, \mu_n)}{\partial(\rho_p, \rho_n)} > 0\,, \tag{108}$$

the stability conditions are fulfilled. This is equivalent to requiring that the two eigenvalues of the stability matrix, given by

$$\lambda_\pm = \frac{1}{2}\left(\mathrm{tr}(\mathscr{C}_{ij}) \pm \sqrt{\mathrm{tr}(\mathscr{C}_{ij})^2 - 4\det(\mathscr{C}_{ij})}\right), \tag{109}$$

are positive. The larger eigenvalue is always positive while the other goes to zero at the spinodal boundary and becomes negative in the instability region. To find the spinodal we are looking for the $\lambda_- = 0$ solution. By swiping through the $\rho_n$ - $\rho_p$ space, the full ANM range is covered. For each $\rho_n$ we are searching for the two matching $\rho_p$ values that will give the points in ($\rho_n$, $\rho_p$) plane for which the eigenvalue $\lambda_-$ changes sign. The two points are the lower and upper boundary of the unstable region. The eigenvectors $\delta\rho^\pm$ associated with the eigenvalues are defined as

$$\frac{\delta\rho^\pm}{\delta\rho_n^\pm} = \frac{\lambda^\pm - \frac{\partial \mu_n}{\partial \rho_n}}{\frac{\partial \mu_n}{\partial \rho_p}}\,. \tag{110}$$

The eigenvector of the $\lambda_-$ eigenvalue that defines the spinodal surface determines the instability direction, that is the direction along which the free energy decreases. Additionally, for each temperature T we can calculate the critical points, important to define the temperature below which the system is expected to be clusterized. These points will simultaneously satisfy [160]

$$\det(\mathscr{C}) = 0 \tag{111}$$

$$\det(\mathscr{M}) = 0\,, \tag{112}$$

with

$$\mathscr{M} = \begin{pmatrix} \mathscr{C}_{11} & \mathscr{C}_{12} \\ \frac{\partial|\mathscr{C}|}{\partial\rho_p} & \frac{\partial|\mathscr{C}|}{\partial\rho_n} \end{pmatrix}. \tag{113}$$

The size and shape of the spinodal region depends on the EOS model, that is on the parameters values, and on the temperature T. Previously, we have fitted our parameters to the nuclear matter properties and obtained the parameter sets for D1 and D2 functions given in Table 6. Additionally, the new parameter sets for the d1 and d2 functions were found (given in Table 8) by fitting to the selected properties of a few finite nuclei. In figure 30, we can compare the spinodal regions for the two cases. It follows that fitting to the properties of nuclei changes the spinodal region of D1 significantly, decreasing the spinodal region and transition density for a low temperature as $T = 6$ MeV, and broadening the instability area for higher temperatures, as for e.g. $T = 12$ MeV. By comparison of the D2 and d2 models, the fit to nuclei doesn't significantly change the spinodal region; the noticable effects are the slight reduction of the instability region for very asymmetric matter and low temperatures, and the increase in the $T_C$ for d2 compared to D2.

After the parameters are fitted to properties of nuclei the differences between the spinodal regions of the two functions d1 and d2 are greatly reduced compared to the D1 and D2 cases. It is however evident that the introduction of energy dependent couplings has little effect on the spinodal region for nuclear

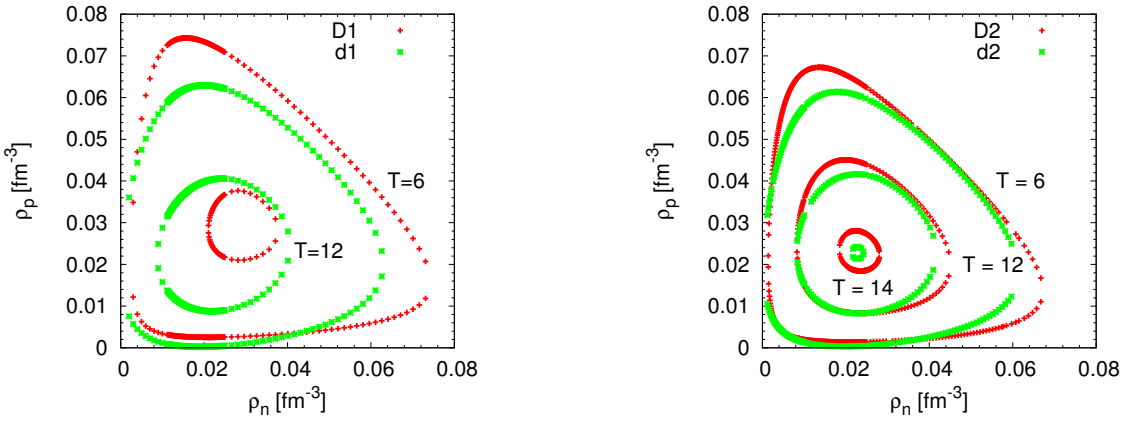


**Figure 30:** The spinodals for different parameter sets of the models with the D1(d1) and D2(d2) functions for several temperatures $T$ given in MeV.

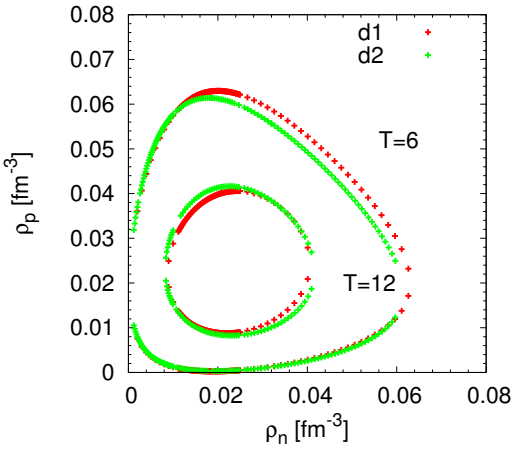


**Figure 31:** Comparison of instability regions between for the two choices of the functions (d1 and d2) of the DD-NLD model for different temperatures.

matter at such low densities and temperatures, as it can be seen on figure 31, and was already perceived from figure 27 where the spinodal lines for d1 and d2 functions are very close to each other.

The obtained results can be further compared to other RMF models, such as the TW [149] and DD2 [128] model, which also have density-dependent couplings but no energy dependence in the self-energies. The comparison is given in figure 32. The DD-NLD model gives a result close to the DD2 values with the exception of a somewhat higher critical temperature in the d2 case, which is seen from the still existing instability region for $T = 14$ MeV. The widest instability region is found for the DD-RMF model with the TW parametrization.

### 7.4.2 Binodal calculation for asymmetric matter

In order to calculate the binodal for ANM the procedure is similar as for SNM, with the exception of allowing the asymmetry of matter and baryon density to change through the calculation such that the baryon and charge chemical potentials are identical. When nuclear matter is considered at finite temperatures, from the thermodynamic point of view, the appropriate quantity to be studied is the free energy density $f(T, \rho_B, \rho_Q)$ or free energy per particle $F(T, \rho_B, \delta) = f(T, \rho_B, \rho_Q)/\rho_B$ since the temperature and

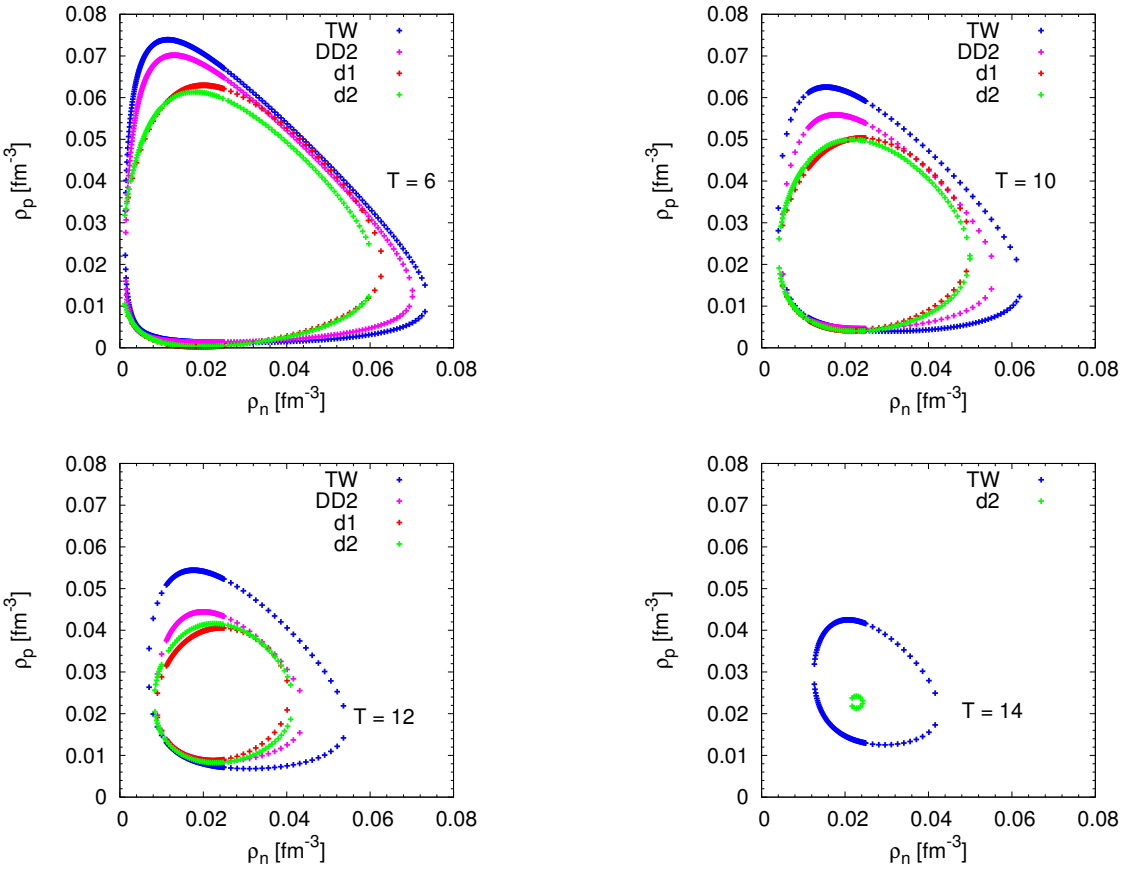


**Figure 32:** Thermodynamic instability regions for four different models TW, DD2 and DD-NLD (with d1 and d2 functions) for different temperatures ($T = 6, 10, 12, 14$ MeV).

the densities are the natural variables in this case. The quantity $\rho_Q$ stands for the total charge number density and is given by

$$\rho_Q = \frac{(1-\delta)\rho_B}{2} \tag{114}$$

for the system with $N_n = (\rho_B - \rho_Q)V$ neutrons and $N_p = \rho_Q V$ protons in a volume $V$. This allows us to express the free energy (and also the EOS, that is the energy per particle) as a function of $\rho_B$ and $\rho_Q$, or $\rho_B$ and asymmetry $\delta$, depending which is more convenient for the purpose.

In the calculation of the binodal, the charge chemical potential $\mu_Q$ will be kept fixed while we allow the asymmetry $\delta$ to change with varying baryon density $\rho_B$. We will do the calculation for a fixed temperature of $T = 10$ MeV as an example. As before, we are searching for the pairs of points with identical intensive variables, i.e. pressure

$$P^T = P\left(T, \rho_B^{(1)}, \rho_Q^{(1)}\right) = P\left(T, \rho_B^{(2)}, \rho_Q^{(2)}\right), \tag{115}$$

baryonic chemical potential

$$\mu_B^T = \mu_B\left(T, \rho_B^{(1)}, \rho_Q^{(1)}\right) = \mu_B\left(T, \rho_B^{(2)}, \rho_Q^{(2)}\right), \tag{116}$$

and charge chemical potential

$$\mu_Q^T = \mu_Q\left(T, \rho_B^{(1)}, \rho_Q^{(1)}\right) = \mu_Q\left(T, \rho_B^{(2)}, \rho_Q^{(2)}\right), \tag{117}$$

where $P^T$, $\mu_B^T$, and $\mu_Q^T$ mark the pressure and chemical potentials for the transition densities. The calculation is done for a range of $\mu_Q$ values, $\mu_Q = 0 \pm 100$ MeV, in order to cover the whole asymmetry space from $\delta = -1$ (proton matter) to $+1$ (neutron matter). The final binodals for d1 and d2 models are given in the ($\delta$, $\rho_B$) diagram on the left panel of figure 33, where the lines for constant values of $\mu_Q$ are presented with the dashed black lines. The phases in coexistance enveloped by the binodal have different densities and different asymmetries: the phase with high $\rho_B$ has low asymmetry $|\delta|$ while the phase of low $\rho_B$ has high asymmetry $|\delta|$.

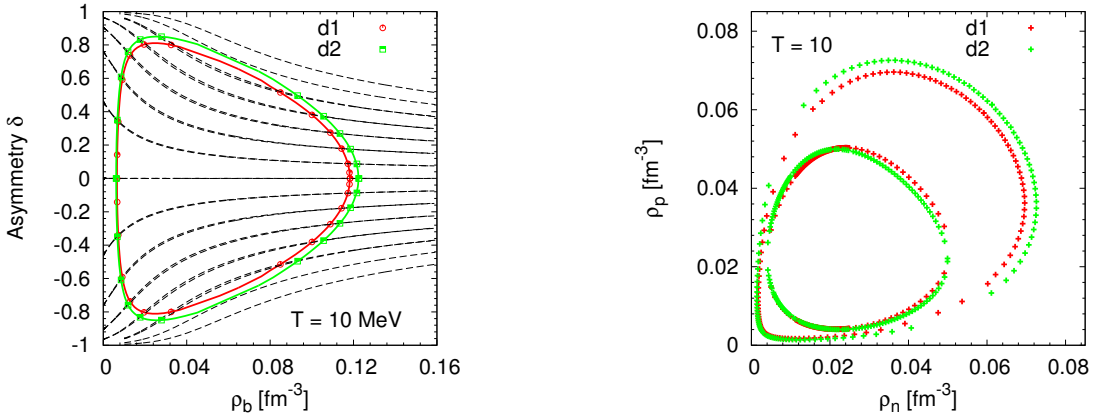


**Figure 33:** Binodals for d1 and d2 functions for $T = 10$ MeV are represented in ($\delta$; $\rho_B$) space on the left panel. Dashed lines correspond to constant charge chemical potentials $\mu_Q$. The right panel shows the binodal regions for the d1 and d2 functions enveloping the spinodals in the ($\rho_n$, $\rho_p$) plane.

The result can be transformed into the ($\rho_n$, $\rho_p$) space by using

$$\rho_p = (1-\delta)\frac{\rho_b}{2} \tag{118}$$

$$\rho_n = (1+\delta)\frac{\rho_b}{2}, \tag{119}$$

where $\delta$ is the asymmetry, given by $\delta = (\rho_n - \rho_p)/\rho_B$. The calculated binodals are presented The unstable region (inside spinodal) is enclosed within the coexistence region (inside binodal) for both cases. The d2 case shows a somewhat larger area of coexistence compared to d1, but the two are in general enclosing a similar area.

Furthermore, the critical points, common for both spinodal and binodals, can be calculated. Figure 34 presents critical points at several temperatures for the d2 function of DD-NLD model.

## 7.5 Instability region for different proton fractions

For ANM, the EOS depends on the proton fraction of the system (see figure 35). SNM with $Y_p = 0.5$ has the minimum in pressure which, with the reduction of proton fraction and at constant temperature, evolves up to a certain $Y_p$ for which it ceases to exist.

The change of proton fraction $Y_p$ changes the EOS, which leads to changes in the transition densities between the stable and unstable regions of nuclear matter, as well as the transition densities to homogeneous matter. The transition densities of SNM were already given in table 10. These are easily extracted from the left panel of figure 36, where the spinodals for the d2 function are plotted for several different temperatures and the transition densities are determined as the densities at which the EOS of SNM crosses the spinodal boundary. If we allow proton fraction to change, starting from SNM value of

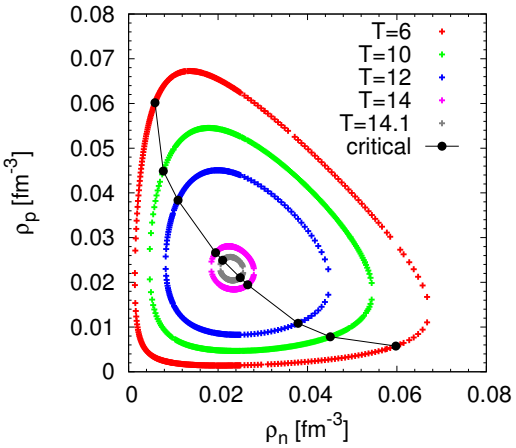


**Figure 34:** Critical points for the d2 function of the DD-NLD model for several different temperatures ($T = 6, 10, 12, 14$ MeV).

$Y_p = 0.5$ toward neutron matter with $Y_p = 0$, the EOS is shifting towards neutron rich matter, as seen on the right panel of figure 36. For a specific value of $Y_p$ the instability region will disappear, that is, the EOS will not intersect with the given spinodal, which means that in a very neutron rich environment (of certain $Y_p$) it is not possible to have two different phases in coexistence. From figure (36) it is evident that, in the case of $T = 10$ MeV and for d2 function, the critical value of $Y_p$ lies between $0.1 < Y_p < 0.2$.

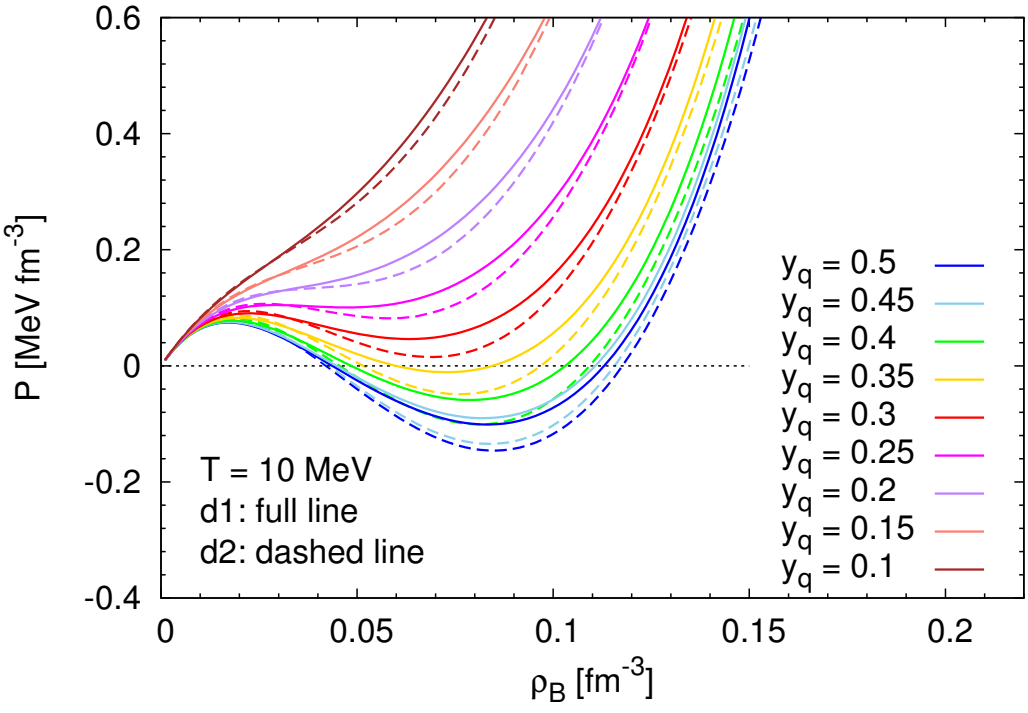


**Figure 35:** EOSs for different proton fractions for the d2 function and $T = 10$ MeV.

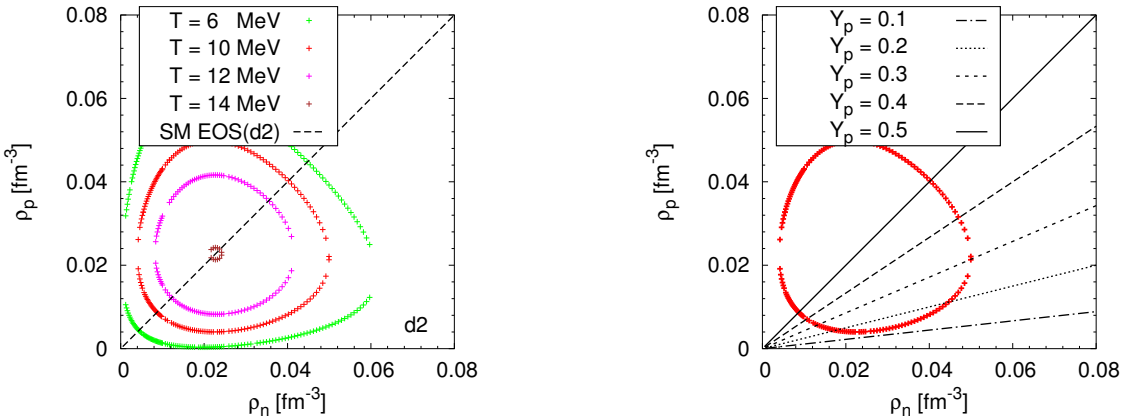


**Figure 36:** Crossing of the d2 EOS for SM with spinodals of different temperatures (left). Crossing of the EOS with different $Y_p$ with the spinodal region for d2 and $T = 10$ MeV (right).

# 8 Conclusions

In this work the conventional RMF model was extended by including non-linear derivatives (NLD) in the nucleon-meson couplings, in addition to the already existing density-dependence (DD). As a consequence, the scalar and vector self-energies in the Dirac equation for nucleons obtain an energy/momentum dependence. The importance of this is obvious once we look at the optical potential of symmetric matter. The experimental data from elastic proton scattering on nuclei of different mass number $A$ imply that the optical potential saturates at high kinetic energies, in difference to standard RMF models that predict a linear increase with energy. The extension we introduced allows to fit the optical potential of the model to experimental data and to reproduce the saturation for energies up to 1 GeV. Save the satisfying optical potential constraint, the energy/momentum dependence of nucleon self-energies is, in general, expected, e.g., from Dirac-Brueckner calculations of nuclear matter, or in simulations of heavy-ion collisions through the use of relativistic transport approaches. An energy/momentum dependence of the effective in-medium interaction is mandatory for a proper description and analysis of these experimental data.

There are already particular extensions of the RMF model with explicit energy or momentum dependencies in the nucleon self-energies, both for DD and NLD models. In the DD approach, linear derivatives of the nucleon fields were considered [120] (DC1, DC2, DC3 models) with an application to uniform nuclear matter, and later, with the introduction of density-dependent couplings [110], the model was successfully applied to finite nuclei ($D^3C$ model). The couplings to all orders in the derivative of nucleons were introduced in the NLD approach [121, 122], first applied for isospin symmetric and asymmetric nuclear matter and without a density dependence or self-couplings of the mesons, and later with the added self-couplings of mesons and generalized NLD couplings of any functional form [109]. The latter was applied to NSs yielding a maximum NS mass over 2 $M_\odot$. This result was also a motivation to test if the introduction of NLD terms will yield high enough NS masses in the case of RMF models with density dependent couplings.

After developing an extended DD-NLD model two parametrizations are introduced: one is a fit to properties of nuclear matter at saturation density while the other includes a fit to properties of several finite nuclei. The different choices of the energy dependent function (D1, D2, D3, d1, d2 and d4) and parametrisation (PRMT1, PRMT2) define different EOSs. The application and results are divided in two main parts. The first part concerns the application to zero temperature systems, infinite symmetric nuclear matter and NSs. In the application to infinite symmetric nuclear matter and pure neutron matter we observe a serious softening of the EOS at high densities, for all of the energy dependent function choices used in this work, both for parameters fitted to nuclear matter properties and with the a to properties of nuclei. This effect is independent of the appearance of additional degrees of freedom, such as hyperons or deltas, and comes purely from the energy dependence appearing in the self-energies and the reproduction of the experimental optical potential behavior. As a result, it becomes very difficult to obtain very massive NSs consistent with the observational constraints. However, in the present work only a few choices of the energy dependence were tested so a substantial freedom in the model remains. Nevertheless, the result of this study indicates that the optical potential constraint has to be taken seriously into account in the development of realistic phenomenological models of dense matter.

To examine the influence of the implemented energy dependence in the nucleon self-energies on the properties of finite nuclei, the calculation of several basic nuclear quantities was performed: binding energies, charge and diffraction radii, surface thicknesses, single-particle energies and spin-orbit splittings. The results were compared to the conventional model with no energy dependence in the self-energies and in addition to the available experimental data. Contrary to the expectations, no significant difference was noticed once the energy dependence is implemented in the nucleon self-energies in comparison to the standard version of the DD-RMF model. The results of all three models, d1, d2 and d4 gave very similar values, and the expected compression of the single-particle energy spectra was not observed. With this we can conclude that NLD extension of the DD model doesn't significantly influence the properties

of finite nuclei. The main contribution is the reasonable description of the optical potential constraint while keeping the other results on a same quality of agreement as the conventional DD-RMF model.

The second part of this work examined the thermodynamics of nuclear matter, both symmetric and antisymmetric, for low temperatures ($T < 20$ MeV) and subsaturation densities. Under these conditions nuclear matter is unstable to density fluctuations, which leads to the occurrence of a liquid-gas phase transition. We wanted to characterize the properties of the liquid-gas phase transition in the present approach in comparison to standard RMF descriptions. In the examination of spinodals and binodals for different temperatures, we found that the d2 EOS that includes energy dependent self-energies gives very similar result as the energy independent d1 function, with very slight difference in the instability and coexistence regions. Due to the energy dependence of the nucleon self-energies in the DD-NLD model, a modification of properties of the liquid-gas phase transition can be expected in particular at high temperatures. The outcome is the increase of the critical temperature for the d2 function with energy dependence in comparison to the d1 function, moving it closer to the results from other RMF models and experiments, that is, towards a higher value. Since the extension to energy dependent self-energies was introduced mainly to take care of the high density part of the EOS, in order to provide the saturation of the optical potential, it is not a surprise that there is little effect on the EOS at subsaturation densities and not too high temperatures.

In conclusion, the developed model is very flexible and can be extended to be applied for different purposes. One possible scenario is to use it in the study of CCSN matter for finite temperatures ($T < 20$ MeV) and fixed proton fractions, since such a collapse happens in order of a second timescale and there is no time for matter to reach $\beta$ equilibrium. Another possibility is to use it in HIC simulations where RMF models with self-energies explicitly dependent on the nucleon energy/momentum can be applied using relativistic transport approaches. The EOS could then be tested at supra-saturation densities. It is well known that an energy/momentum dependence of the effective in-medium interaction is mandatory for a proper description and analysis of experimental data from HICs. Such an approach can help to constrain the parameters of the present model at densities that are not accessible in the description of finite nuclei.

# A Optical potential

The optical potential (43) is derived starting from the in-medium dispersion relation

$$p_i^{*\mu} p^*_{i\mu} = \left(m_i^*\right)^2 \tag{A.1}$$

or

$$\left(p_i^\mu - \Sigma_i^\mu\right)\left(p_{i\mu} - \Sigma_{i\mu}\right) = (m_i - \Sigma_i)^2 \ . \tag{A.2}$$

By considering only the zero component of the vector self-energy we obtain

$$p_i^2 = (E_i - \Sigma_i^0)^2 - (m_i - \Sigma_i)^2 \ . \tag{A.3}$$

In free space the dispersion relation is equal to

$$E_i^{\text{free}} = \sqrt{p_i^2 + m_i^2}$$

and the optical potential is given as a difference between the two energies

$$U_{\text{i,opt}} = E_i - E_i^{\text{free}} \tag{A.4}$$

where $p_i$ is given by (A.3). It follows that the difference yields the expression for optical potential

$$\begin{aligned} U_{\text{i,opt}}(E_i) &= E_i - \sqrt{p_i^2 + m_i^2} \\ &= E_i - \sqrt{(E_i - \Sigma_i^0)^2 + \Sigma_i\,(2m_i - \Sigma_i)} \end{aligned} \tag{A.5}$$

with the expression for the momentum (A.3).

# B DD-NLD model

## B.1 Interaction Lagrangian

For the simplicity we will derive the interaction Lagrangian only for $\sigma$ and $\omega$ mesons. The same procedure can be applied for $\rho$ mesons.

Starting from the standard RMF model, the interaction Lagrangian for $\sigma$ and $\omega$ mesons is given by

$$\mathscr{L}_{\rm int} = \Gamma_\sigma \sigma \overline{\Psi}\Psi - \Gamma_\omega \omega_\mu \overline{\Psi}\gamma^\mu \Psi \,. \tag{B.1}$$

We are introducing the higher order derivative terms of nucleon-meson coupling in the interaction as

$$\begin{aligned}
\mathscr{L}^\sigma_{int} &= \Gamma_\sigma\Big[\overline{\Psi}\Big(d^{(0)} + \frac{1}{1!}d^{(1)}(-v^{\beta_1}\overleftarrow{\partial_{\beta_1}} - sm) + \frac{1}{2!}d^{(2)}(-v^{\beta_1}\overleftarrow{\partial_{\beta_1}} - sm)(-v^{\beta_2}\overleftarrow{\partial_{\beta_2}} - sm) + \dots \\
&+ \frac{1}{n!}d^{(n)}(-v^{\beta_1}\overleftarrow{\partial_{\beta_1}} - sm)\cdots(-v^{\beta_n}\overleftarrow{\partial_{\beta_n}} - sm)\Big)\Psi\sigma \\
&+ \sigma\overline{\Psi}\Big(d^{(0)} + \frac{1}{1!}d^{(1)}(v^{\beta_1}\overrightarrow{\partial_{\beta_1}} - sm) + \frac{1}{2!}d^{(2)}(v^{\beta_1}\overrightarrow{\partial_{\beta_1}} - sm)(v^{\beta_2}\overrightarrow{\partial_{\beta_2}} - sm) + \dots \\
&+ \frac{1}{n!}d^{(n)}(v^{\beta_1}\overrightarrow{\partial_{\beta_1}} - sm)\cdots(v^{\beta_n}\overrightarrow{\partial_{\beta_n}} - sm)\Big)\Psi\Big]
\end{aligned} \tag{B.2}$$

$$\begin{aligned}
\mathscr{L}^\omega_{int} &= -\Gamma_\omega\Big[\overline{\Psi}\Big(d^{(0)} + \frac{1}{1!}d^{(1)}(-v^{\beta_1}\overleftarrow{\partial_{\beta_1}} - sm) + \frac{1}{2!}d^{(2)}(-v^{\beta_1}\overleftarrow{\partial_{\beta_1}} - sm)(-v^{\beta_2}\overleftarrow{\partial_{\beta_2}} - sm) + \dots \\
&+ \frac{1}{n!}d^{(n)}(-v^{\beta_1}\overleftarrow{\partial_{\beta_1}} - sm)\cdots(-v^{\beta_n}\overleftarrow{\partial_{\beta_n}} - sm)\Big)\gamma^\mu\Psi\omega_\mu \\
&+ \omega_\mu\overline{\Psi}\gamma^\mu\Big(d^{(0)} + \frac{1}{1!}d^{(1)}(v^{\beta_1}\overrightarrow{\partial_{\beta_1}} - sm) + \frac{1}{2!}d^{(2)}(v^{\beta_1}\overrightarrow{\partial_{\beta_1}} - sm)(v^{\beta_2}\overrightarrow{\partial_{\beta_2}} - sm) + \dots \\
&+ \frac{1}{n!}d^{(n)}(v^{\beta_1}\overrightarrow{\partial_{\beta_1}} - sm)\cdots(v^{\beta_n}\overrightarrow{\partial_{\beta_n}} - sm)\Big)\Psi\Big]
\end{aligned} \tag{B.3}$$

We can rewrite the derivative terms as a sum and and write is as an opearator $\overrightarrow{D}$ of the form

$$\begin{aligned}
\overrightarrow{D} &= \sum_{n=0}^{\infty}\frac{1}{n!}d^{(n)}\sum_{k=0}^{n}\binom{n}{k}(-sm)^{n-k}(v^\beta i\partial_\beta)^k \\
&= \sum_{k=0}^{n}\Big[\sum_{n=k}^{\infty}\frac{1}{n!}d^{(n)}\binom{n}{k}(-sm)^{n-k}\Big](v^\beta i\partial_\beta)^k \\
&= \sum_{k=0}^{\infty}C_k(v^\beta i\partial_\beta)^k
\end{aligned} \tag{B.4}$$

where $C_k$ is

$$C_k = \sum_{n}^{k}\frac{1}{n!}d^{(n)}\binom{n}{k}(-sm)^{n-k}\,. \tag{B.5}$$

From here the interaction Lagrangians for $\sigma$ and $\omega$ can be written as

$$\begin{aligned}
\mathscr{L}^\sigma_{int} &= \Gamma_\sigma\Big[\overline{\Psi}\sum_{k=0}^{n}C_k(-v^\beta i\overleftarrow{\partial_\beta})^k\Psi\sigma + \sigma\overline{\Psi}\sum_{k=0}^{n}C_k(v^\beta i\overrightarrow{\partial_\beta})^k\Psi\Big] \\
\mathscr{L}^\omega_{int} &= -\Gamma_\omega\Big[\overline{\Psi}\sum_{k=0}^{n}C_k(-v^\beta i\overleftarrow{\partial_\beta})^k\gamma^\mu\Psi\omega_\mu + \omega_\mu\overline{\Psi}\gamma^\mu\sum_{k=0}^{n}C_k(v^\beta i\overrightarrow{\partial_\beta})^k\Psi\Big],
\end{aligned} \tag{B.6}$$

that is as

$$\begin{aligned}\mathscr{L}^{\sigma}_{int} &= \Gamma_\sigma\Big[\overline{\Psi}\overleftarrow{D}_\sigma\Psi\sigma+\sigma\overline{\Psi}\overrightarrow{D}_\sigma\Psi\Big]\\ \mathscr{L}^{\omega}_{int} &= -\Gamma_\omega\Big[\overline{\Psi}\overleftarrow{D}_\omega\Psi\omega_\mu+\omega_\mu\overline{\Psi}\overrightarrow{D}_\omega\Psi\Big].\end{aligned} \tag{B.7}$$

## B.2 Derivation of Dirac equation

To derive the Dirac equation we start from the generalized Euler-Lagrange equation (54) and find the derivatives of the Lagrangian regarding the nucleon field. The Lagrangian is of the form

$$\begin{aligned}\mathscr{L} &= \frac{1}{2}\Big[\overline{\Psi}(-\gamma^\mu i\overleftarrow{\partial_\mu}-m)\Psi+\overline{\Psi}(\gamma^\mu i\overrightarrow{\partial_\mu}-m)\Psi\Big]+\mathscr{L}_m\\ &+\frac{1}{2}\Big[\overline{\Psi}\sum_{k=0}^{n}C_k(-v^\beta i\overleftarrow{\partial_\beta})^k(-\gamma^\mu\Gamma_\omega\omega_\mu+\Gamma_\sigma\sigma)\Psi\\ &+\overline{\Psi}(-\gamma^\mu\Gamma_\omega\omega_\mu+\Gamma_\sigma\sigma)\sum_{k=0}^{n}C_k(v^\beta i\overrightarrow{\partial_\beta})^k\Psi\Big]\end{aligned} \tag{B.8}$$

We need to use the generalized Euler-Lagrange equation

$$\frac{\partial\mathscr{L}}{\partial\varphi_r}+\sum_{i=1}^{\infty}(-)^i\partial_{\alpha_1,\ldots,\alpha_i}\frac{\partial\mathscr{L}}{\partial(\partial_{\alpha_1,\ldots,\alpha_i}\varphi_r)}=0\,. \tag{B.9}$$

Let us find the necessary derivations for Euler-Lagrange equation

$$\begin{aligned}\frac{\partial\mathscr{L}}{\partial\overline{\Psi}} &= \frac{1}{2}\Big[-m+(\gamma^\mu i\overrightarrow{\partial_\mu}-m)+C_0(-\gamma^\mu\Gamma_\omega\omega_\mu+\Gamma_\sigma\sigma)+(-\gamma^\mu\Gamma_\omega\omega_\mu+\Gamma_\sigma\sigma)\sum_{k=0}^{n}C_k(v^\beta i\overrightarrow{\partial_\beta})^k\Big]\Psi\\ \frac{\partial\mathscr{L}}{\partial(\partial_{\alpha_1}\overline{\Psi})} &= \frac{1}{2}\Big[(-\gamma^{\alpha_1}i)+(C_1(-v^{\alpha_1}i)(-\gamma^\mu\Gamma_\omega\omega_\mu+\Gamma_\sigma\sigma)\Big]\Psi\\ \frac{\partial\mathscr{L}}{\partial(\partial_{\alpha_1,\alpha_2}\overline{\Psi})} &= \frac{1}{2}\Big[C_2(-v^{\alpha_1}i)(-v^{\alpha_2}i)(-\gamma^\mu\Gamma_\omega\omega_\mu+\Gamma_\sigma\sigma)\Big]\Psi\\ \frac{\partial\mathscr{L}}{\partial(\partial_{\alpha_1,\alpha_2,\alpha_3}\overline{\Psi})} &= \frac{1}{2}\Big[C_3(-v^{\alpha_1}i)(-v^{\alpha_2}i)(-v^{\alpha_3}i)(-\gamma^\mu\Gamma_\omega\omega_\mu+\Gamma_\sigma\sigma)\Big]\Psi\\ &\vdots\\ \frac{\partial\mathscr{L}}{\partial(\partial_{\alpha_1,\ldots\alpha_i}\overline{\Psi})} &= \frac{1}{2}\Big[C_n(-v^{\alpha_1}i)\ldots(v^{\alpha_n}i)(-\gamma^\mu\Gamma_\omega\omega_\mu+\Gamma_\sigma\sigma)\Big]\Psi\,.\end{aligned}$$

For the equation of motion up to first order in the index $i$ we obtain

$$\begin{aligned}&\frac{1}{2}(\gamma^\mu i\overrightarrow{\partial_\mu}-m)+\frac{1}{2}(\gamma^{\alpha_1}i\partial_{\alpha_1}-m)+\frac{1}{2}(-\gamma^\mu)\Gamma_\omega\Big(C_0\omega_\mu+C_1(v^{\alpha_1}i\partial_{\alpha_1})\omega_\mu+\omega_\mu\sum_{k=0}^{n}C_k(v^\beta i\overrightarrow{\partial_\beta})^k\Big)\\ &+\frac{1}{2}\Gamma_\sigma\Big(C_0\sigma+C_1(v^{\alpha_1}i\partial_{\alpha_1})\sigma+\sigma\sum_{k=0}^{n}C_k(v^\beta i\overrightarrow{\partial_\beta})^k\Big)=0\,.\end{aligned}$$

The equation of motion up to n-th order is then

$$\begin{aligned}&\Big[\frac{1}{2}(\gamma^\mu i\overrightarrow{\partial_\mu}-m)+\frac{1}{2}(\gamma^{\alpha_1}i\partial_{\alpha_1}-m)+\frac{1}{2}(-\gamma^\mu)\Gamma_\omega\Big(\sum_{k=0}^{n}C_k(v^\alpha i\overrightarrow{\partial_\alpha})^k\omega_\mu+\omega_\mu\sum_{k=0}^{n}C_k(v^\beta i\overrightarrow{\partial_\beta})^k\Big)+\\ &\frac{1}{2}\Gamma_\sigma\Big(\sum_{k=0}^{n}C_k(v^\alpha i\overrightarrow{\partial_\alpha})^k\sigma+\sigma\sum_{k=0}^{n}C_k(v^\beta i\overrightarrow{\partial_\beta})^k\Big)\Big]\Psi=0\,.\end{aligned}$$

The Dirac equation follows as

$$\gamma^\mu i\partial_\mu\Psi - m\Psi - \frac{1}{2}\gamma^\mu\Gamma_\omega(\overrightarrow{D}\,\omega_\mu + \omega_\mu\overrightarrow{D})\Psi + \frac{1}{2}\Gamma_\sigma(\overrightarrow{D}\,\sigma + \sigma\overrightarrow{D})\Psi = 0 \tag{B.10}$$

or

$$\gamma^\mu(i\partial_\mu - \Sigma_\mu)\Psi - (m - \Sigma)\Psi = 0 \tag{B.11}$$

where $\Sigma_\mu = \frac{1}{2}\Gamma_\omega\left(\overrightarrow{D}\,\omega_\mu + \omega_\mu\overrightarrow{D}\right)$ and $\Sigma = \frac{1}{2}\Gamma_\sigma\left(\overrightarrow{D}\,\sigma + \sigma\overrightarrow{D}\right)$ are vector and scalar self-energies, in case when no $\rho$ meson is taken into account. The same procedure would be applied when $\rho$ is included.

## B.3 Derivation of meson field equations

As we said, for mesons we use the standard Euler-Lagrange equation

$$\frac{\partial\mathscr{L}}{\partial\varphi_r} - \partial_\alpha\frac{\partial\mathscr{L}}{\partial(\partial_\alpha\varphi_r)} = 0 \tag{B.12}$$

because only first derivatives of the meson fields appear in the Lagrangian density. The equations of motion are calculated as follows:

- For the $\sigma$ meson:

$$\begin{aligned}
\frac{\partial\mathscr{L}}{\partial\sigma} &= -m_\sigma^2\sigma + \Gamma_\sigma\Big[\overline{\Psi}\overleftarrow{D}\Psi + \overline{\Psi}\overrightarrow{D}\Psi\Big] \\
\frac{\partial\mathscr{L}}{\partial(\partial_\alpha\sigma)} &= \frac{1}{2}\Big(\frac{\partial(\partial^\mu\sigma)}{\partial(\partial_\alpha\sigma)}\partial_\mu\sigma + \partial^\mu\sigma\frac{\partial(\partial_\mu\sigma)}{\partial(\partial_\alpha\sigma)}\Big) \\
&= \frac{1}{2}\Big(\partial^\alpha\sigma + \partial^\alpha\sigma\Big) \\
&= \partial^\alpha\sigma
\end{aligned}$$

  The field equation for $\sigma$ meson is

$$\partial_\alpha\partial^\alpha\sigma + m_\sigma^2\sigma = \Gamma_\sigma\Big[\overline{\Psi}\overleftarrow{D}\Psi + \overline{\Psi}\overrightarrow{D}\Psi\Big]. \tag{B.13}$$

- For the $\omega$ meson:

$$\begin{aligned}
\frac{\partial\mathscr{L}}{\partial\omega_\nu} &= \frac{1}{2}m_\omega^2\Big(\frac{\partial\omega^\mu}{\partial\omega_\nu}\omega_\mu + \omega^\mu\frac{\partial\omega_\mu}{\partial\omega_\nu}\Big) - \Gamma_\omega\Big[\overline{\Psi}\overleftarrow{D}\gamma^\mu\Psi\frac{\partial\omega_\mu}{\partial\omega_\nu} + \frac{\partial\omega_\mu}{\partial\omega_\nu}\overline{\Psi}\gamma^\mu\overrightarrow{D}\Psi\Big] \\
&= m_\omega^2\omega^\nu - \Gamma_\omega\Big[\overline{\Psi}\overleftarrow{D}\gamma^\nu\Psi + \overline{\Psi}\gamma^\nu\overrightarrow{D}\Psi\Big]
\end{aligned}$$

$$\begin{aligned}
\frac{\partial\mathscr{L}}{\partial(\partial_\alpha\omega_\nu)} &= -\frac{1}{4}\frac{\partial}{\partial(\partial_\alpha\omega_\nu)}\Big[(\partial^\mu\omega^\tau - \partial^\tau\omega^\mu)(\partial_\mu\omega_\tau - \partial_\tau\omega_\mu)\Big] \\
&= -\frac{1}{4}\Bigg[\Big[\frac{\partial(\partial^\mu\omega^\tau)}{\partial(\partial_\alpha\omega_\nu)} - \frac{\partial(\partial^\tau\omega^\mu)}{\partial(\partial_\alpha\omega_\nu)}\Big](\partial_\mu\omega_\tau - \partial_\tau\omega_\mu) \\
&\qquad + (\partial^\mu\omega^\tau - \partial^\tau\omega^\mu)\Big[\frac{\partial(\partial_\mu\omega_\tau)}{\partial(\partial_\alpha\omega_\nu)} - \frac{\partial(\partial_\tau\omega_\mu)}{\partial(\partial_\alpha\omega_\nu)}\Big]\Bigg] \\
&= -(\partial^\alpha\omega^\nu - \partial^\nu\omega^\alpha) \\
&= -F^{(\omega)\alpha\nu} = F^{(\omega)\nu\alpha}
\end{aligned}$$

  The field equation for $\omega$ meson is

$$\partial_\alpha F^{(\omega)\alpha\nu} + m_\omega^2\omega^\nu = \Gamma_\omega\Big[\overline{\Psi}\overleftarrow{D}\gamma^\nu\Psi + \overline{\Psi}\gamma^\nu\overrightarrow{D}\Psi\Big]. \tag{B.14}$$

## B.4 Densities

The proton and neutron densities (80) in the DD-NLD model are easily calculated through a momentum integration of the relevant integral. For other quantities, however, it is more convenient to introduce an energy integration by substitution because the scalar ($S_i$) and vector ($V_i$) potentials are explicit functions of the energy $E_i$ of nucleon $i$. With the dispersion relation (82) we obtain

$$p = \sqrt{[E_i - V_i(E_i)]^2 - [m_i - S_i(E_i)]^2} \tag{B.15}$$

and the derivative

$$\begin{aligned} \frac{dp}{dE_i} &= \frac{1}{2}\frac{1}{\sqrt{(E_i-V_i)^2-(m_i-S_i)^2}}\left[2(E_i-V_i)(1-\frac{dV_i}{dE_i})+2(m_i-S_i)\left(-\frac{dS_i}{dE_i}\right)\right] \\ &= \frac{1}{\sqrt{(E_i-V_i)^2-(m_i-S_i)^2}}\left[(E_i-V_i)(1-\frac{dV_i}{dE_i})+(m_i-S_i)\left(-\frac{dS_i}{dE_i}\right)\right] \end{aligned} \tag{B.16}$$

with

$$\frac{dV_i}{dE_i} = \left(\Gamma_\omega \omega + \Gamma_\rho \tau_{3,i}\rho\right)\frac{dD}{dE_i}$$

and

$$\frac{dS_i}{dE_i} = \Gamma_\sigma \sigma \frac{dD}{dE_i}\,.$$

Then, the neutron and proton densities are equal to

$$\begin{aligned} n_i &= \frac{\kappa_i}{(2\pi)^3}\int_0^{p_{Fi}} d^3p \\ &= \frac{\kappa_i}{(2\pi)^3}4\pi\int_0^{p_{Fi}} p^2 dp \\ &= \frac{\kappa_i}{8\pi^3}4\pi\int_{E_i^{(\min)}}^{E_i^{(\max)}} \frac{dp}{dE_i}dE_i\sqrt{[E_i-V_i(E_i)]^2-[m_i-S_i(E_i)]^2}^2 \\ &= \frac{\kappa_i}{2\pi^2}\int_{E_i^{(\min)}}^{E_i^{(\max)}} dE_i\sqrt{[E_i-V_i(E_i)]^2-[m_i-S_i(E_i)]^2} \\ &\quad \left[[E_i-V_i(E_i)][1-\frac{dV_i(E_i)}{dE_i}]-[m_i-S_i(E_i)]\frac{dS_i(E_i)}{dE_i}\right]. \end{aligned} \tag{B.17}$$

## B.5 Energy density and pressure

After introducing the energy integration in equations (89) and (90) the expressions for energy density $\epsilon$ and pressure $P$ are the following

$$\begin{aligned}
\varepsilon &= \sum_{i=p,n} \kappa_i \int_0^{p_{Fi}} \frac{d^3p}{(2\pi)^3} E_i - \langle \mathscr{L} \rangle \\
&= \frac{1}{\pi^2} \int_{E_i^{(\min)}}^{E_i^{(\max)}} dE_i \sqrt{[E_i - V_i(E_i)]^2 - [m_i - S(E_i)]^2} \\
&\quad \left[ (E_i - V_i(E_i)) + (m_i - S(E_i)) \frac{dS_i(E_i)}{dE_i} - [E_i - V_i(E_i)] \frac{dV_i(E_i)}{dE_i} \right] - \langle \mathscr{L} \rangle \\
&= \frac{1}{\pi^2} \int_{E_i^{(\min)}}^{E_i^{(\max)}} dE_i \, p(E_i) \Pi_i^0(E_i) E_i - \langle \mathscr{L} \rangle
\end{aligned} \tag{B.18}$$

$$\begin{aligned}
P &= \frac{1}{3} \sum_{i=p,n} \kappa_i \int_0^{p_{Fi}} \frac{d^3p}{(2\pi)^3} \frac{p^2}{\Pi_i^0} + \langle \mathscr{L} \rangle \\
&= \frac{1}{3\pi^2} \sum_{i=p,n} \int_{E_i^{(\min)}}^{E_i^{(\max)}} dE_i \sqrt{[E_i - V_i(E_i)]^2 - [m_i - S(E_i)]^2} \\
&\quad \left[ (E_i - V_i(E_i))^2 - [m_i - S(E_i)]^2 \right] + \langle \mathscr{L} \rangle \\
&= \sum_{i=p,n} \frac{\kappa_i}{6\pi^2} \int_{E_i^{(\min)}}^{E_i^{(\max)}} dE_i \, [p(E_i)]^3 + \langle \mathscr{L} \rangle
\end{aligned} \tag{B.19}$$

with

$$\begin{aligned}
S(E_i) &= \Gamma_\sigma \sigma D(E_i) \\
V(E_i) &= \left( \Gamma_\omega \omega + \Gamma_\rho \tau_{3,i} \rho \right) D(E_i) \, .
\end{aligned}$$

## B.6 Thermodynamic consistency

Using a partial integration and equation (B.16) in the appendix, the thermodynamic identity

$$\begin{aligned}
\varepsilon + p &= \sum_{i=p,n} \frac{\kappa_i}{(2\pi)^3} \frac{p^3}{3} E_i \Big|_0^{p_{Fi}} \\
&\quad + \sum_{i=p,n} \frac{\kappa_i}{(2\pi)^3} \left\{ -\frac{1}{3} \int_0^{p_{Fi}} d^3p \, p \frac{dE_i}{dp} + \frac{1}{3} \sum_{i=p,n} \kappa_i \int_0^{p_{Fi}} d^3p \, \frac{p^2}{\Pi_i^0} \right\} \\
&= \sum_{i=p,n} \mu_i n_i
\end{aligned} \tag{B.20}$$

with the chemical potential $\mu_i = E_i(p_{Fi})$ is easily confirmed.

## B.7 $\beta$ equilibrium

We will derive the $\beta$-equilibrium condition for a system of nucleons and electrons. The function we want to minimize is $\epsilon(n_p, n_n, n_e)$. This is done by the method of Lagrange multipliers. We will construct a new

function $F$ from the one we wish to extremize, while including the two constrains, $n_B = n_p + n_n$ and $n_p = n_e$. The new function is given by

$$F(n_p, n_n, n_e) = \epsilon(n_p, n_n, n_e) + \alpha(n_B - n_p - n_n) + \beta(n_e - n_p) \tag{B.21}$$

with Lagrange multipliers $\alpha$ and $\beta$. For arbitrary variations of three particle densities we require that

$$\frac{\partial F}{\partial n_n} = 0, \quad \frac{\partial F}{\partial n_p} = 0, \quad \frac{\partial F}{\partial n_e} = 0 \tag{B.22}$$

By using

$$\frac{\partial \epsilon}{\partial n_n} = \mu_n \tag{B.23}$$

$$\frac{\partial \epsilon}{\partial n_p} = \mu_p \tag{B.24}$$

$$\frac{\partial \epsilon}{\partial n_e} = \mu_e \tag{B.25}$$

we have

$$\begin{aligned} \frac{\partial F}{\partial n_n} &= \mu_n + \alpha(0-1-0) + \beta(0-0) = 0 \\ \frac{\partial F}{\partial n_p} &= \mu_p + \alpha(0-0-1) + \beta(0-1) = 0 \\ \frac{\partial F}{\partial n_e} &= \mu_e + \alpha(0-0-0) + \beta(1-0) = 0 \end{aligned} \tag{B.26}$$

or

$$\begin{aligned} \mu_n - \alpha &= 0 \\ \mu_p - \alpha - \beta &= 0 \\ \mu_e + \beta &= 0\,. \end{aligned} \tag{B.27}$$

From here the $\beta$ equilibrium relation follows:

$$\mu_n = \mu_p + \mu_e\,. \tag{B.28}$$

# C Parametrization of density dependence

By introducing the ratios

$$r_{21}(x) = \frac{f_m''(x)}{f_m'(x)} \qquad \text{and} \qquad r_{10}(x) = \frac{f_m'(x)}{f_m(x)} \tag{C.1}$$

the density dependence is described only by this two independent parameters, defined by function $f_m(x)$ (98) and its derivatives equal to

$$f_m'(x) = \frac{d}{dx} f_m(x) = \frac{2a_m(b_m - c_m)(x + d_m)}{\left[1 + c_m(x + d_m)^2\right]^2} \tag{C.2}$$

and

$$f_m''(x) = \frac{d^2}{dx^2} f_m(x) = \frac{2a_m(b_m - c_m)\left[1 - 3c_m(x + d_m)^2\right]}{\left[1 + c_m(x + d_m)^2\right]^3} \,. \tag{C.3}$$

Since the couplings $\Gamma_m(n_v)$ (97) are given as functions of $f_m$, their derivatives are the following

$$\begin{aligned} \Gamma_m'(n) &= \frac{d\Gamma_m}{dn}|_n = \Gamma_m(n_{\text{ref}}) \frac{f_m'(x)}{n_{\text{ref}}} \,, \\ \Gamma_m''(n) &= \frac{d^2\Gamma_m}{dn^2}|_n = \Gamma_m(n_{\text{ref}}) \frac{f_m''(x)}{n_{\text{ref}}^2} \,. \end{aligned} \tag{C.4}$$

The conditions $f_\sigma(1) = f_\omega(1) = 1$ and $f_\sigma'(0) = f_\omega'(0) = 0$ lead to

$$a_m = \frac{1 + c_m(1 + d_m)^2}{1 + b_m(1 + d_m)^2} \qquad \text{and} \qquad c_m = \frac{1}{3d_m^2} \,. \tag{C.5}$$

Hence, the rations $r_{21}(x)$ and $r_{10}(x)$ are given as

$$r_{21}(x) = \frac{1 - 3c_m(x + d_m)^2}{\left[1 + c_m(x + d_m)^2\right](x + d_j m)} = \frac{d_m^2 - (x + d_m)^2}{\left[d_m^2 + (x + d_m)^2/3\right](x + d_m)} \tag{C.6}$$

that depends only on $x$ and $d_m$, and

$$r_{10}(x) = \frac{2(b_m - c_m)(x + d_m)}{\left[1 + c_m(x + d_m)^2\right]\left[1 + b_m(x + d_m)^2\right]} \,. \tag{C.7}$$

The model parameters can be extracted from the ratio values. For $x = 1$, the coefficient $d_m$ is determined from $r_{21} < 0$ by the recursion relation

$$d_m = \frac{1}{2}\sqrt{-1 - 2d_m - \frac{3 + 6d_m}{(1 + d_m) r_{21}(1)}} \,. \tag{C.8}$$

Then $c_m = 1/(3d_m^2)$ and $b_m$ follows from $r_{10}$ as

$$b_m = \frac{c_m \frac{2(1+d_m)}{1+c_j(1+d_m)^2} + r_{10}(1)}{\frac{2(1+d_m)}{1+c_m(1+d_m)^2} - (1 + d_m)^2 r_{10}(1)} \,. \tag{C.9}$$

Then $a_m$ is obtained from eq. (C.5).

For $\rho$ meson a simple exponential density dependence is used which depends only on single parameter $a_\rho$, given by

$$a_\rho = -\frac{\Gamma_\rho'(n_{\text{ref}}) n_{\text{ref}}}{\Gamma_\rho(n_{\text{ref}})} \geq 0 \tag{C.10}$$

# List of Figures

# List of Tables

# References


[1] N. K. Glendenning, Compact stars: Nuclear physics, particle physics, and general relativity, 1997.

[2] F. Weber, Strange quark matter and compact stars, Prog. Part. Nucl. Phys. 54 (2005) 193–288. arXiv:astro-ph/0407155, doi:10.1016/j.ppnp.2004.07.001.

[3] P. Haensel, A. Y. Potekhin, D. G. Yakovlev, Neutron stars 1: Equation of state and structure, Vol. 326, Springer, New York, USA, 2007. doi:10.1007/978-0-387-47301-7.

[4] J. M. Lattimer, The nuclear equation of state and neutron star masses, Ann. Rev. Nucl. Part. Sci. 62 (2012) 485–515. arXiv:1305.3510, doi:10.1146/annurev-nucl-102711-095018.

[5] A. Mezzacappa, ASCERTAINING THE CORE COLLAPSE SUPERNOVA MECHANISM: The State of the Art and the Road Ahead, Ann. Rev. Nucl. Part. Sci. 55 (2005) 467–515. doi:10.1146/annurev.nucl.55.090704.151608.

[6] H.-T. Janka, K. Langanke, A. Marek, G. Martinez-Pinedo, B. Mueller, Theory of Core-Collapse Supernovae, Phys. Rept. 442 (2007) 38–74. arXiv:astro-ph/0612072, doi:10.1016/j.physrep.2007.02.002.

[7] K. Kotake, K. Sato, K. Takahashi, Explosion mechanism, neutrino burst, and gravitational wave in core-collapse supernovae, Rept. Prog. Phys. 69 (2006) 971–1144. arXiv:astro-ph/0509456, doi:10.1088/0034-4885/69/4/R03.

[8] C. D. Ott, The Gravitational Wave Signature of Core-Collapse Supernovae, Class. Quant. Grav. 26 (2009) 063001. arXiv:0809.0695, doi:10.1088/0264-9381/26/6/063001.

[9] H.-T. Janka, Explosion Mechanisms of Core-Collapse Supernovae, Ann. Rev. Nucl. Part. Sci. 62 (2012) 407–451. arXiv:1206.2503, doi:10.1146/annurev-nucl-102711-094901.

[10] A. Burrows, Colloquium: Perspectives on core-collapse supernova theory, Rev. Mod. Phys. 85 (2013) 245. arXiv:1210.4921, doi:10.1103/RevModPhys.85.245.

[11] M. Prakash, I. Bombaci, M. Prakash, P. J. Ellis, J. M. Lattimer, R. Knorren, Composition and structure of protoneutron stars, Phys. Rept. 280 (1997) 1–77. arXiv:nucl-th/9603042, doi:10.1016/S0370-1573(96)00023-3.

[12] J. A. Pons, S. Reddy, M. Prakash, J. M. Lattimer, J. A. Miralles, Evolution of protoneutron stars, Astrophys. J. 513 (1999) 780. arXiv:astro-ph/9807040, doi:10.1086/306889.

[13] M. Shibata, K. Taniguchi, Coalescence of Black Hole-Neutron Star Binaries, Living Rev. Rel. 14 (2011) 6. doi:10.12942/lrr-2011-6.

[14] J. A. Faber, F. A. Rasio, Binary Neutron Star Mergers, Living Rev. Rel. 15 (2012) 8. arXiv:1204.3858, doi:10.12942/lrr-2012-8.

[15] S. Rosswog, The multi-messenger picture of compact binary mergers, Int. J. Mod. Phys. D24 (05) (2015) 1530012. arXiv:1501.02081, doi:10.1142/S0218271815300128.

[16] B. Blattel, V. Koch, U. Mosel, Transport-theoretical analysis of relativistic heavy-ion collisions, Reports on Progress in Physics 56 (1) (1993) 1.

[17] C. Fuchs, P. Essler, T. Gaitanos, H. H. Wolter, Temperature and thermodynamic instabilities in heavy ion collisions, Nucl. Phys. A626 (1997) 987–998. arXiv:nucl-th/9705023, doi:10.1016/S0375-9474(97)00467-3.

[18] Gsi helmholtzzentrum für schwerionenforschung, https://www.gsi.de/en/researchaccelerators/fair/research_with_fair/nuclear_matter_physics.htm.

[19] C. DeTar, U. M. Heller, QCD Thermodynamics from the Lattice, Eur. Phys. J. A41 (2009) 405–437. arXiv:0905.2949, doi:10.1140/epja/i2009-10825-3.

[20] A. Bazavov, et al., The chiral and deconfinement aspects of the QCD transition, Phys. Rev. D85 (2012) 054503. arXiv:1111.1710, doi:10.1103/PhysRevD.85.054503.

[21] The european organization for nuclear research (cern), https://home.cern/.

[22] U. W. Heinz, M. Jacob, Evidence for a new state of matter: An Assessment of the results from the CERN lead beam programarXiv:nucl-th/0002042.

[23] Cern: A new state of matter, http://newstate-matter.web.cern.ch/newstate-matter/science.html.

[24] Brookhaven national laboratory's relativistic heavy ion collider, https://www.bnl.gov/rhic/.

[25] I. Arsene, et al., Quark gluon plasma and color glass condensate at RHIC? The Perspective from the BRAHMS experiment, Nucl. Phys. A757 (2005) 1–27. arXiv:nucl-ex/0410020, doi:10.1016/j.nuclphysa.2005.02.130.

[26] B. B. Back, et al., The PHOBOS perspective on discoveries at RHIC, Nucl. Phys. A757 (2005) 28–101. arXiv:nucl-ex/0410022, doi:10.1016/j.nuclphysa.2005.03.084.

[27] K. Adcox, et al., Formation of dense partonic matter in relativistic nucleus-nucleus collisions at RHIC: Experimental evaluation by the PHENIX collaboration, Nucl. Phys. A757 (2005) 184–283. arXiv:nucl-ex/0410003, doi:10.1016/j.nuclphysa.2005.03.086.

[28] K. Rajagopal, F. Wilczek, The Condensed Matter Physics of QCD, At the Frontier of Particle Physics, Vol. Handbook of QCD, World Scientific, 2001.

[29] M. G. Alford, Color superconducting quark matter, Ann. Rev. Nucl. Part. Sci. 51 (2001) 131–160. arXiv:hep-ph/0102047, doi:10.1146/annurev.nucl.51.101701.132449.

[30] M. G. Alford, K. Rajagopal, F. Wilczek, QCD at finite baryon density: Nucleon droplets and color superconductivity, Phys. Lett. B422 (1998) 247–256. arXiv:hep-ph/9711395, doi:10.1016/S0370-2693(98)00051-3.

[31] R. Rapp, T. Schäfer, E. V. Shuryak, M. Velkovsky, High density QCD and instantons, Annals Phys. 280 (2000) 35–99. arXiv:hep-ph/9904353, doi:10.1006/aphy.1999.5991.

[32] N. K. Glendenning, P. Hecking, ON 'PION CONDENSATION IN A RELATIVISTIC FIELD THEORY AND PI RHO INTERACTION.', Phys. Lett. B116 (1982) 1–3. doi:10.1016/0370-2693(82)90021-1.

[33] D. Chatterjee, I. Vidaña, Do hyperons exist in the interior of neutron stars?, Eur. Phys. J. A52 (2) (2016) 29. arXiv:1510.06306, doi:10.1140/epja/i2016-16029-x.

[34] D. G. Yakovlev, C. J. Pethick, Neutron star coolingdoi:10.1146/annurev.astro.42.053102.134013.

[35] T. Strohmayer, S. Mahmoodifar, Discovery of a neutron star oscillation mode during a superburst, The Astrophysical Journal Letters 793 (2) (2014) L38.
URL http://stacks.iop.org/2041-8205/793/i=2/a=L38

[36] B. Haskell, R-modes in neutron stars: Theory and observations, International Journal of Modern Physics E 24 (09) (2015) 1541007. doi:10.1142/S0218301315410074.

[37] R. Turolla, S. Zane, A. Watts, Magnetars: the physics behind observations. A review, Rept. Prog. Phys. 78 (11) (2015) 116901. arXiv:1507.02924, doi:10.1088/0034-4885/78/11/116901.

[38] F. Weber, Strange quark matter and compact stars, Progress in Particle and Nuclear Physics 54 (1) (2005) 193 – 288. doi:https://doi.org/10.1016/j.ppnp.2004.07.001.
URL http://www.sciencedirect.com/science/article/pii/S0146641004001061

[39] T. Klahn, et al., Constraints on the high-density nuclear equation of state from the phenomenology of compact stars and heavy-ion collisions, Phys. Rev. C74 (2006) 035802. arXiv:nucl-th/0602038, doi:10.1103/PhysRevC.74.035802.

[40] J. M. Lattimer, M. Prakash, Neutron Star Observations: Prognosis for Equation of State Constraints, Phys. Rept. 442 (2007) 109–165. arXiv:astro-ph/0612440, doi:10.1016/j.physrep.2007.02.003.

[41] J. M. Lattimer, Y. Lim, Constraining the Symmetry Parameters of the Nuclear Interaction, Astrophys. J. 771 (2013) 51. arXiv:1203.4286, doi:10.1088/0004-637X/771/1/51.

[42] M. Oertel, M. Hempel, T. Klähn, S. Typel, Equations of state for supernovae and compact stars, Rev. Mod. Phys. 89 (1) (2017) 015007. arXiv:1610.03361, doi:10.1103/RevModPhys.89.015007.

[43] H. Yukawa, On the Interaction of Elementary Particles I, Proc. Phys. Math. Soc. Jap. 17 (1935) 48–57, [Prog. Theor. Phys. Suppl.1,1(1935)]. doi:10.1143/PTPS.1.1.

[44] Unedf scidac collaboration, http://unedf.mps.ohio-state.edu/.

[45] M. R. Anastasio, L. S. Celenza, W. S. Pong, C. M. Shakin, RELATIVISTIC NUCLEAR STRUCTURE PHYSICS, Phys. Rept. 100 (1983) 327–401. doi:10.1016/0370-1573(83)90060-1.

[46] B. Ter Haar, R. Malfliet, Nucleons, Mesons and Deltas in Nuclear Matter. A Relativistic Dirac-Bruckner Approach, Phys. Rept. 149 (1987) 207–286. doi:10.1016/0370-1573(87)90085-8.

[47] R. Brockmann, R. Machleidt, Relativistic nuclear structure. 1: Nuclear matter, Phys. Rev. C42 (1990) 1965–1980. doi:10.1103/PhysRevC.42.1965.

[48] P. Hohenberg, W. Kohn, Inhomogeneous Electron Gas, Phys. Rev. 136 (1964) B864–B871. doi:10.1103/PhysRev.136.B864.

[49] W. Kohn, L. J. Sham, Self-Consistent Equations Including Exchange and Correlation Effects, Phys. Rev. 140 (1965) A1133–A1138. doi:10.1103/PhysRev.140.A1133.

[50] T. H. R. Skyrme, CVII. The nuclear surface, Phil. Mag. 1 (1956) 1043–1054. doi:10.1080/14786435608238186.

[51] T. Skyrme, The effective nuclear potential, Nucl. Phys. 9 (1959) 615–634. doi:10.1016/0029-5582(58)90345-6.

[52] J. Decharge, D. Gogny, Hartree-Fock-Bogolyubov calculations with the D1 effective interactions on spherical nuclei, Phys. Rev. C21 (1980) 1568–1593. doi:10.1103/PhysRevC.21.1568.

[53] J. D. Walecka, A Theory of highly condensed matter, Annals Phys. 83 (1974) 491–529. doi:10.1016/0003-4916(74)90208-5.

[54] S. A. Chin, J. D. Walecka, An Equation of State for Nuclear and Higher-Density Matter Based on a Relativistic Mean-Field Theory, Phys. Lett. B52 (1974) 24–28. doi:10.1016/0370-2693(74)90708-4.

[55] B. D. Serot, J. D. Walecka, The Relativistic Nuclear Many Body Problem, Adv. Nucl. Phys. 16 (1986) 1–327.

[56] B. D. Serot, Quantum hadrodynamics, Rept. Prog. Phys. 55 (1992) 1855–1946. doi:10.1088/0034-4885/55/11/001.

[57] M. Dutra, O. Lourenco, J. Sa Martins, A. Delfino, J. Stone, et al., Skyrme Interaction and Nuclear Matter Constraints, Phys.Rev. C85 (2012) 035201. arXiv:1202.3902, doi:10.1103/PhysRevC.85.035201.

[58] M. Dutra, O. Lourenço, S. Avancini, B. Carlson, A. Delfino, et al., Relativistic Mean-Field Hadronic Models under Nuclear Matter Constraints, Phys.Rev. C90 (5) (2014) 055203. arXiv:1405.3633, doi:10.1103/PhysRevC.90.055203.

[59] J. Piekarewicz, Unmasking the nuclear matter equation of state, Phys. Rev. C69 (2004) 041301. arXiv:nucl-th/0312020, doi:10.1103/PhysRevC.69.041301.

[60] Shlomo, S., Kolomietz, V. M., Colò, G., Deducing the nuclear-matter incompressibility coefficient from data on isoscalar compression modes, Eur. Phys. J. A 30 (1) (2006) 23–30. doi:10.1140/epja/i2006-10100-3.
URL https://doi.org/10.1140/epja/i2006-10100-3

[61] P. Klupfel, P. G. Reinhard, T. J. Burvenich, J. A. Maruhn, Variations on a theme by skyrme: A systematic study of adjustments of model parameters, Phys. Rev. C79 (2009) 034310. arXiv:0804.3385, doi:10.1103/PhysRevC.79.034310.

[62] M. Kortelainen, T. Lesinski, J. More, W. Nazarewicz, J. Sarich, N. Schunck, M. V. Stoitsov, S. Wild, Nuclear Energy Density Optimization, Phys. Rev. C82 (2010) 024313. arXiv:1005.5145, doi:10.1103/PhysRevC.82.024313.

[63] J. M. Lattimer, A. W. Steiner, Constraints on the symmetry energy using the mass-radius relation of neutron stars, Eur. Phys. J. A50 (2014) 40. doi:10.1140/epja/i2014-14040-y.

[64] W. Baade, F. Zwicky, Remarks on Super-Novae and Cosmic Rays, Phys. Rev. 46 (1934) 7677.

[65] J. Chadwick, Possible Existence of a Neutron, Nature 129 (1932) 312. doi:10.1038/129312a0.

[66] J. Bell, A. Hewish, J. D. H. Pilkington, P. F. Scott, R. A. Collins, Observation of a Rapidly Pulsating Radio Source., Nature 217 (1968) 709.

[67] R. N. Manchester, G. B. Hobbs, A. Teoh, M. Hobbs, The Australia Telescope National Facility pulsar catalogue, Astron. J. 129 (2005) 1993. arXiv:astro-ph/0412641, doi:10.1086/428488.

[68] R. A. Hulse, J. H. Taylor, Discovery of a pulsar in a binary system, Astrophys. J. 195 (1975) L51–L53. doi:10.1086/181708.

[69] D. Backer, S. Kulkarni, C. Heiles, M. Davis, W. Goss, A millisecond pulsar, Nature. 300 (1982) 615–618. doi:10.1038/300615a0.

[70] A. G. Lyne, et al., A Double - pulsar system - A Rare laboratory for relativistic gravity and plasma physics, Science 303 (2004) 1153–1157. arXiv:astro-ph/0401086, doi:10.1126/science.1094645.

[71] P. Demorest, T. Pennucci, S. Ransom, M. Roberts, J. Hessels, Shapiro Delay Measurement of A Two Solar Mass Neutron Star, Nature 467 (2010) 1081–1083. arXiv:1010.5788, doi:10.1038/nature09466.

[72] J. Antoniadis, P. C. Freire, N. Wex, T. M. Tauris, R. S. Lynch, et al., A Massive Pulsar in a Compact Relativistic Binary, Science 340 (2013) 6131. arXiv:1304.6875, doi:10.1126/science.1233232.

[73] D. Lonardoni, A. Lovato, S. Gandolfi, F. Pederiva, The hyperon puzzle: new hints from Quantum Monte Carlo calculationsarXiv:1407.4448.

[74] Fortin, M., Zdunik, J. L., Haensel, P., Bejger, M., Neutron stars with hyperon cores: stellar radii and equation of state near nuclear density, A&A 576 (2015) A68. doi:10.1051/0004-6361/201424800.
URL https://doi.org/10.1051/0004-6361/201424800

[75] A. Drago, A. Lavagno, G. Pagliara, D. Pigato, Early appearance of $\Delta$ isobars in neutron stars, Phys. Rev. C 90 (2014) 065809. doi:10.1103/PhysRevC.90.065809.
URL https://link.aps.org/doi/10.1103/PhysRevC.90.065809

[76] B.-J. Cai, F. J. Fattoyev, B.-A. Li, W. G. Newton, Critical density and impact of $\Delta(1232)$ resonance formation in neutron stars, Phys. Rev. C 92 (2015) 015802. doi:10.1103/PhysRevC.92.015802.
URL https://link.aps.org/doi/10.1103/PhysRevC.92.015802

[77] A. Tiengo, et al., A variable absorption feature in the X-ray spectrum of a magnetar, Nature 500 (2013) 312. arXiv:1308.4987, doi:10.1038/nature12386.

[78] J. W. T. Hessels, S. M. Ransom, I. H. Stairs, P. C. C. Freire, V. M. Kaspi, F. Camilo, A Radio Pulsar Spinning at 716 Hz, Science 311 (2006) 1901–1904. arXiv:astro-ph/0601337, doi:10.1126/science.1123430.

[79] N. Chamel, P. Haensel, Physics of Neutron Star Crusts, Living Rev. Rel. 11 (2008) 10. arXiv:0812.3955, doi:10.12942/lrr-2008-10.

[80] D. G. Ravenhall, C. J. Pethick, J. R. Wilson, STRUCTURE OF MATTER BELOW NUCLEAR SATURATION DENSITY, Phys. Rev. Lett. 50 (1983) 2066–2069. doi:10.1103/PhysRevLett.50.2066.

[81] G. Baym, C. Pethick, P. Sutherland, The Ground state of matter at high densities: Equation of state and stellar models, Astrophys. J. 170 (1971) 299–317. doi:10.1086/151216.

[82] P. Haensel, B. Pichon, Experimental nuclear masses and the ground state of cold dense matter, Astron. Astrophys. 283 (1994) 313. arXiv:nucl-th/9310003.

[83] S. B. Ruester, M. Hempel, J. Schaffner-Bielich, The outer crust of non-accreting cold neutron stars, Phys. Rev. C73 (2006) 035804. arXiv:astro-ph/0509325, doi:10.1103/PhysRevC.73.035804.

[84] G. Baym, H. A. Bethe, C. Pethick, Neutron star matter, Nucl. Phys. A175 (1971) 225–271. doi:10.1016/0375-9474(71)90281-8.

[85] J. W. Negele, D. Vautherin, Neutron star matter at subnuclear densities, Nucl. Phys. A207 (1973) 298–320. doi:10.1016/0375-9474(73)90349-7.

[86] F. Douchin, P. Haensel, A unified equation of state of dense matter and neutron star structure, Astron. Astrophys. 380 (2001) 151. arXiv:astro-ph/0111092, doi:10.1051/0004-6361:20011402.

[87] C. Ducoin, J. Margueron, C. Providencia, I. Vidana, Core-crust transition in neutron stars: predictivity of density developments, Phys. Rev. C83 (2011) 045810. arXiv:1102.1283, doi:10.1103/PhysRevC.83.045810.

[88] F. Grill, H. Pais, C. Providência, I. Vidaña, S. S. Avancini, Equation of state and thickness of the inner crust of neutron stars, Phys. Rev. C90 (4) (2014) 045803. arXiv:1404.2753, doi:10.1103/PhysRevC.90.045803.

[89] G. N. K, Compact Stars-Nuclear Physics, Particle Physics, and General Relativity, 2nd Edition, New York:Springer, 2000.

[90] J. Oppenheimer, G. Volkoff, On Massive neutron cores, Phys.Rev. 55 (1939) 374–381. doi:10.1103/PhysRev.55.374.

[91] R. C. Tolman, Static solutions of Einstein's field equations for spheres of fluid, Phys.Rev. 55 (1939) 364–373. doi:10.1103/PhysRev.55.364.

[92] M. H. van Kerkwijk, R. Breton, S. R. Kulkarni, Evidence for a Massive Neutron Star from a Radial-Velocity Study of the Companion to the Black Widow Pulsar PSR B1957+20, Astrophys. J. 728 (2011) 95. arXiv:1009.5427, doi:10.1088/0004-637X/728/2/95.

[93] D. L. Kaplan, V. B. Bhalerao, M. H. van Kerkwijk, D. Koester, S. R. Kulkarni, K. Stovall, A Metal-Rich Low-Gravity Companion to a Massive Millisecond Pulsar, Astrophys. J. 765 (2013) 158. arXiv:1302.2492, doi:10.1088/0004-637X/765/2/158.

[94] J. M. Lattimer, M. Prakash, The Ultimate energy density of observable cold matter, Phys. Rev. Lett. 94 (2005) 111101. arXiv:astro-ph/0411280, doi:10.1103/PhysRevLett.94.111101.

[95] M. Fortin, J. Zdunik, P. Haensel, M. Bejger, Neutron stars with hyperon cores: stellar radii and eos near nuclear densityarXiv:1408.3052.

[96] A. Drago, A. Lavagno, G. Pagliara, D. Pigato, Early appearance of $\Delta$ isobars in neutron stars, Phys.Rev. C90 (6) (2014) 065809. arXiv:1407.2843, doi:10.1103/PhysRevC.90.065809.

[97] B.-J. Cai, F. J. Fattoyev, B.-A. Li, W. G. Newton, Critical density and impact of $\delta(1232)$ resonance formation in neutron starsarXiv:1501.01680.

[98] J. W. T. Hessels, S. M. Ransom, I. H. Stairs, P. C. C. Freire, V. M. Kaspi, F. Camilo, A radio pulsar spinning at 716-hz, Science 311 (2006) 1901–1904. arXiv:astro-ph/0601337, doi:10.1126/science.1123430.

[99] J. S. Read, B. D. Lackey, B. J. Owen, J. L. Friedman, Constraints on a phenomenologically parameterized neutron-star equation of state, Phys. Rev. D79 (2009) 124032. arXiv:0812.2163, doi:10.1103/PhysRevD.79.124032.

[100] F. Ozel, D. Psaltis, Reconstructing the Neutron-Star Equation of State from Astrophysical Measurements, Phys. Rev. D80 (2009) 103003. arXiv:0905.1959, doi:10.1103/PhysRevD.80.103003.

[101] F. Ozel, G. Baym, T. Guver, Astrophysical Measurement of the Equation of State of Neutron Star Matter, Phys. Rev. D82 (2010) 101301. arXiv:1002.3153, doi:10.1103/PhysRevD.82.101301.

[102] A. W. Steiner, J. M. Lattimer, E. F. Brown, The Neutron Star Mass-Radius Relation and the Equation of State of Dense Matter, Astrophys. J. 765 (2013) L5. arXiv:1205.6871, doi:10.1088/2041-8205/765/1/L5.

[103] The neutron star interior composition explorer mission, nicer, https://heasarc.gsfc.nasa.gov/docs/nicer/.

[104] The athena x-ray observatory, athena, http://www.the-athena-x-ray-observatory.eu/.

[105] Large observatory for x-ray timing homepage, loft, http://www.isdc.unige.ch/loft/.

[106] Laser interferometer gravitational-wave observatory, ligo, https://www.ligo.caltech.edu/.

[107] S. Hama, B. Clark, E. Cooper, H. Sherif, R. Mercer, Global Dirac optical potentials for elastic proton scattering from heavy nuclei, Phys.Rev. C41 (1990) 2737–2755. doi:10.1103/PhysRevC.41.2737.

[108] E. Cooper, S. Hama, B. Clark, R. Mercer, Global Dirac phenomenology for proton nucleus elastic scattering, Phys.Rev. C47 (1993) 297–311. doi:10.1103/PhysRevC.47.297.

[109] T. Gaitanos, M. M. Kaskulov, Momentum dependent mean-field dynamics of compressed nuclear matter and neutron stars, Nucl.Phys. A899 (2013) 133–169. arXiv:1206.4821, doi:10.1016/j.nuclphysa.2013.01.002.

[110] S. Typel, Relativistic model for nuclear matter and atomic nuclei with momentum-dependent self-energies, Phys.Rev. C71 (2005) 064301. arXiv:nucl-th/0501056, doi:10.1103/PhysRevC.71.064301.

[111] P. Danielewicz, R. Lacey, W. G. Lynch, Determination of the equation of state of dense matter, Science 298 (2002) 1592–1596. doi:10.1126/science.1078070.

[112] H.-P. Duerr, Relativistic effects in nuclear forces, Phys. Rev. 103 (1956) 469–480. doi:10.1103/PhysRev.103.469.

[113] F. Wilczek, Particle physics: Hard-core revelations, Nature 445 (2007) 156–157. doi:10.1038/445156a.

[114] J. Boguta, A. R. Bodmer, Relativistic Calculation of Nuclear Matter and the Nuclear Surface, Nucl. Phys. A292 (1977) 413–428. doi:10.1016/0375-9474(77)90626-1.

[115] C. Fuchs, H. Lenske, H. H. Wolter, Density dependent hadron field theory, Phys. Rev. C52 (1995) 3043–3060. arXiv:nucl-th/9507044, doi:10.1103/PhysRevC.52.3043.

[116] C. Fuchs, Mean field theory, http://www.tphys.physik.uni-tuebingen.de/faessler/Fuchs/Skript/Chap_8.pdf.

[117] S. Typel, H. Wolter, Relativistic mean field calculations with density dependent meson nucleon coupling, Nucl.Phys. A656 (1999) 331–364. doi:10.1016/S0375-9474(99)00310-3.

[118] C. Fuchs, The relativistic dirac-brueckner approach to nuclear matter, Lect.Notes Phys. 641 (2004) 119–146. arXiv:nucl-th/0309003.

[119] J.-M. Zhang, S. Das Gupta, C. Gale, Momentum dependent nuclear mean fields and collective flow in heavy ion collisions, Phys.Rev. C50 (1994) 1617–1625. arXiv:nucl-th/9405006, doi:10.1103/PhysRevC.50.1617.

[120] S. Typel, T. von Chossy, H. Wolter, Relativistic mean field model with generalized derivative nucleon meson couplings, Phys.Rev. C67 (2003) 034002. arXiv:nucl-th/0210090, doi:10.1103/PhysRevC.67.034002.

[121] T. Gaitanos, M. Kaskulov, U. Mosel, Non-Linear derivative interactions in relativistic hadrodynamics, Nucl.Phys. A828 (2009) 9–28. arXiv:0904.1130, doi:10.1016/j.nuclphysa.2009.06.019.

[122] T. Gaitanos, M. Kaskulov, Energy Dependent Isospin Asymmetry in Mean-Field Dynamics, Nucl.Phys. A878 (2012) 49–66. arXiv:1109.4837, doi:10.1016/j.nuclphysa.2012.01.013.

[123] J. Zimanyi, S. Moszkowski, Nuclear Equation of state with derivative scalar coupling, Phys.Rev. C42 (1990) 1416–1421. doi:10.1103/PhysRevC.42.1416.

[124] Y. Chen, Relativistic mean field model for nuclear matter with non-linear derivative couplings, Eur.Phys.J. A48 (2012) 132. doi:10.1140/epja/i2012-12132-4.

[125] Y. Chen, Relativistic mean-field model with nonlinear derivative couplings for nuclear matter and nuclei, Phys.Rev. C89 (6) (2014) 064306. doi:10.1103/PhysRevC.89.064306.

[126] S. Typel, Rmf+ code, version 3.01, Private communication.

[127] S. Typel, Mr relation of nss with given eos using 4th order runge-kutta, version 1.04, Private communication.

[128] S. Typel, G. Ropke, T. Klahn, D. Blaschke, H. H. Wolter, Composition and thermodynamics of nuclear matter with light clusters, Phys. Rev. C81 (2010) 015803. arXiv:0908.2344, doi:10.1103/PhysRevC.81.015803.

[129] P. G. Reinhard, M. Rufa, J. Maruhn, W. Greiner, J. Friedrich, Nuclear Ground State Properties in a Relativistic Meson Field Theory, Z. Phys. A323 (1986) 13–25.

[130] M. Rufa, P. G. Reinhard, J. A. Maruhn, W. Greiner, M. R. Strayer, Optimal parametrization for the relativistic mean-field model of the nucleus, Phys. Rev. C38 (1988) 390–409. doi:10.1103/PhysRevC.38.390.

[131] D. Baye, P. H. Heenen, Generalised meshes for quantum mechanical problems, Journal of Physics A: Mathematical and General 19 (11) (1986) 2041.
URL http://stacks.iop.org/0305-4470/19/i=11/a=013

[132] M. Vincke, L. Malegat, D. Baye, Regularization of singularities in lagrange-mesh calculations, Journal of Physics B: Atomic, Molecular and Optical Physics 26 (5) (1993) 811.
URL http://stacks.iop.org/0953-4075/26/i=5/a=006

[133] D. Baye, Lagrange-mesh method for quantum-mechanical problems, physica status solidi (b) 243 (5) (2006) 1095–1109. doi:10.1002/pssb.200541305.
URL http://dx.doi.org/10.1002/pssb.200541305

[134] G. Audi, A. H. Wapstra, The 1993 atomic mass evaluation. 1. atomic mass table, Nucl. Phys. A565 (1993) 1–65. doi:10.1016/0375-9474(93)90024-R.

[135] Nudat database, national nuclear data center, http://www.nndc.bnl.gov/nndc/nudat/.

[136] S. Gandolfi, A. Gezerlis, J. Carlson, Neutron Matter from Low to High Density, Ann. Rev. Nucl. Part. Sci. 65 (2015) 303–328. arXiv:1501.05675, doi:10.1146/annurev-nucl-102014-021957.

[137] M. Barranco, J. R. Buchler, Thermodynamic properties of hot nucleonic matter, Phys. Rev. C22 (1980) 1729–1737. doi:10.1103/PhysRevC.22.1729.

[138] H. Muller, B. D. Serot, Phase transitions in warm, asymmetric nuclear matter, Phys. Rev. C52 (1995) 2072–2091. arXiv:nucl-th/9505013, doi:10.1103/PhysRevC.52.2072.

[139] N. Itoh, Hydrostatic Equilibrium of Hypothetical Quark Stars, Prog. Theor. Phys. 44 (1970) 291. doi:10.1143/PTP.44.291.

[140] H. Heiselberg, C. J. Pethick, E. F. Staubo, Quark matter droplets in neutron stars, Phys. Rev. Lett. 70 (1993) 1355–1359. doi:10.1103/PhysRevLett.70.1355.

[141] A. Steiner, M. Prakash, J. Lattimer, P. Ellis, Isospin asymmetry in nuclei and neutron stars, Physics Reports 411 (6) (2005) 325 – 375. doi:http://doi.org/10.1016/j.physrep.2005.02.004. URL http://www.sciencedirect.com/science/article/pii/S0370157305001043

[142] M. P. J. M. Lattimer*, The Physics of Neutron Stars, Science 304 (2004) 536–542. doi:10.1126/science.1090720.

[143] H. Shen, H. Toki, K. Oyamatsu, K. Sumiyoshi, Relativistic equation of state of nuclear matter for supernova explosion, Prog. Theor. Phys. 100 (1998) 1013. arXiv:nucl-th/9806095, doi:10.1143/PTP.100.1013.

[144] P. Chomaz, F. Gulminelli, C. Ducoin, P. Napolitani, K. H. O. Hasnaoui, Anomalous thermodynamics and phase transitions of neutron-star matter, Phys. Rev. C75 (2007) 065805. arXiv:astro-ph/0507633, doi:10.1103/PhysRevC.75.065805.

[145] G. Watanabe, Simulating pasta phases by molecular dynamics and cold atoms: Formation in supernovae and superfluid neutrons in neutron stars, Prog. Theor. Phys. Suppl. 186 (2010) 45–50. arXiv:1007.0153, doi:10.1143/PTPS.186.45.

[146] J. Schaffner-Bielich, M. Hanauske, H. Stoecker, W. Greiner, Phase transition to hyperon matter in neutron stars, Phys. Rev. Lett. 89 (2002) 171101. arXiv:astro-ph/0005490, doi:10.1103/PhysRevLett.89.171101.

[147] F. Gulminelli, A. R. Raduta, M. Oertel, Phase transition towards strange matter, Phys. Rev. C86 (2012) 025805. arXiv:1206.4924, doi:10.1103/PhysRevC.86.025805.

[148] F. Gulminelli, A. R. Raduta, M. Oertel, J. Margueron, Strangeness-driven phase transition in (proto-)neutron star matter, Phys. Rev. C87 (5) (2013) 055809. arXiv:1301.0390, doi:10.1103/PhysRevC.87.055809.

[149] G. A. Lalazissis, J. Konig, P. Ring, A New parametrization for the Lagrangian density of relativistic mean field theory, Phys. Rev. C55 (1997) 540–543. arXiv:nucl-th/9607039, doi:10.1103/PhysRevC.55.540.

[150] T. Nayak, Phases of nuclear matter, Current science 103 (8) (2012) 888–894.

[151] J. W. Holt, N. Kaiser, W. Weise, Nuclear chiral dynamics and thermodynamics, Prog. Part. Nucl. Phys. 73 (2013) 35–83. arXiv:1304.6350, doi:10.1016/j.ppnp.2013.08.001.

[152] P. J. SIEMENS, Liquid-gas phase transition in nuclear matter, Nature 305 (1983) 410–412. doi:10.1038/305410a0.

[153] O. Lourenço, B. M. Santos, M. Dutra, A. Delfino, Correlations between critical parameters and bulk properties of nuclear matter, Phys. Rev. C94 (4) (2016) 045207. arXiv:1610.01974, doi:10.1103/PhysRevC.94.045207.

[154] J. B. Natowitz, K. Hagel, Y. Ma, M. Murray, L. Qin, R. Wada, J. Wang, Limiting temperatures and the equation of state of nuclear matter, Phys. Rev. Lett. 89 (2002) 212701. arXiv:nucl-ex/0204015, doi:10.1103/PhysRevLett.89.212701.

[155] V. A. Karnaukhov, et al., Critical temperature for the nuclear liquid gas phase transition, Phys. Rev. C67 (2003) 011601. arXiv:nucl-ex/0302006, doi:10.1103/PhysRevC.67.011601.

[156] J. B. Elliott, P. T. Lake, L. G. Moretto, L. Phair, Determination of the coexistence curve, critical temperature, density, and pressure of bulk nuclear matter from fragment emission data, Phys. Rev. C 87 (2013) 054622. doi:10.1103/PhysRevC.87.054622.
URL https://link.aps.org/doi/10.1103/PhysRevC.87.054622

[157] C. Ducoin, P. Chomaz, F. Gulminelli, Role of isospin in the nuclear liquid-gas phase transition, Nucl. Phys. A771 (2006) 68–92. arXiv:nucl-th/0512029, doi:10.1016/j.nuclphysa.2006.03.005.

[158] A. Rios, Effective interaction dependence of the liquid-gas phase transition in symmetric nuclear matter, Nucl. Phys. A845 (2010) 58–87. arXiv:1002.1907, doi:10.1016/j.nuclphysa.2010.05.057.

[159] V. Baran, M. Colonna, M. Di Toro, A. B. Larionov, Spinodal decomposition of low-density asymmetric nuclear matter, Nucl. Phys. A632 (1998) 287–303. arXiv:0705.1291, doi:10.1016/S0375-9474(98)00006-2.

[160] S. S. Avancini, L. Brito, P. Chomaz, D. P. Menezes, C. Providência, Spinodal instabilities and the distillation effect in relativistic hadronic models, Phys. Rev. C 74 (2006) 024317. doi:10.1103/PhysRevC.74.024317.
URL https://link.aps.org/doi/10.1103/PhysRevC.74.024317

[161] L. D. Landau, E. M. Lifshitz, Statistical physics, Vol. 1, Pergamon Press, New York, 1989.

# Curriculum vitae

Sofija Antić
born on 9th of May 1988
in Pula, Croatia

| | |
|---|---|
| 10/2006 - 02/2013 | Master Studies at the University of Zagreb,<br>Zagreb, Croatia |
| 15/02/2013 | Master of science (M.sc.),<br>Topic: Quantum phase transitions in atomic nuclei |
| 10/2013 - 07/2017 | Doctoral studies at Technical University of Darmstadt,<br>Darmstadt, Germany |
| 12/07/2017 | Doctor rerum naturalium (Dr. rer. nat.),<br>Topic: Generalized relativistic mean-field model with non-linear derivative nucleon-meson couplings for nuclear matter and finite nuclei |